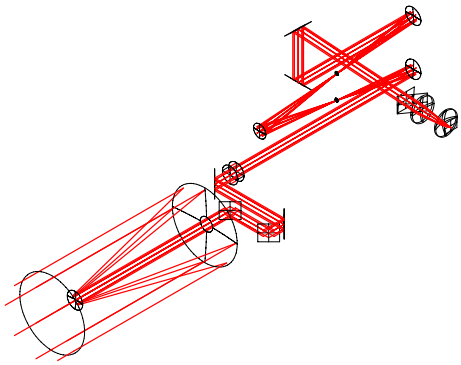

The *Mid*-Infrared *I*nterferometric
Instrument for the
Very Large Telescope
Interferometer

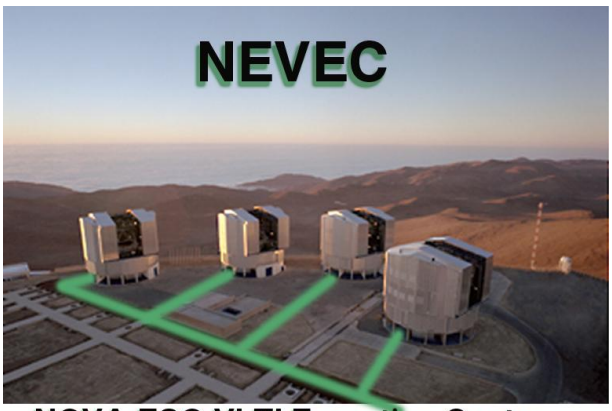

MIDI

Correlation of MIDI Phase Fluctuations with Fluctuations of Water and Carbon Dioxide, Paranal June 2007

Doc. No.	UL-TRE-MID-15829-0113
Issue	1
Date	March 14, 2008

Prepared	Richard J. Mathar	March 14, 2008	
			Signature
Approved	Walter J. Jaffe	March 14, 2008	
			Signature
Released			
			Signature

Change Record

Issue	Date	Section/Parag. affected	Reason/Initiation/Documents/Remarks
0.1.185	04-Jul-2007	all	created (rjm)
1.0	13-Mar-2008	all	first official release (rjm)

Contents

List of Figures

List of Tables

1 OVERVIEW

1.1 Scope

Fluctuations of water and carbon dioxide densities have been measured by W. J. Jaffe and R. S. Le Poole on the roof top of the VLTI control building, in the VLTI tunnel, and the hull of the VST dome with a LI-COR gas analyzer at the end of June 2007 [16].

During four nights in the same period, the fringe tracker of the MIDI/VLTI interferometer collected data on the motion jitter at the mid-infrared wavelength of 10 μm. We combine a subset of 30 of these exposures on visibility calibrators—each of a duration of approximately 2 minutes—where an overlap with ambient LI-COR data exists. A quantitative comparison between phase power spectra and structure functions is drawn here; the adjective "quantitative" indicates that not only the power exponents of these spectra are examined—which has been done before in OI [2] and will not be reviewed—but also the strength of the turbulence, commonly associated with various seeing parameters.

1.2 Data Sources

This manuscript has drawn information from

- a one-time campaign with a loaned LI-COR water/carbon-dioxide gas analyzer, June 25–30, 2007 [16].
- an ASCII interface to the temperatures, pressures, relative humidities, wind directions, wind velocities and seeing parameters stored in the Paranal ambient server data base [19].
- data on precipitable water vapor, wind speed and wind direction on the 300 mbar level (height) originating from the ECMWF.
- characterisation of interferometric geometry (including air mass), snapshots of the ambient meteorology and seeing, and stored in FITS files of MIDI raw data of four nights overlapping with the gas analyzer data during 30 exposures of approximately 2 minutes duration (each).
- data reduction products of the same MIDI detector data with the MIDI prism, equivalent to a spectral resolution of roughly 32 channels in the N band,
- Temperatures and relative humidities of four sensors in the VLTI tunnel and ducts copied from a directory on ESO's anonymous `ftp` server.

1.3 References

[1] Clifford, S. F. 1971, J. Opt. Soc. Am., 61, 1285

[2] Colavita, M. M., Shao, M., & Staelin, D. H. 1987, Appl. Opt., 26, 4106

[3] d'Arcio, L. 1995, Differential anisoplanatic OPDs and OPD spectra for the VLTI at Cerro Paranal from PARSCA 1992 Balloon Data. VLT-TRE-ESO-15000-0835

[4] de Mooij, E. 2006, Atmospheric turbulence measured with MIDI, Tech. rep.

[5] Fried, D. L. 1965, J. Opt. Soc. Am., 55, 1427. E: [6]

[6] — 1966, J. Opt. Soc. Am., 56, 410E

[7] Hufnagel, R. E., & Stanley, N. R. 1964, J. Opt. Soc. Am., 54, 52

[8] Koehler, B. 2000, Results of OPD measurement on UT#3 in May '00, Test Report. VLT-TRE-ESO-15000-2258

[9] Koresko, C., Colavita, M., Serabyn, E., Booth, A., & Garcia, J. 2006, in Advances in Stellar Interferometry, edited by J. D. Monnier, M. Schöller, & W. Danchi (Int. Soc. Optical Engineering), vol. 6268, 626817

[10] Labit, P. 1998, Meteorological Prediction Software, User and Maintenance Manual. VLT-TRE-ESO-17443-1678

[11] Lévêque, S. 2002, Temperature sensor network for the VLTI. VLT-TRE-ESO-15000-2532

[12] Marchetti, S., & Simili, R. 2006, Infr. Phys. Techn., 47, 263. Presumbably, the factor 10^{-4} ought read 10^{+4} and the temperature 296 °C read 23 °C in Table 1.

[13] Mathar, R. J. 2006, Astrometric Survey for Extra-Solar Planets with PRIMA, Astrometric dispersion correction. UL-TRE-AOS-15753-0010

[14] — 2007, Baltic Astronomy, 16, 287

[15] — 2007, J. Opt. A: Pure and Appl. Optics, 9, 470

[16] Mathar, R. J., Jaffe, W. J., & Le Poole, R. S. 2007, High Frequency Fluctuations of Water and Carbon Dioxide, Paranal July 25–27, 2007. UL-TRE-ESO-15000-0836

[17] Roddier, F. 1981 (Amsterdam: North Holland), vol. XIX of Prog. Opt., 281–376

[18] Roddier, F., & Lena, P. 1984, J. Optics (Paris), 15, 171

[19] Sarazin, M. 2003, Astroclimatology of Paranal, Tech. rep., European Southern Observatory. URL http://www.eso.org/gen-fac/pubs/astclim/paranal

[20] Schwider, J. 1990 (Amsterdam: Elsevier), vol. 28 of Prog. Opt., 271–359

1.4 Acronyms

AO Adaptive Optics

DICB Data Interface Definition Board (of ESO) http://archive.eso.org/dicb

DL Delay Line

ECMWF European Center for Medium-Range Weather Forecasts http://www.ecmwf.int/

ESO European Southern Observatory http://www.eso.org

FITS Flexible Image Transport System http://fits.gsfc.nasa.gov

FT Fourier Transform

GPS Global Positioning System

GUI Graphical User Interface

IDL Interactive Data Language http://www.uni-giessen.de/hrz/software/idl/

IR Infrared

IRIS Infrared Image Sensor http://www.eso.org/projects/vlti/iris/

ISS Interferometric Supervisor-Software

MDL main delay line
http://www.eso.org/outreach/press-rel/pr-2000/phot-26-00.html

MIDI Mid-Infrared Interferometric Instrument http://www.mpia.de/MIDI

NOVA Nederlandse Onderzoekschool voor Astronomie
http://www.strw.leidenuniv.nl/nova/

OI Optical Interferometry http://olbin.jpl.nasa.gov/

OPD optical path difference

OS Observation Software

PDF Power Density Function http://en.wikipedia.org/wiki/Spectral_density

PWV precipitable water vapor

UT Unit Telescope (of the VLTI) http://www.eso.org/projects/vlt/unit-tel/

UTC Universal Time Coordinated

VLT Very Large Telescope http://www.eso.org/

VLTI Very Large Telescope Interferometer http://www.eso.org/vlti

VST VLT Survey Telescope http://vstportal.oacn.inaf.it/

2 FITTED DISPERSED MIDI SCANS

2.1 Parameters: times, baselines, meteorological

An overview of the time allocation of the 30 MIDI exposures in the four nights is in Figure 1. Some parameters extracted from the primary headers of the first in each group of FITS files of an exposure are in table 1.

- The first column is a small integer to avoid tagging with the full standard file name that is given in the second column.
- Baselines are listed in the third column.
- Two temperatures along the DL tunnel are in the 4th and 5th column, taken from the keywords `ISS TEMP TUN1` and `ISS TEMP TUN4` [11].
- P is the column with the projected baseline, `ISS PBL12 START`.
- D and $\dot{D}$ are the external path delay (in vacuum) and its time derivative, using `LST`, `OCS ISS RA` and `OCS ISS DEC` as inputs. The sum $b^2 = P^2 + D^2$ is the squared baseline length and constant for a pair of stations, $b = 46.4$ m (46.6 m according to the distance between the station coordinates in the OPD model of `Mfile22`) for `UT23` and $b = 62.4$ m for `UT34`.
- The column τ_0 is the mean of `AMBI TAU0 START` and `AMBI TAU0 END`.
- The column $\partial T/\partial h$ is the value of `AMBI LRATE`.
- The column `AIRM` is the air mass of `ISS AIRM START`.

The detector cycle time (average distance between start of two exposures) was 20.9 ms (49 Hz) in all cases. These are non-chopped observations which basically ensures that the stream of data fills the time axis almost continuously. The number of piezo steps per scan was 40 in all cases (keyword `PIEZ POSNUM`), which means block adjustments of the internal or main delay lines initiated by the MIDI fringe tracker could occur in intervals of 0.836 seconds. (This is roughly equivalent to the mean passage time for a UT diameter at characteristic wind speeds of 10 m/s.) Multiplication with $\dot{D}$ of Table 1—which is of the order of 1 mm/s—gives an estimate of how much the main delay line moved during that time.

Some additional characterization of the seeing conditions is in Figure 2; its data will not be used in the followup analysis.

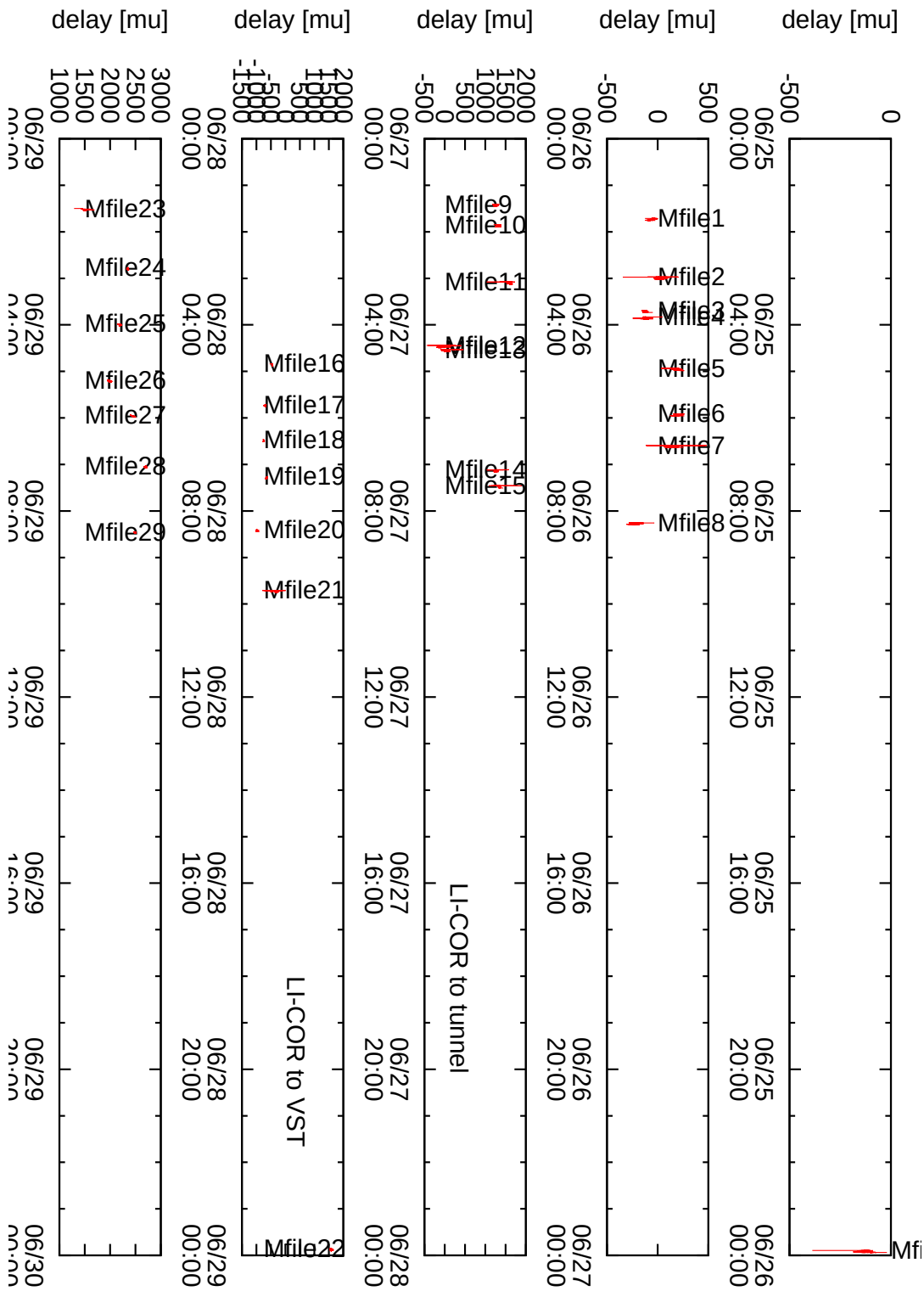

Figure 1: Timing overview of the four nights with MIDI data files.

MFile*n*	ARCFILE start	TELESCOP stations	TUN1 T West (°C)	TUN4 East (°C)	PBL12 P (m)	D (m)	$\dot{D}$ (mm/s)	TAUO τ_0 (ms)	LRATE $\partial T/\partial h$ (°C/m)	AIRM	WINDSP (m/s)
0	MIDI.2007-06-25T23:53:33	U34	13.49	14.27	62.3	4.0	-1.2	1.00	-0.0143	1.478	11.90
1	MIDI.2007-06-25T01:42:35	U34	12.96	14.41	61.9	6.2	-0.7	1.18	-0.0054	1.451	12.78
2	MIDI.2007-06-26T02:58:18	U34	13.37	14.31	62.2	6.2	-0.7	0.95	-0.0100	1.730	10.73
3	MIDI.2007-06-26T03:41:14	U34	13.38	14.36	58.5	-21.8	-3.6	1.24	-0.0139	1.067	11.68
4	MIDI.2007-06-26T03:49:39	U34	13.32	14.35	57.8	-23.6	-3.5	1.21	-0.0136	1.080	11.38
5	MIDI.2007-06-26T04:56:08	U34	13.29	14.34	43.8	44.6	-1.3	0.94	-0.0171	1.779	11.53
6	MIDI.2007-06-26T05:54:39	U34	13.39	14.37	58.3	22.6	-2.9	0.81	-0.0171	1.122	8.98
7	MIDI.2007-06-26T06:35:22	U34	13.34	14.42	50.9	36.2	-2.1	0.84	-0.0275	1.382	8.68
8	MIDI.2007-06-26T08:15:15	U34	13.22	14.49	49.5	38.1	-3.4	0.83	-0.0504	1.323	8.48
9	MIDI.2007-06-27T01:24:27	U23	13.41	14.50	45.2	-11.4	-0.8	0.78	-0.0121	1.267	16.25
10	MIDI.2007-06-27T01:50:36	U23	12.36	14.43	44.9	-12.7	-0.9	0.78	-0.0107	1.228	14.73
11	MIDI.2007-06-27T03:04:41	U23	12.09	14.44	39.9	-24.2	-1.5	0.60	-0.0282	1.183	17.10
12	MIDI.2007-06-27T04:26:37	U23	12.30	14.49	46.0	-7.7	0.2	0.83	-0.0304	1.967	15.88
13	MIDI.2007-06-27T04:31:47	U23	12.29	14.51	46.0	-7.7	0.2	0.87	-0.0268	1.925	16.00
14	MIDI.2007-06-27T07:06:52	U23	12.30	14.52	45.8	-8.9	-0.7	0.94	-0.0304	1.289	15.15
15	MIDI.2007-06-27T07:27:32	U23	12.31	14.44	45.7	-9.2	-0.8	0.97	-0.0357	1.228	16.58
16	MIDI.2007-06-28T04:50:12	U34	12.88	14.35	60.6	-15.1	-1.4	3.12	-0.0189	1.449	13.45
17	MIDI.2007-06-28T05:42:41	U34	13.16	14.37	56.8	-26.0	-3.7	3.22	-0.0111	1.104	9.93
18	MIDI.2007-06-28T06:27:47	U34	13.08	14.43	54.6	-30.4	-2.0	3.44	-0.0132	1.356	10.53
19	MIDI.2007-06-28T07:15:28	U34	13.08	14.50	39.2	48.7	-1.4	4.73	-0.0061	1.869	8.90
20	MIDI.2007-06-28T08:23:48	U34	13.28	14.56	46.9	-41.3	-3.2	2.68	-0.0304	1.399	8.43
21	MIDI.2007-06-28T09:42:30	U34	13.19	14.64	58.0	23.2	-3.4	1.91	-0.0671	1.983	9.93
22	MIDI.2007-06-28T23:51:18	U23	13.34	14.64	46.6	2.1	-0.4	2.68	-0.0236	1.397	9.13
23	MIDI.2007-06-29T01:29:51	U23	13.37	14.65	46.6	1.4	-0.7	2.98	-0.0218	1.264	9.80
24	MIDI.2007-06-29T02:46:08	U23	13.39	14.63	45.8	-8.7	-1.5	2.94	-0.0039	1.054	8.23
25	MIDI.2007-06-29T03:58:27	U23	13.39	14.55	46.4	4.5	-1.7	3.11	-0.0054	1.016	7.72
26	MIDI.2007-06-29T05:11:09	U23	13.41	14.56	43.6	-16.5	-1.8	2.89	-0.0089	1.071	6.95
27	MIDI.2007-06-29T05:56:11	U23	13.40	14.64	46.2	-6.1	-2.1	2.71	-0.0032	1.011	7.80
28	MIDI.2007-06-29T07:01:57	U23	13.42	14.52	42.8	-18.4	-2.2	2.43	-0.0021	1.173	6.50
29	MIDI.2007-06-29T08:26:56	U23	13.47	14.47	39.2	-25.3	-2.0	3.28	-0.0346	1.336	7.00

Table 1: Parameters of the 30 MIDI data sets derived from primary FITS headers.

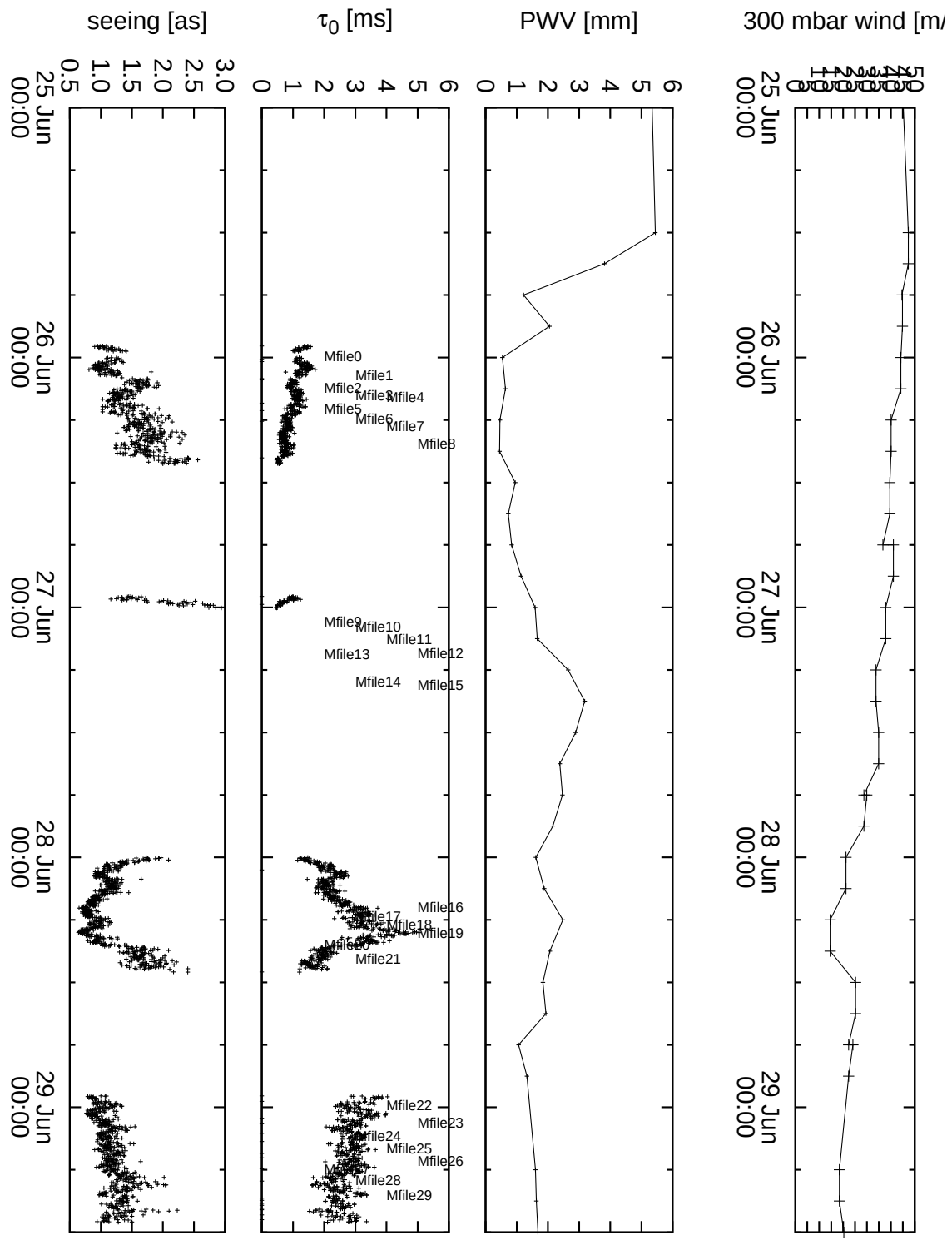

Figure 2: Upper two plots: The wind velocity during the five days of observation at the 300 mbar pressure level, and the precipitable water vapor, from the ECMWF [10, 19]. The PWV plot is a section of Figure 57 in [13]. Lower two plots: seeing and coherence time from the ambient data base server at the same times. The 25th of June is included in the plot to demonstrate implicitly through the PWV that it was rainy.

Fig. 3 is a close-up (redundant) view on the wind speeds of Figs. 2–7 of [16] during the times of the 30 MIDI observations, a synopsis of the `WINDSP` column of Table 1 with the markers of Fig. 1. The intent is to demonstrate that the wind speed is stable over the approximate 2 minutes of an exposure only to within 0.5 m/s. The `WINDSP` entry in the FITS headers are (due to some known constraints of data handling procedures in the instrument software) a snapshot taken at some time during the part of the exposure covered by the first FITS file of the series; the nominal accuracy of 0.01 m/s is not achieved.

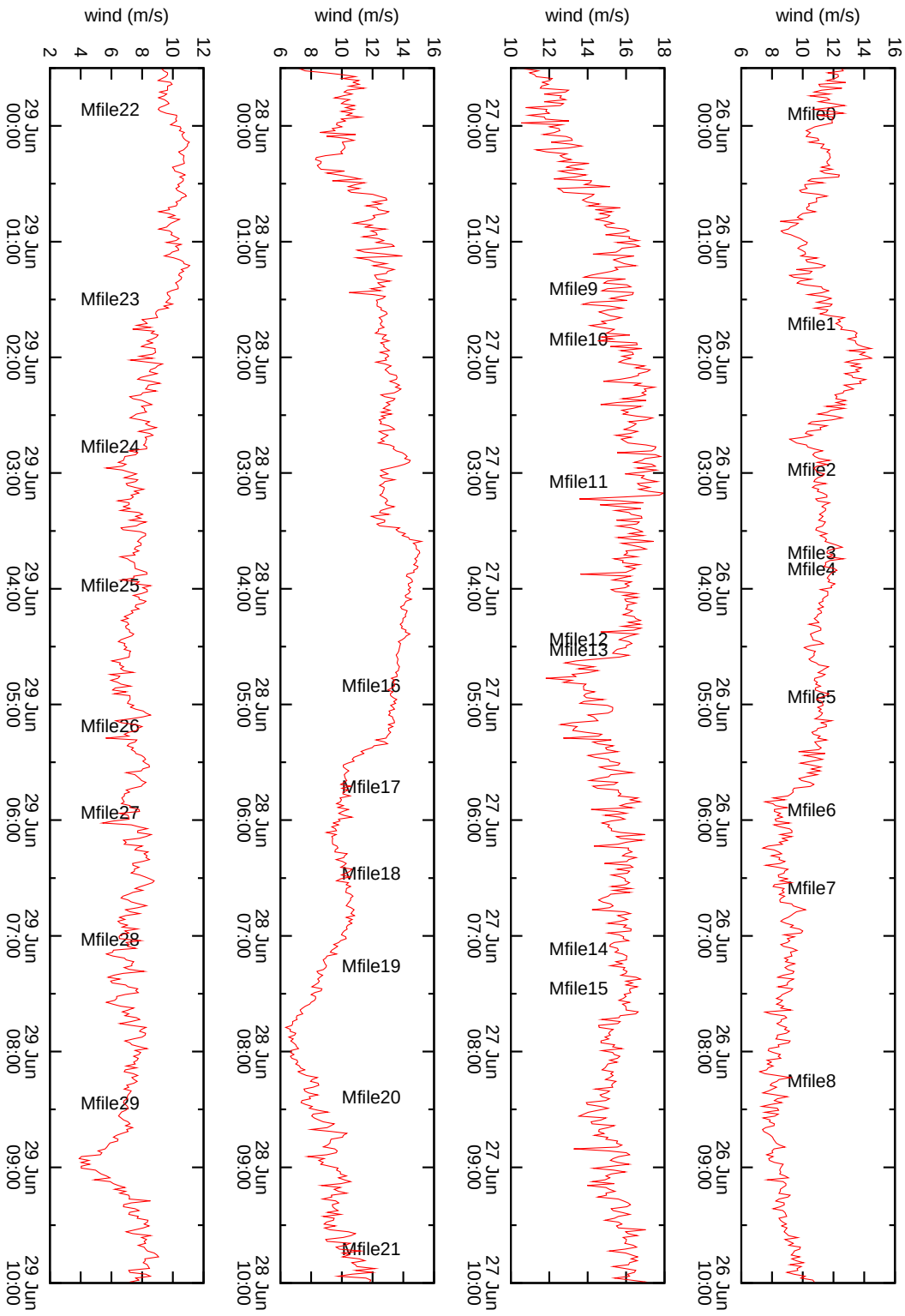

Figure 3: Ground wind speeds from the ambient server database during the MIDI observations.

2.2 Reduction of Dispersion with Linear Fits to Wavenumber

The interferometric phase φ

$$\varphi = n(k)kD_i - kD_e \tag{1}$$

measured at wave vectors $k = 2\pi\sigma$ at internal (stepped) delays D_i, external geometric path delay D_e for nominal refractive index $n(k)$ is fitted over the MIDI band width to a model of constant interband group delay [9]

$$\varphi = \varphi_0 + k\varphi'. \tag{2}$$

This is a self-sustained data reduction without "astrometric" support, which means the input is essentially the cosine of φ, so φ_0 is only determined modulo 2π. The algorithm is essentially the technique of taking the FT of the interferograms and putting a window around one of the two side bands that arise from splitting the cosine with the Euler formula [20, §3.4].

Some cleansing of the 2-parametric reduced data is done before display and further use of ϕ_0 and ϕ':

- At the start of some MIDI files, the initial time segment shows the behaviour during fringe acquisition, with much larger changes than for the rest of the approximately 2 1/2 minutes covered in total. Chopping off some initial frames of the MIDI exposures—typically a sequence of fringe acquisition—leads to modified start times of the exposures of Table 2. For exposures with index 12, Fig. 16, such a simple way of discarding data is not effective and has not been attempted.
- Some spikes in φ' are removed: frames where $\Delta\varphi'$ differs from the average of the previous 15 frames by more than 20 μm are discarded. This removes data which claim an OPD motion of more than 20 μm within 0.3 seconds.
- One second is chopped off the end to remove the tail wiggle.

In each of the figures 4–33

- The top 4 plots show data as a function of UTC. Each small vertical bar represents the spread of values within an individual second, so we have 60 of these per major tic mark on the time axis.
- the two plots with ordinate φ_0 and φ' show the MIDI parameters reduced to φ_0 (in units of cycles, ie, 2π) and reduced to φ' (in units of μm) after this removal of some optional initial number of frames.
- the plots carrying ordinate units of some powers of mol/m^3 summarize the LI-COR measurements at its local position (outdoors or tunnel) during that same time. The CO_2 densities are as monitored, the water densities transformed with the linear equation (1) of [16] for `Lfile6` and later. The power spectral density derived for the water vapor is the third plot from below. The enumeration `Lfile1`—`Lfile10` is the same as in [16].
- The MIDI phase fluctuation at $\lambda = 10$ μm, the value

  $$\varphi(10\mu) \equiv \varphi_0 + 2\pi\varphi'/(10\mu\text{m}) \tag{3}$$

  that combines the two variables φ_0 and φ' of each MIDI frame, is transformed to the PDF of φ and φ_0 with ordinate units rad^2/Hz. A local maximum in PDF_{φ_0} near 1.2 Hz with occasional ghosts at multiples seems to be some artifact of the data reduction algorithm, where 1.2 Hz is the inverse of the period of the sawtooth pattern of the phase shifting internal delay line.

- In PDF plots, the frequency abscissa axis is accompanied by a second logarithmic axis, which shows wave numbers
$$\sigma \equiv \nu/v \tag{4}$$
in units of inverse meters associated with the frequencies ν by the individual wind velocity v during that observation (Fig. 3 and Table 1). They are inverse length scales of the density fluctuations assuming constant speed during the exposure.

As mentioned earlier, the Nyquist frequency of the LI-COR data is 10 Hz, the Nyquist frequency of the MIDI data 25 Hz. In all spectra and structure functions, a linear drift term has been removed before the Fourier transform; the sub-plots with the data as a function of UTC time show the data prior to this transformation. The spectra appear noisier than those of Fig. 29–45 in [16] because an additional averaging on the time axes has been introduced in Fig. 29–45 of [16] for display (but not for calculation of the derived quantities like autocorrelation and structure function) but not here.

The time axis of LI-COR is a PC clock manually adjusted to UTC, whereas the MIDI exposures are clocked with a GPS based system with sub-second accuracy. A relative shift of the two time axes of the order of 2 seconds is expected.[1] The PDF of the molecular LI-COR water density is calculated over the time interval shown in the upper part of the figures. A linear drift has been removed, and the water density correction (1) of [16] is made for all measurements in the tunnel and in the VST.

[1]The `UTC` keyword of the MIDI primary headers does not show the start of the exposures but a time when ISS received some specific message from the MIDI OS. This is typically 8 seconds ahead of the values of `MJD-OBS` and `OBS-DATE` which should be used for accurate reference of the start of exposures.

Mfile*n*	start	`ALT` (deg)	`AZ` (deg)
0	2007-06-25T23:53:45	42.509	15.839
1	2007-06-25T01:42:47	43.512	9.954
2	2007-06-26T02:58:30	35.245	13.849
3	2007-06-26T03:41:26	69.571	108.794
4	2007-06-26T03:49:51	67.571	106.434
5	2007-06-26T04:56:20	34.124	321.301
6	2007-06-26T05:54:52	62.991	328.085
7	2007-06-26T06:35:33	46.294	323.812
8	2007-06-26T08:15:27	49.061	269.363
9	2007-06-27T01:24:39	52.051	333.532
10	2007-06-27T01:50:48	54.498	338.092
11	2007-06-27T03:04:53	57.676	25.906
12	2007-06-27T04:27:16	30.470	321.100
13	2007-06-27T04:32:04	31.209	321.107
14	2007-06-27T07:07:04	50.852	327.679
15	2007-06-27T07:27:44	54.485	329.785
16	2007-06-28T04:50:24	43.570	40.322
17	2007-06-28T05:42:53	64.872	122.506
18	2007-06-28T06:27:59	47.452	66.855
19	2007-06-28T07:15:42	32.262	313.861
20	2007-06-28T08:23:59	45.577	130.046
21	2007-06-28T09:42:42	30.196	226.210
22	2007-06-28T23:51:29	45.663	306.282
23	2007-06-29T01:30:03	52.278	307.147
24	2007-06-29T02:46:19	71.600	346.124
25	2007-06-29T03:58:38	79.934	276.846
26	2007-06-29T05:11:20	69.035	31.843
27	2007-06-29T05:56:22	81.636	66.875
28	2007-06-29T07:02:08	58.453	81.035
29	2007-06-29T08:27:07	48.414	75.355

Table 2: Time stamps of the first exposures in the MIDI data files of Table 1 after optional removal of a variable initial portion (of typically up to 550 frames) which show large variation of the delay parameter. `ALT` and `AZ` are the pointing coordinates in degrees in the local coordinate system following DICB conventions, from the FITS headers.

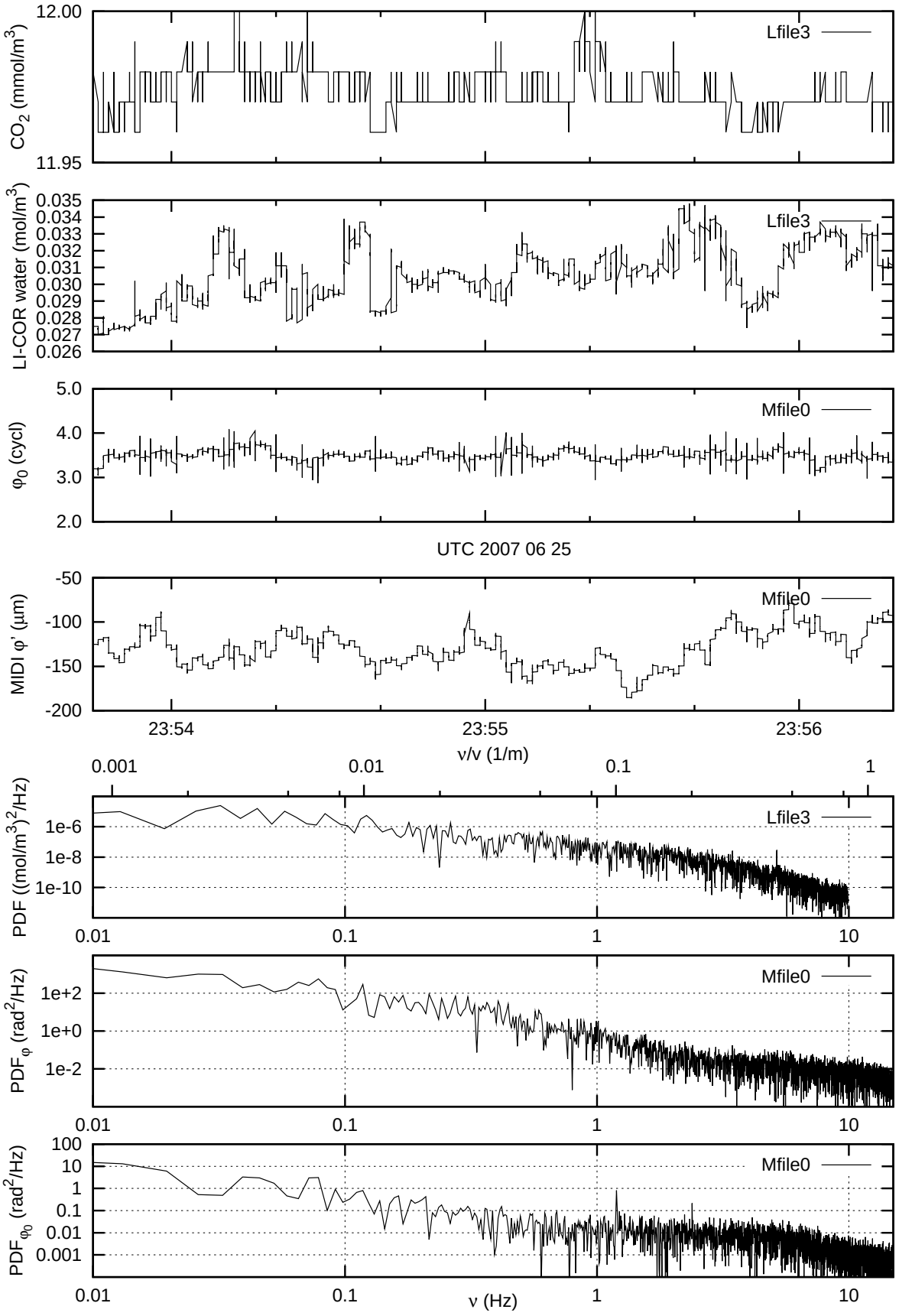

Figure 4: Correlation of MIDI data file 0 with LI-COR densities.

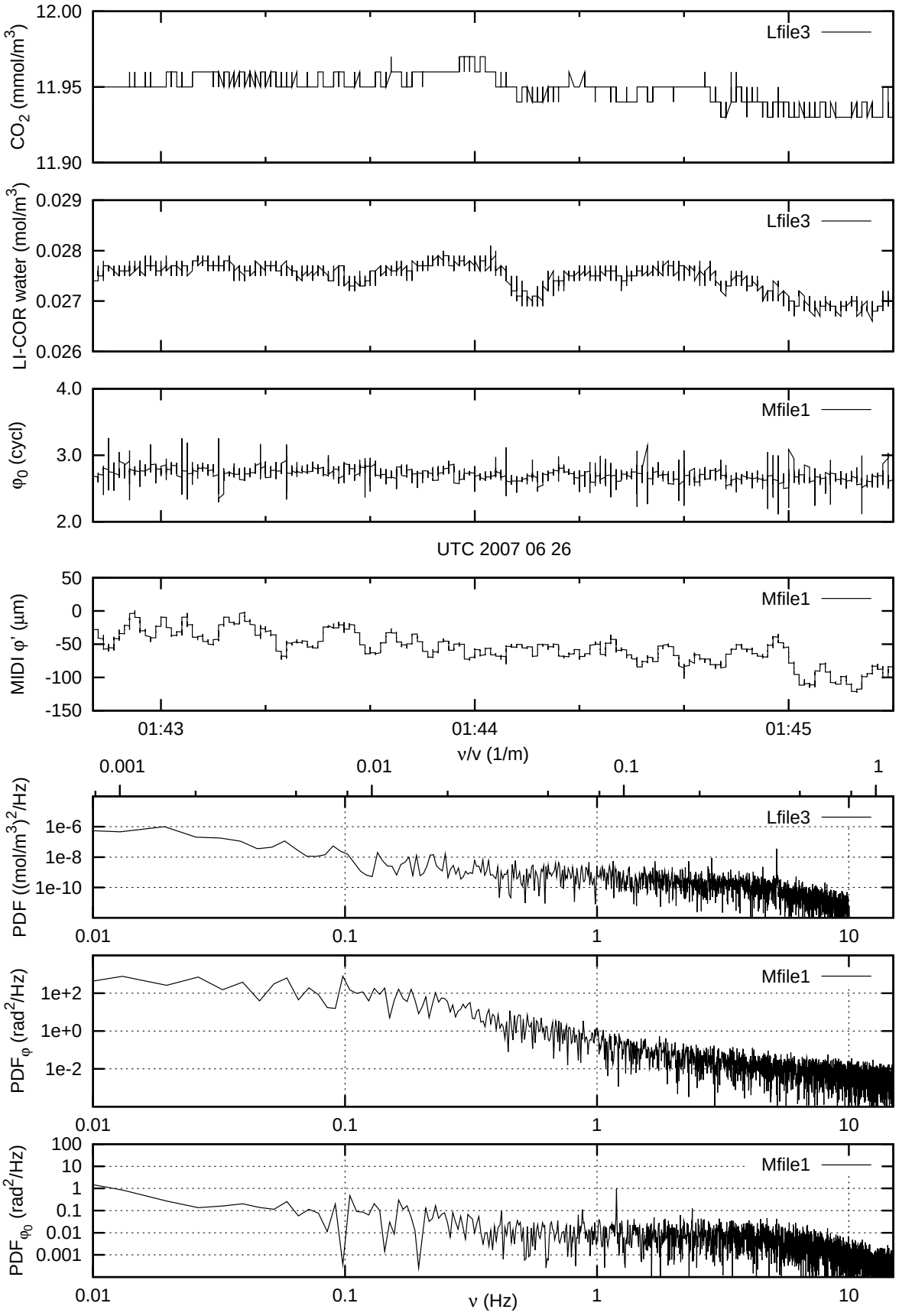

Figure 5: Correlation of MIDI data file 1 with LI-COR densities.

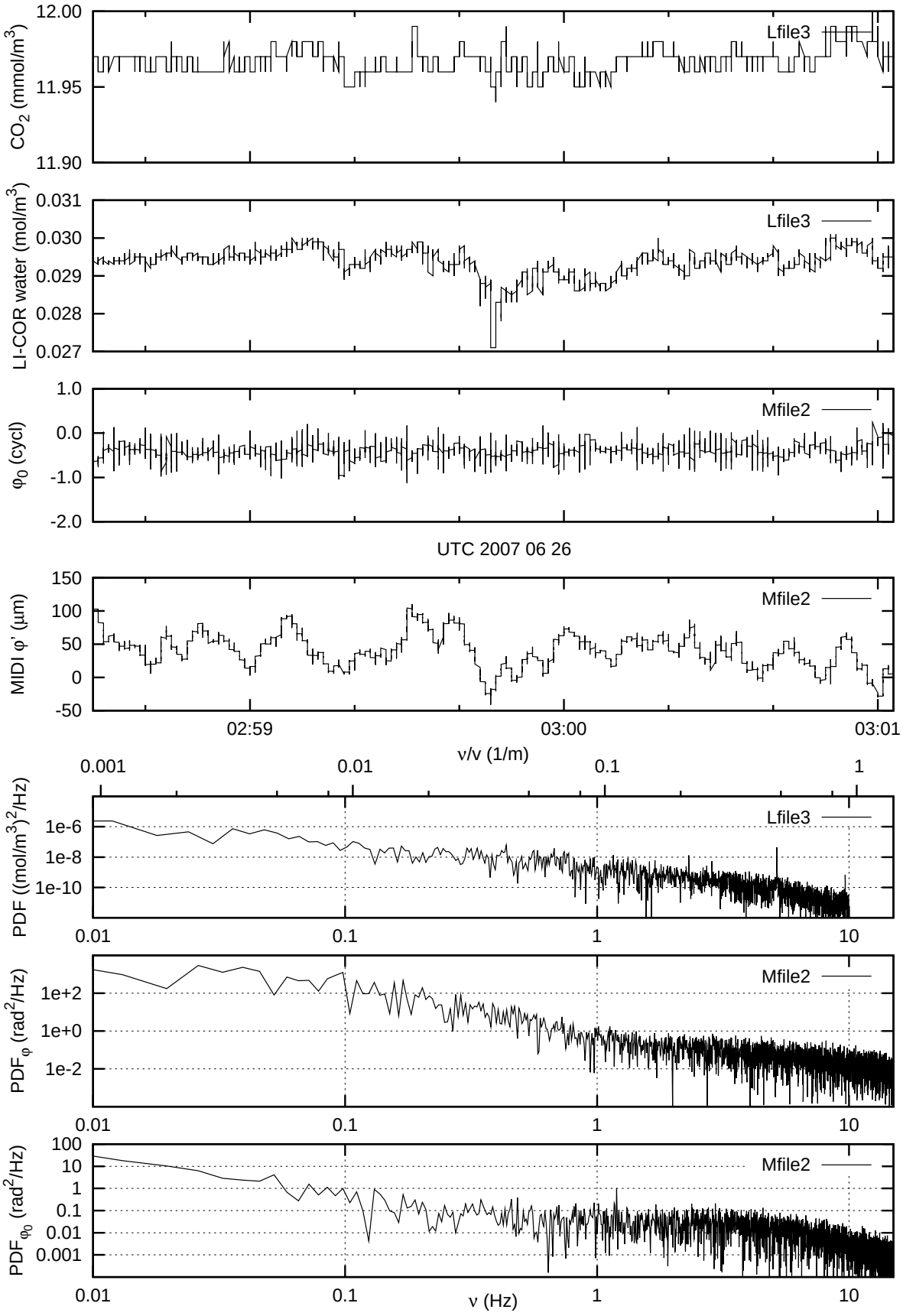

Figure 6: Correlation of MIDI data file 2 with LI-COR densities.

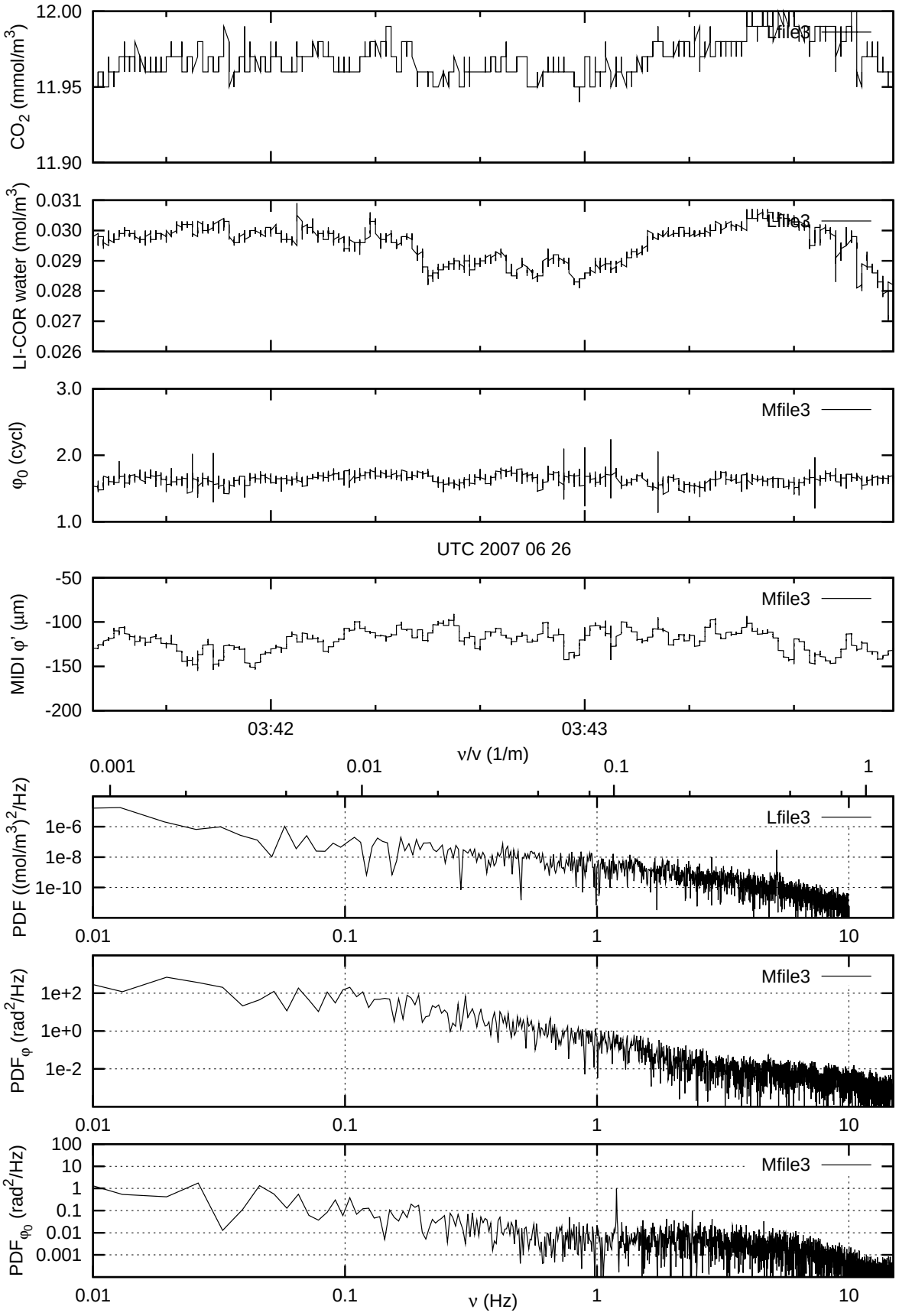

Figure 7: Correlation of MIDI data file 3 with LI-COR densities.

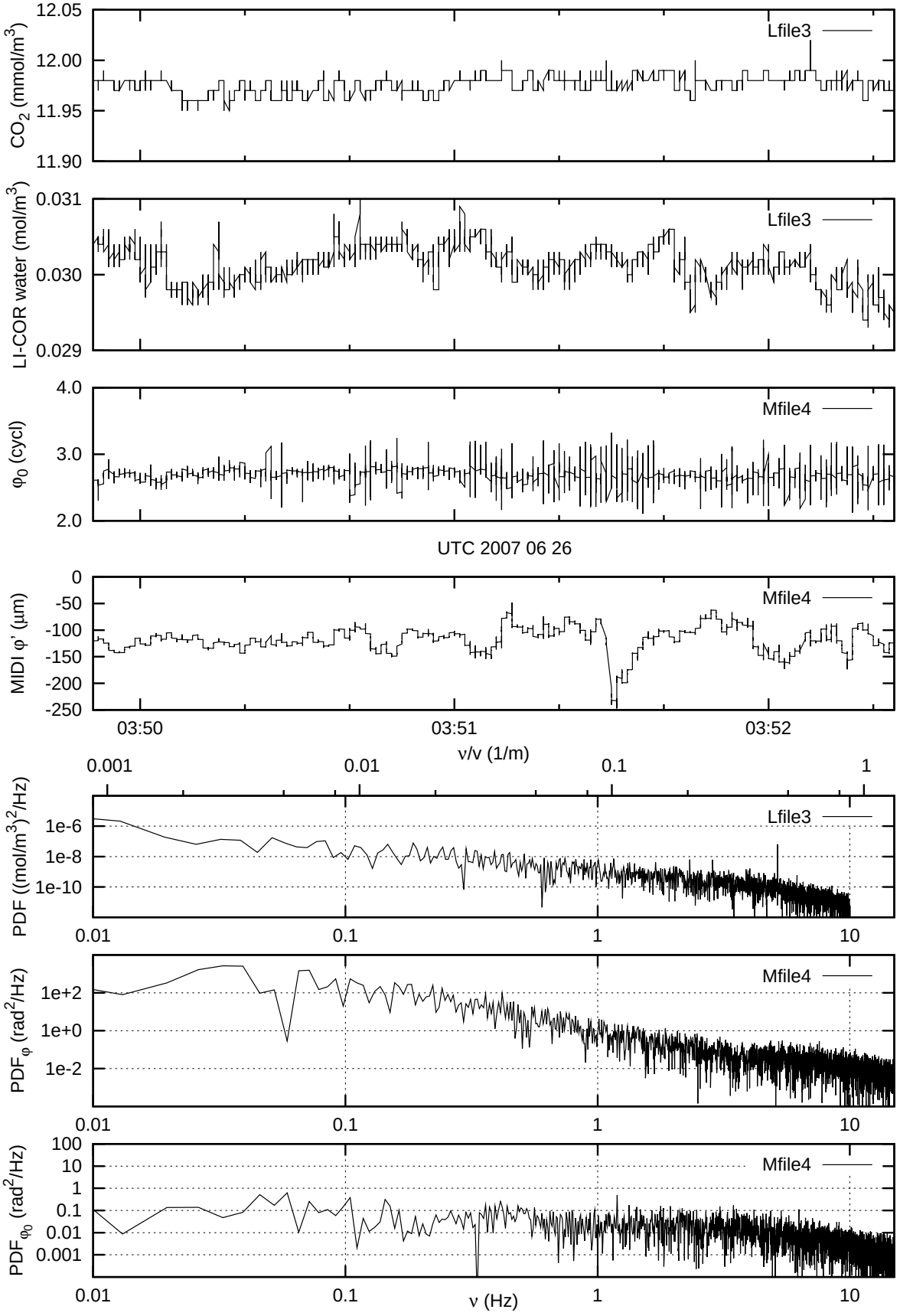

Figure 8: Correlation of MIDI data file 4 with LI-COR densities.

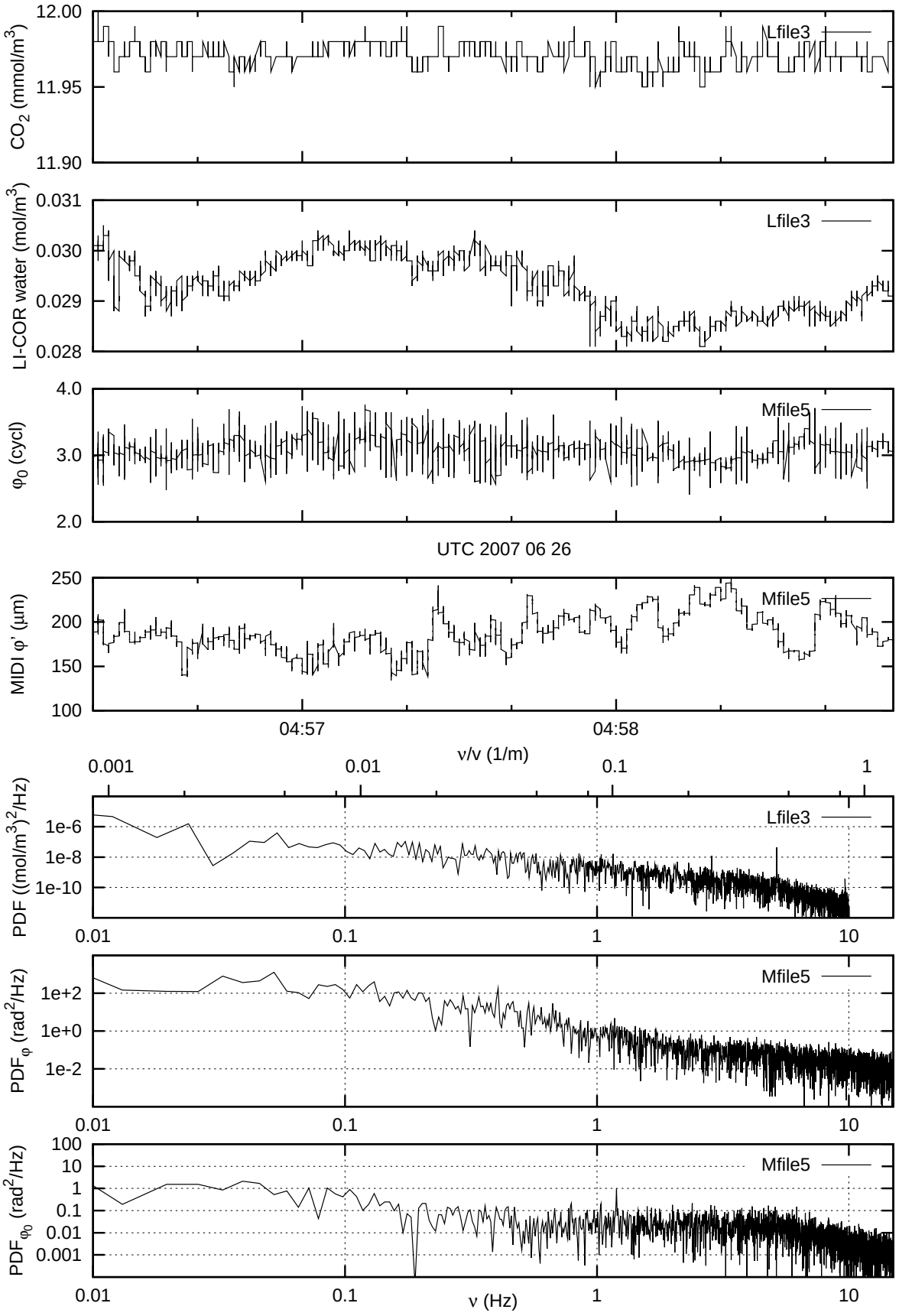

Figure 9: Correlation of MIDI data file 5 with LI-COR densities.

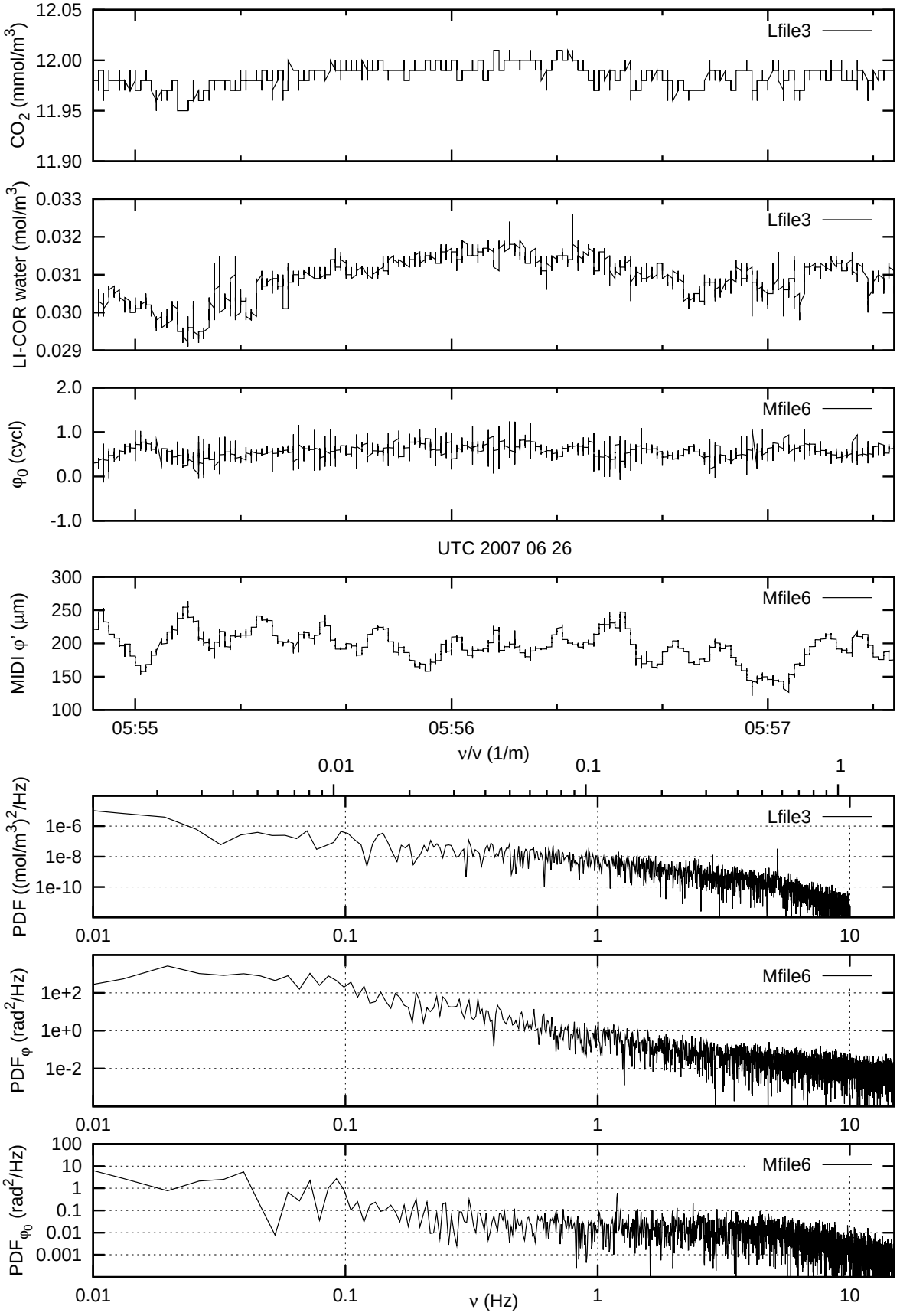

Figure 10: Correlation of MIDI data file 6 with LI-COR densities.

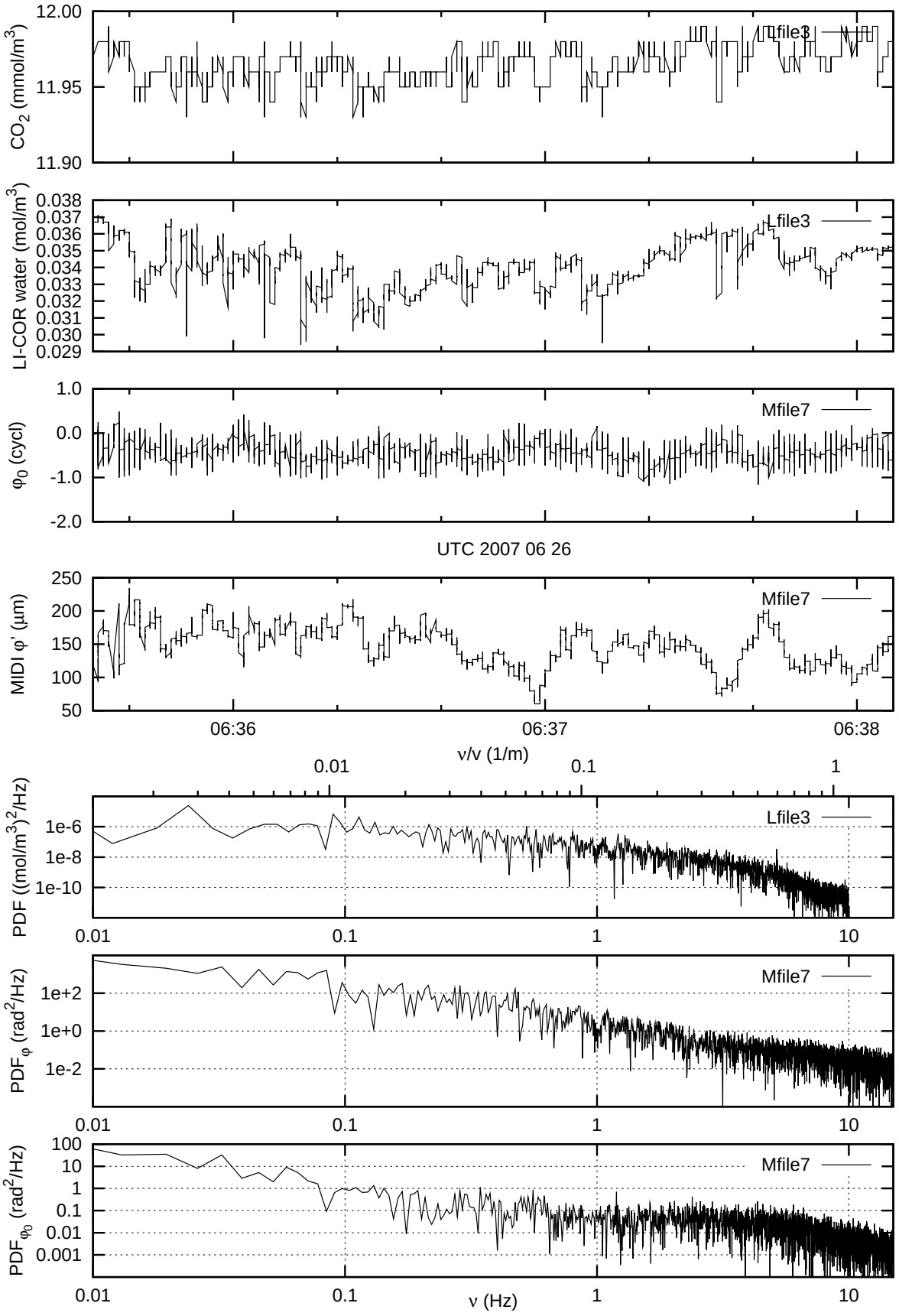

Figure 11: Correlation of MIDI data file 7 with LI-COR densities.

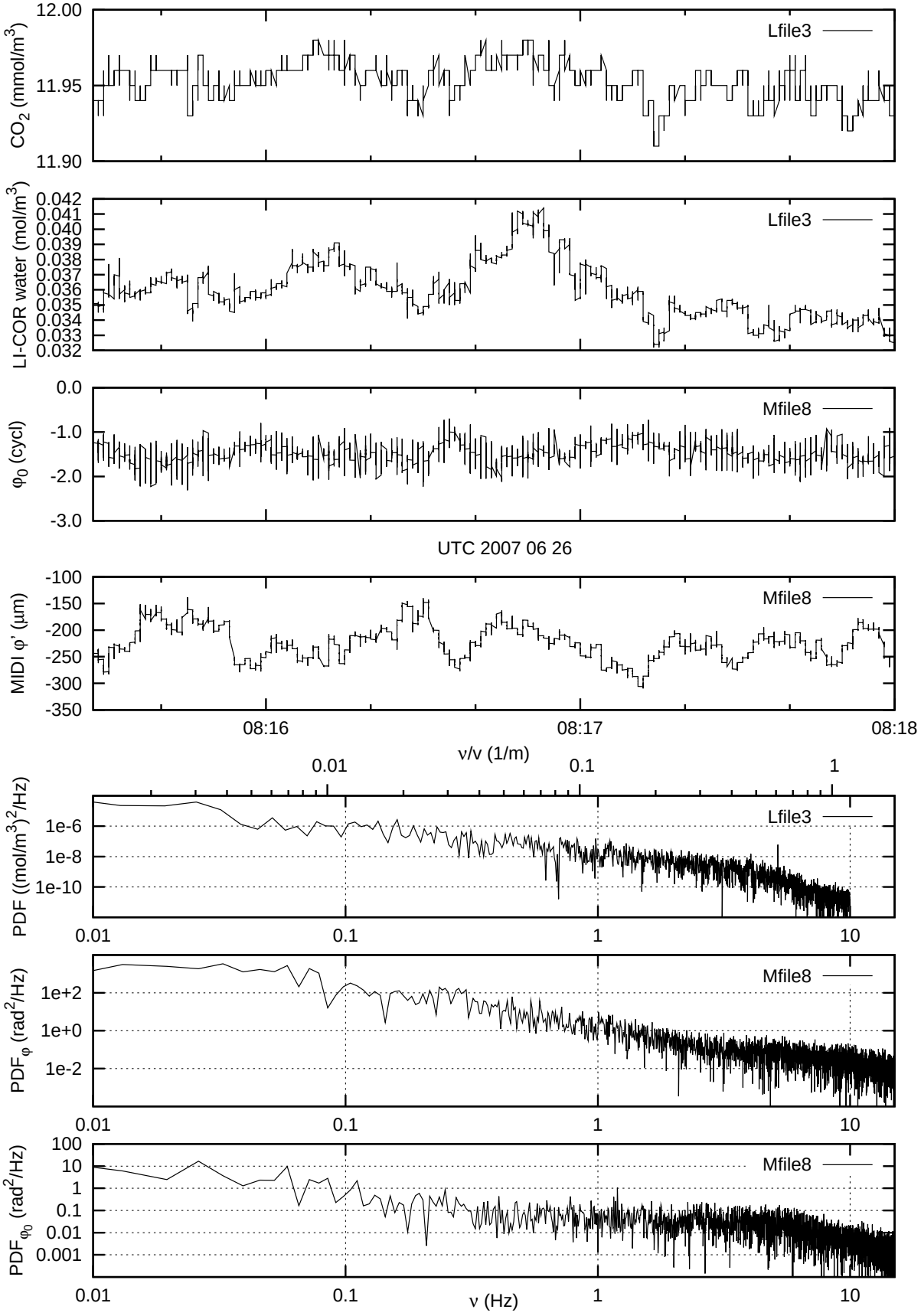

Figure 12: Correlation of MIDI data file 8 with LI-COR densities.

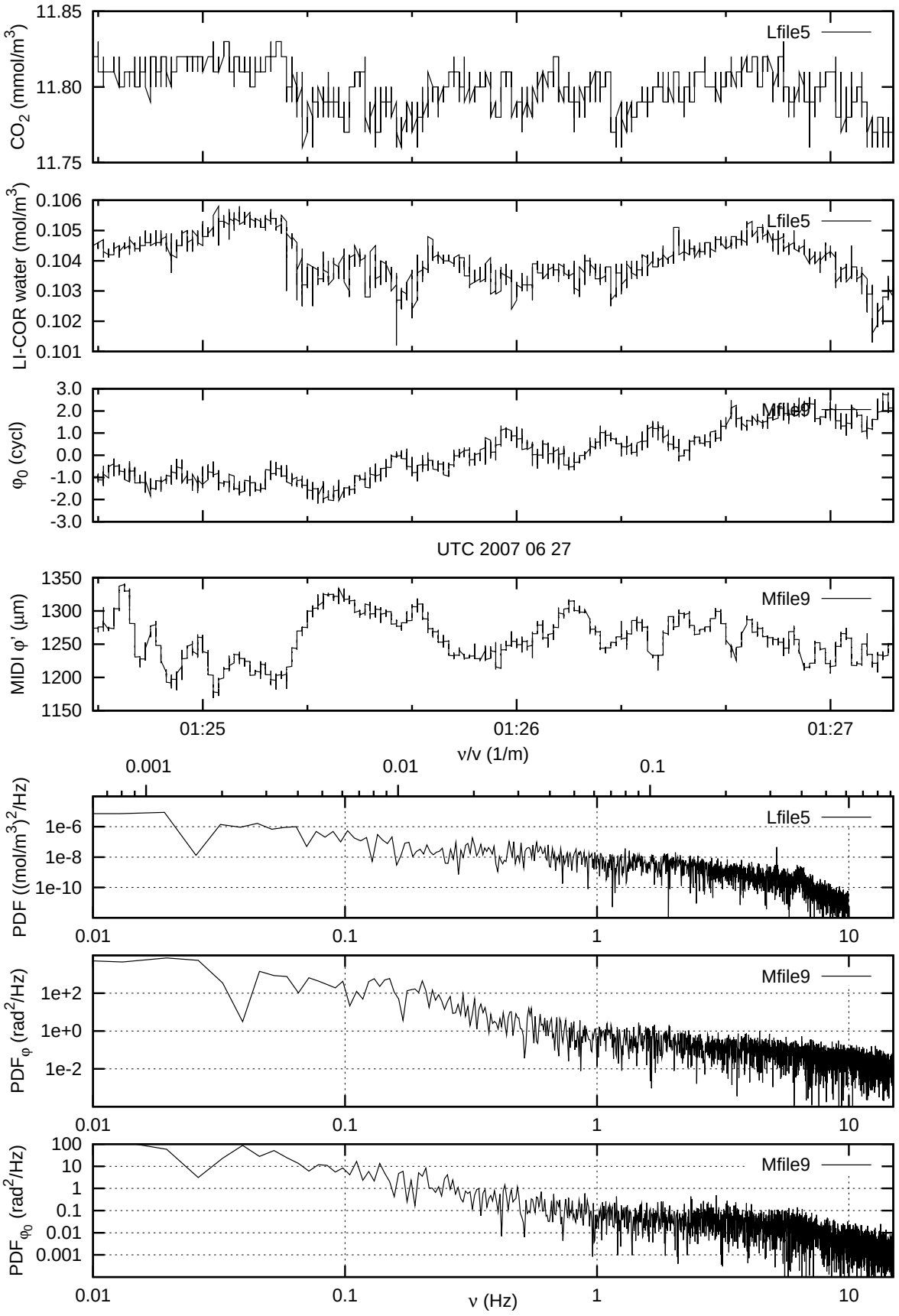

Figure 13: Correlation of MIDI data file 9 with LI-COR densities.

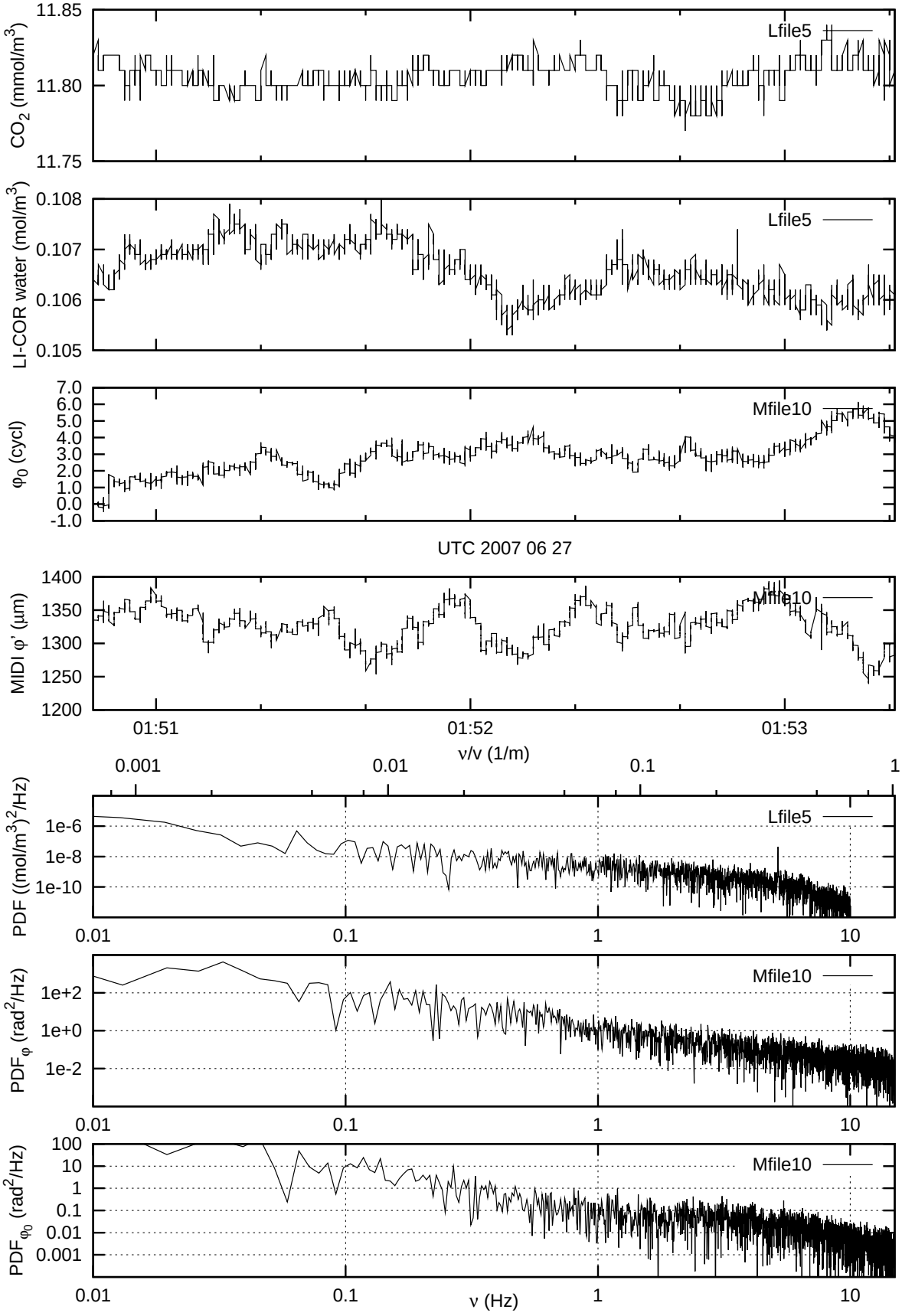

Figure 14: Correlation of MIDI data file 10 with LI-COR densities.

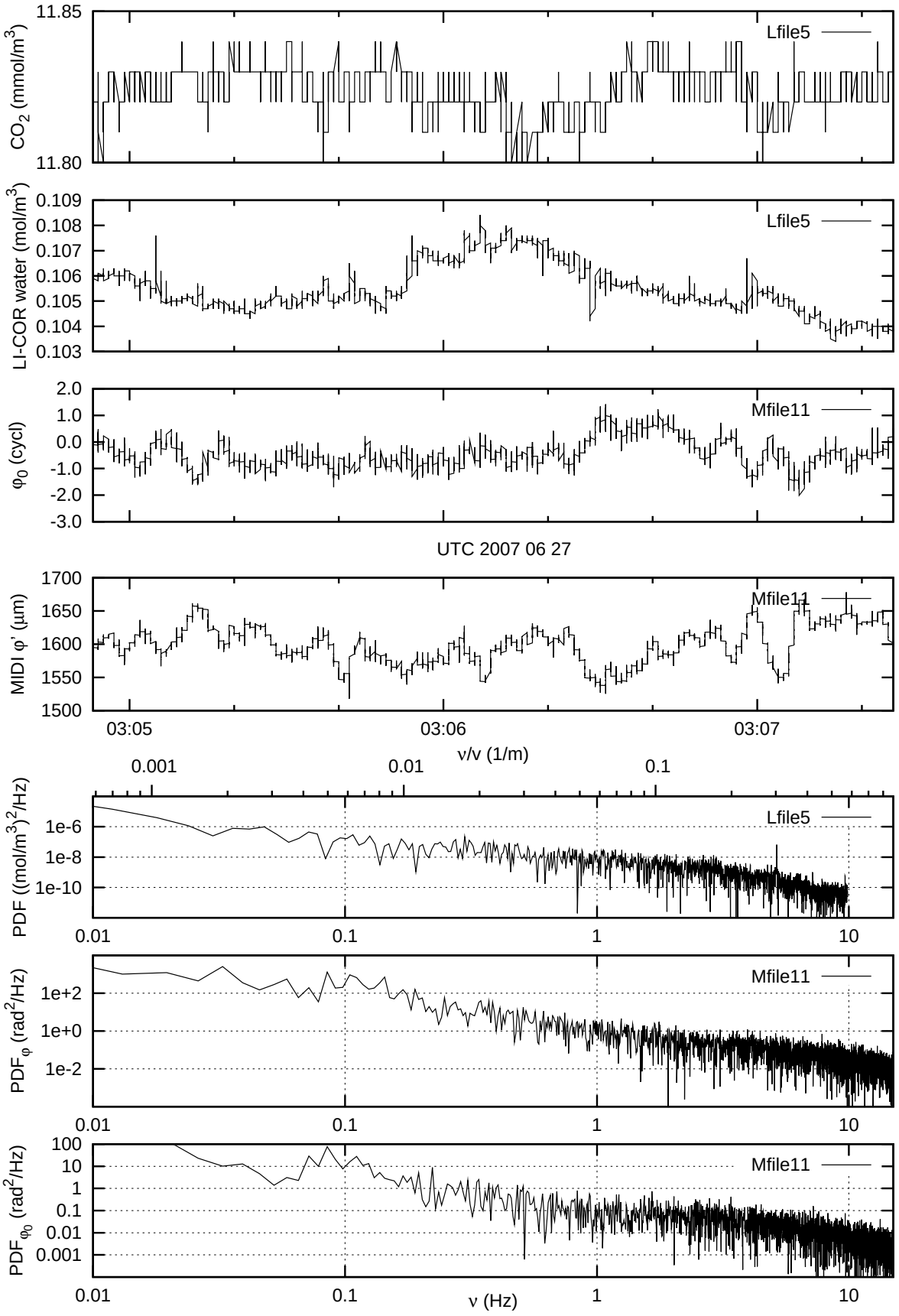

Figure 15: Correlation of MIDI data file 11 with LI-COR densities.

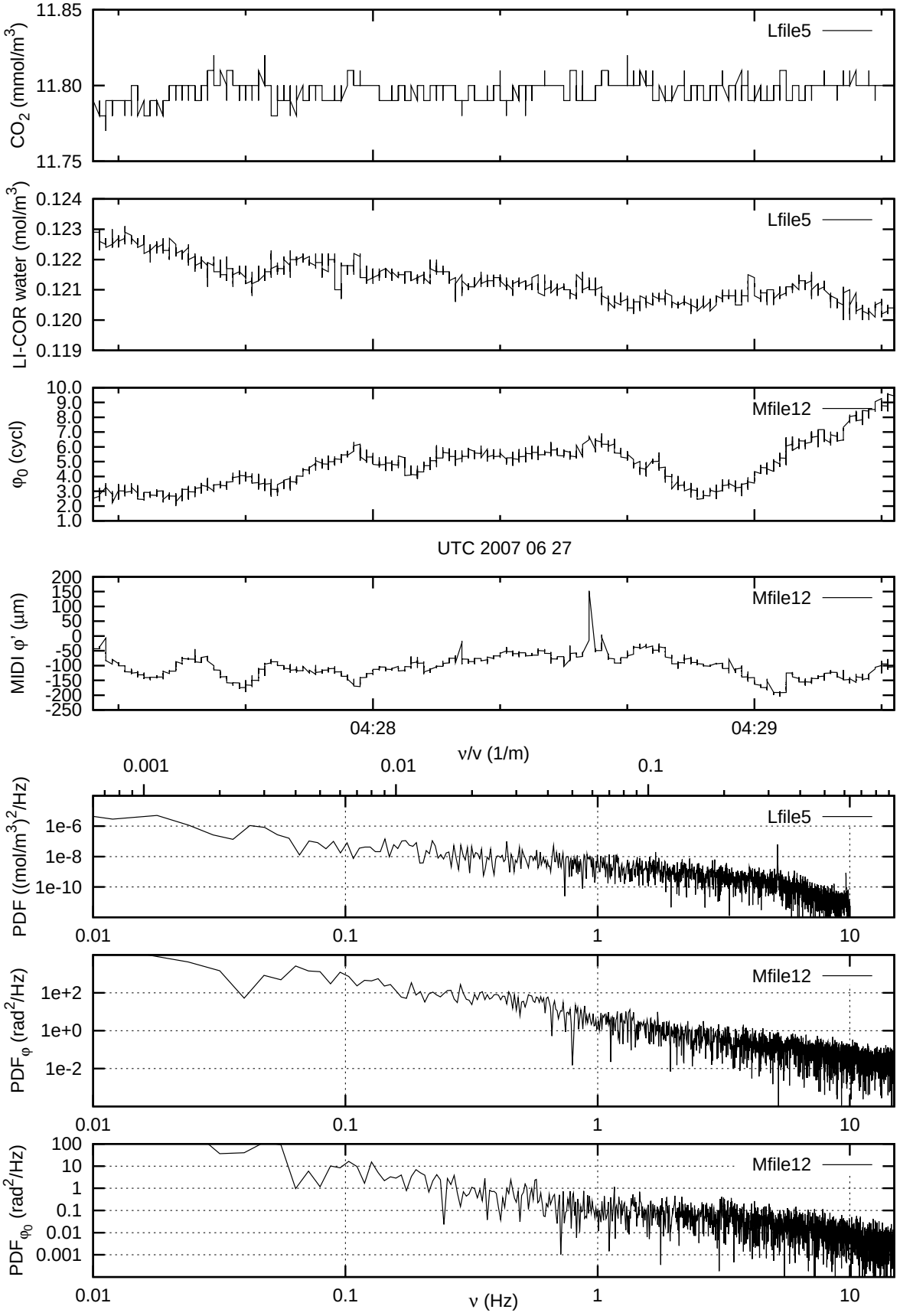

Figure 16: Correlation of MIDI data file 12 with LI-COR densities.

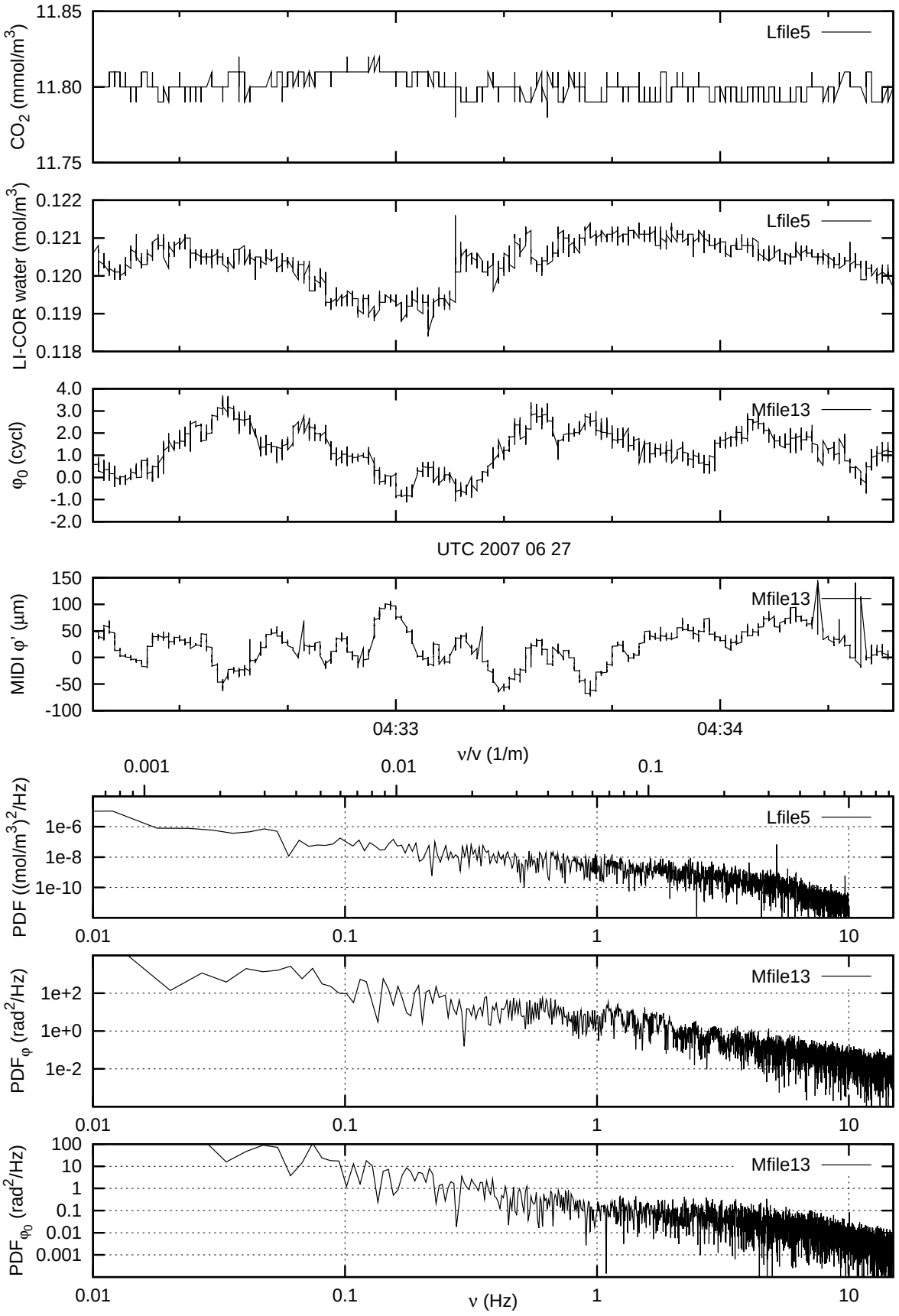

Figure 17: Correlation of MIDI data file 13 with LI-COR densities.

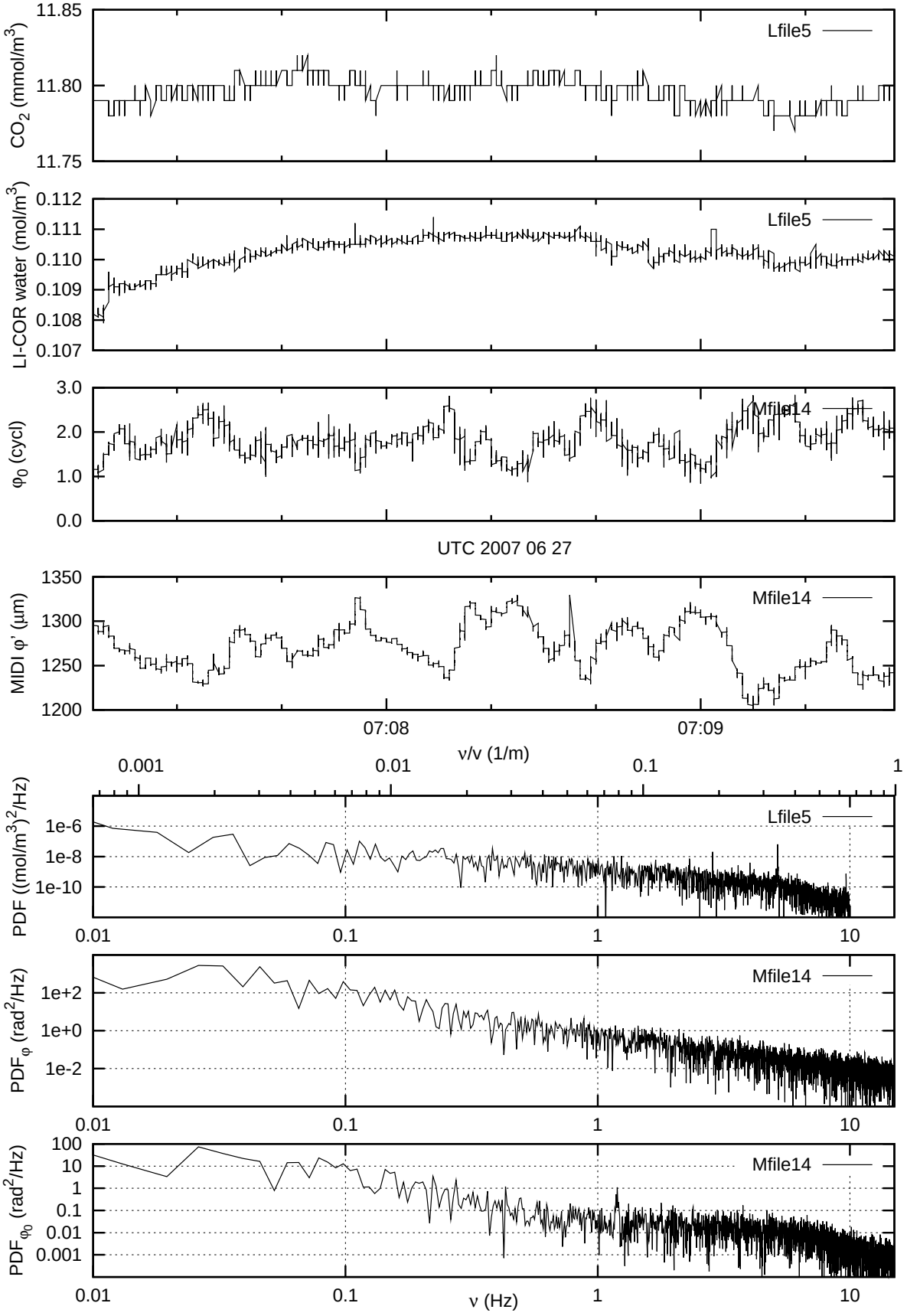

Figure 18: Correlation of MIDI data file 14 with LI-COR densities.

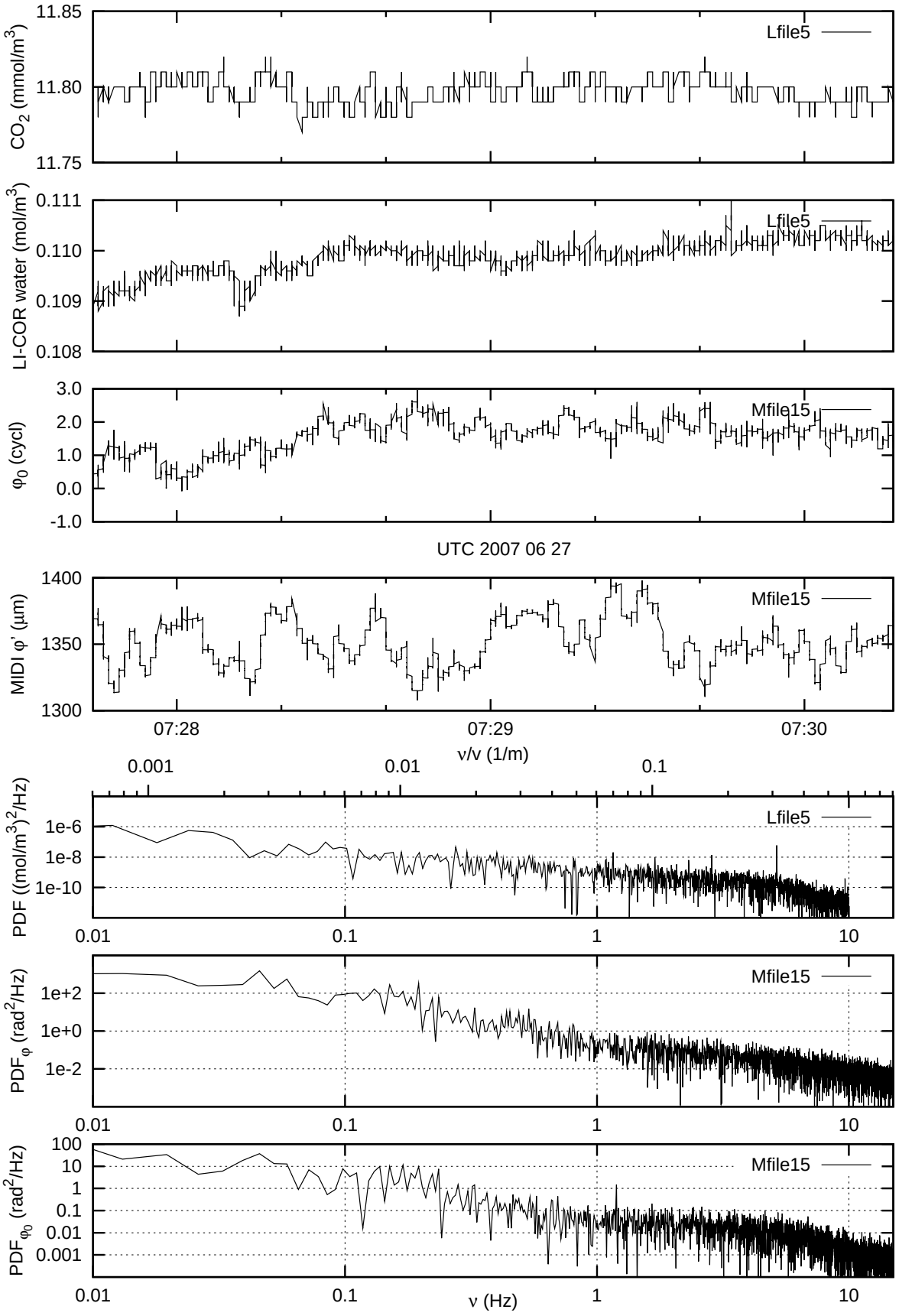

Figure 19: Correlation of MIDI data file 15 with LI-COR densities.

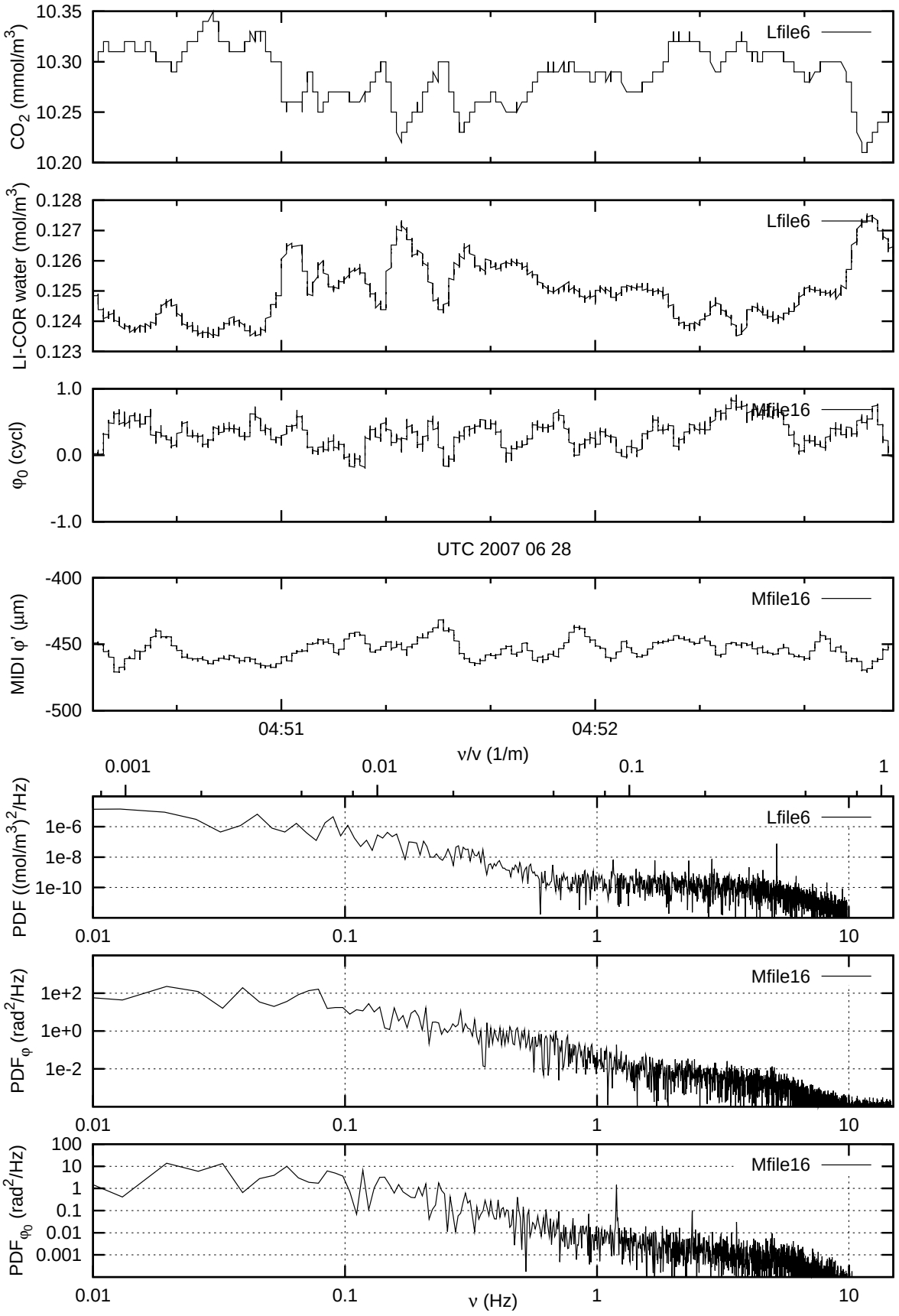

Figure 20: Correlation of MIDI data file 16 with LI-COR densities. The water densities in Figs. 20–33 are those reduced with Equation (1) of [16]. The wavenumber scale ν/v on the LI-COR densities does not make much sense in these figures because they have been measured in the tunnel and are scaled here with the weather pole wind velocity.

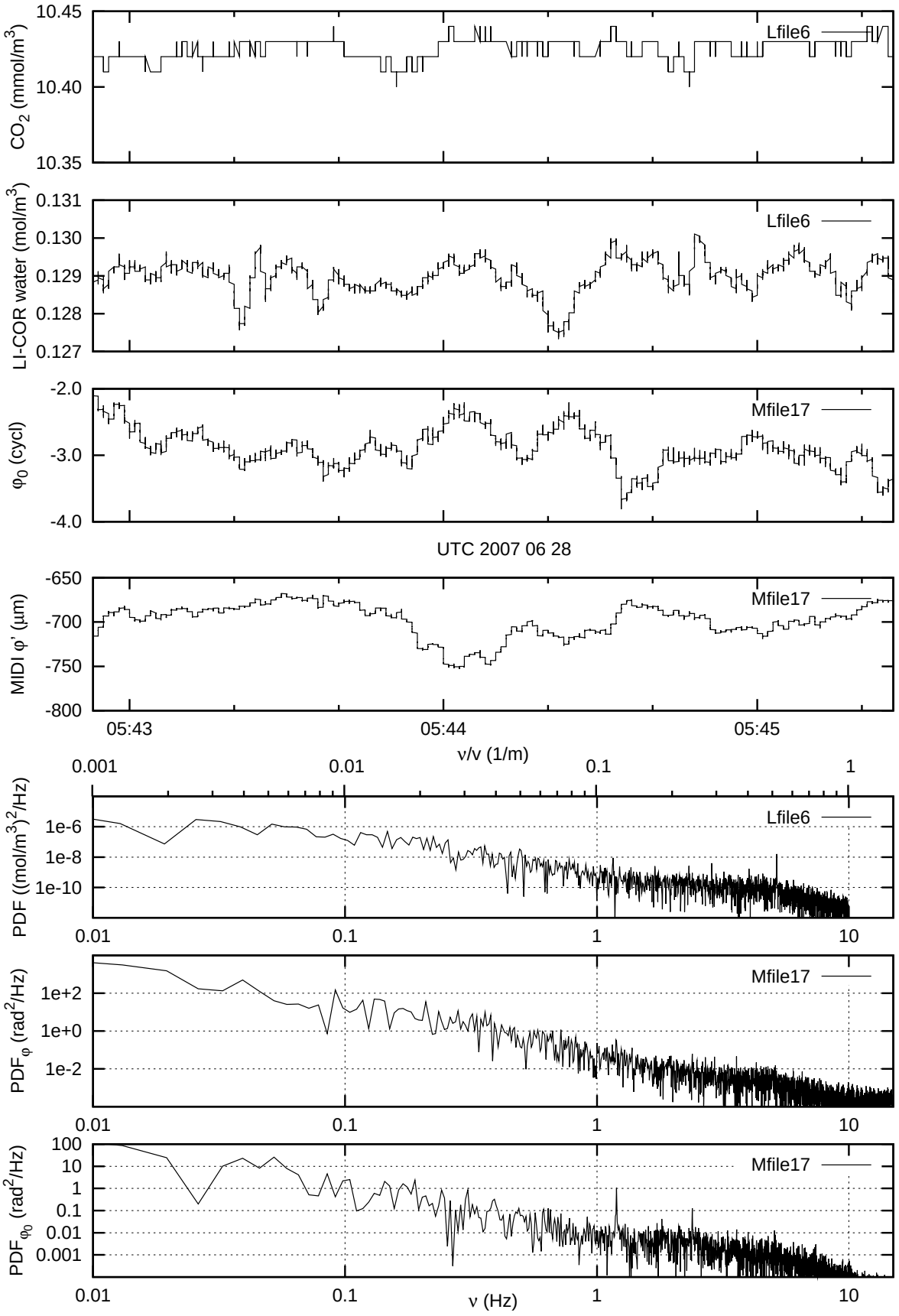

Figure 21: Correlation of MIDI data file 17 with LI-COR densities. Note that the wavenumber scale on the LI-COR densities does not make much sense here because they have been measured in the tunnel and are scaled here with the weather pole wind velocity.

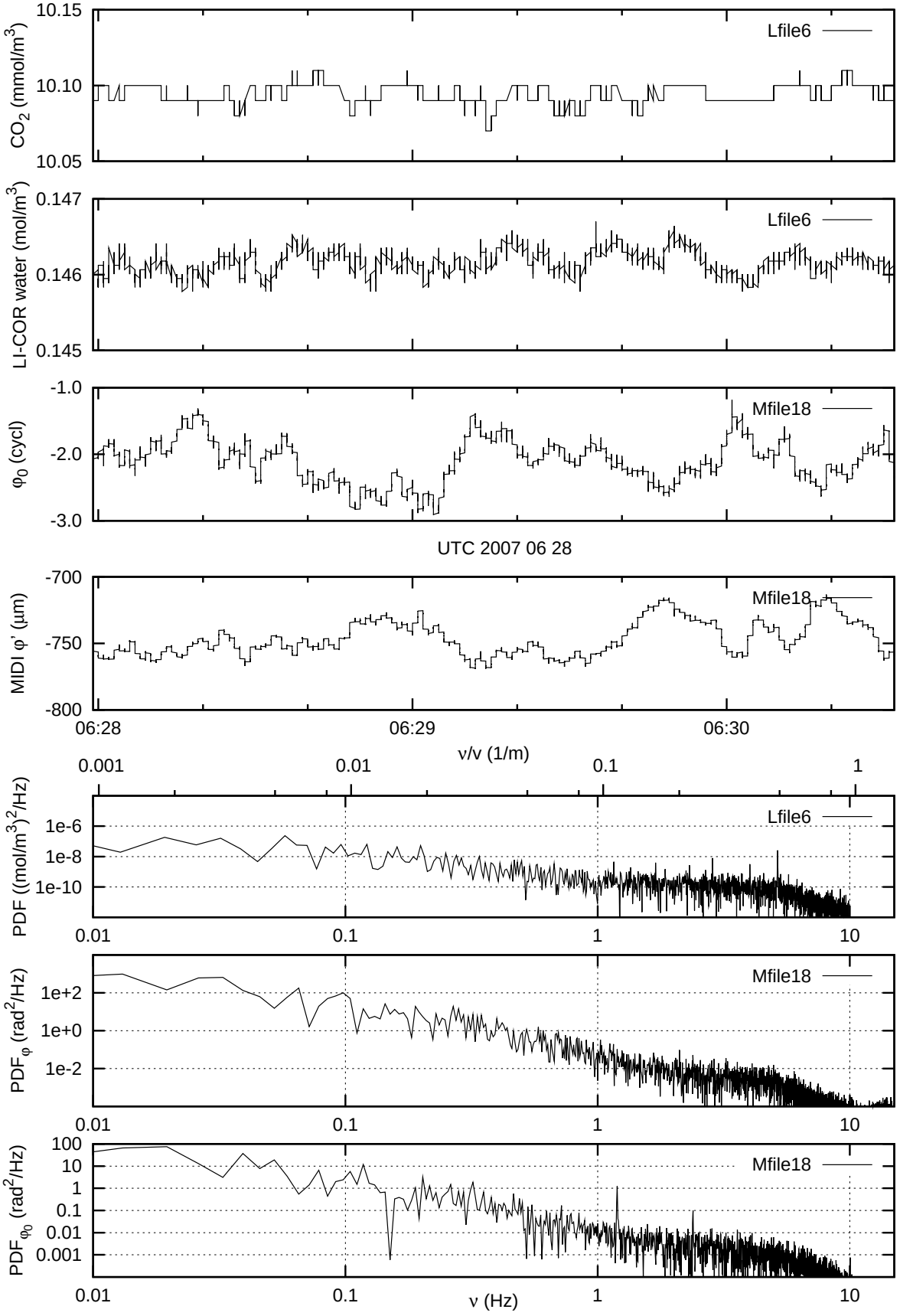

Figure 22: Correlation of MIDI data file 18 with LI-COR densities. Note that the wavenumber scale on the LI-COR densities does not make much sense here because they have been measured in the tunnel and are scaled here with the weather pole wind velocity.

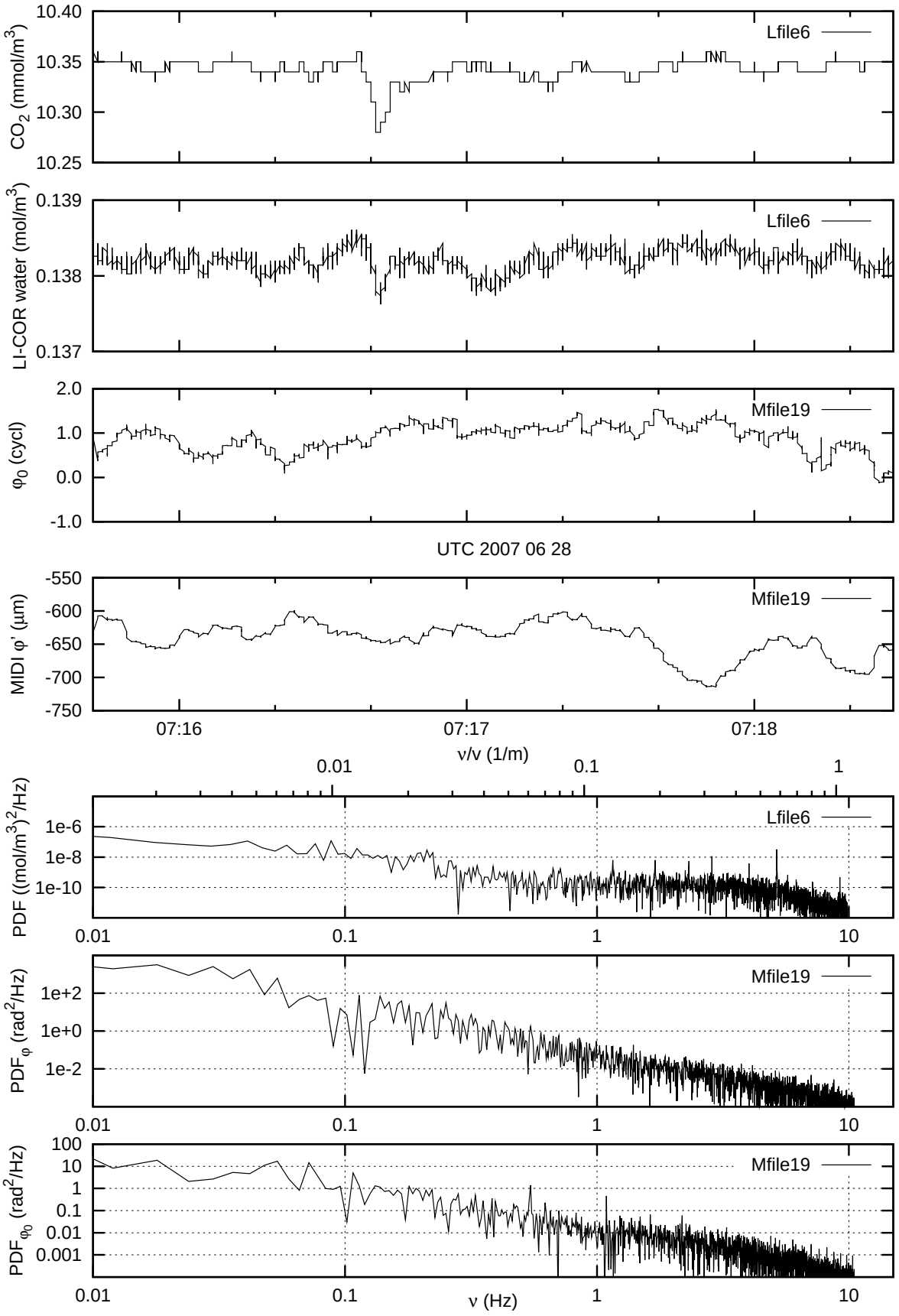

Figure 23: Correlation of MIDI data file 19 with LI-COR densities. Note that the wavenumber scale on the LI-COR densities does not make much sense here because they have been measured in the tunnel and are scaled here with the weather pole wind velocity.

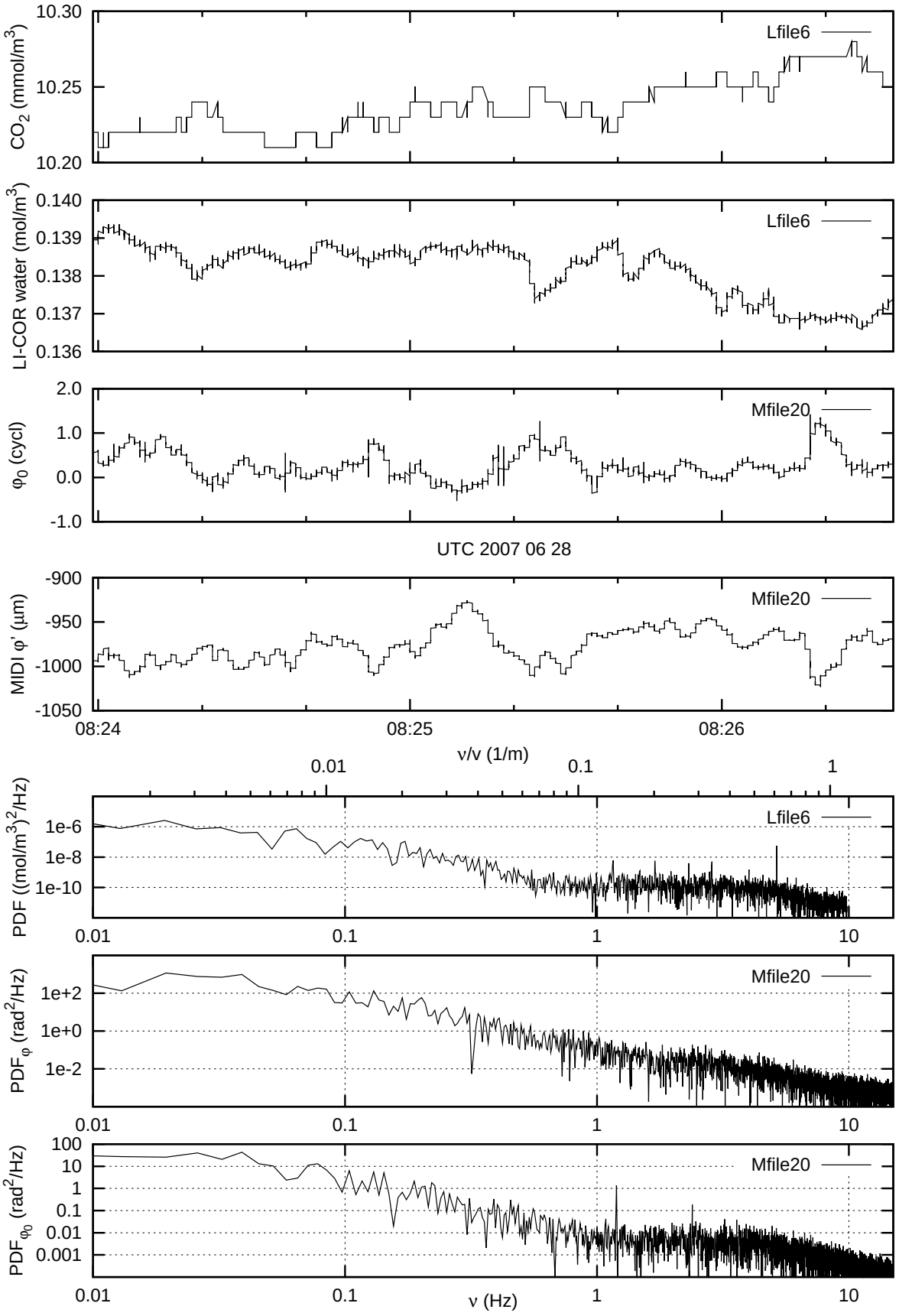

Figure 24: Correlation of MIDI data file 20 with LI-COR densities. Note that the wavenumber scale on the LI-COR densities does not make much sense here because they have been measured in the tunnel and are scaled here with the weather pole wind velocity.

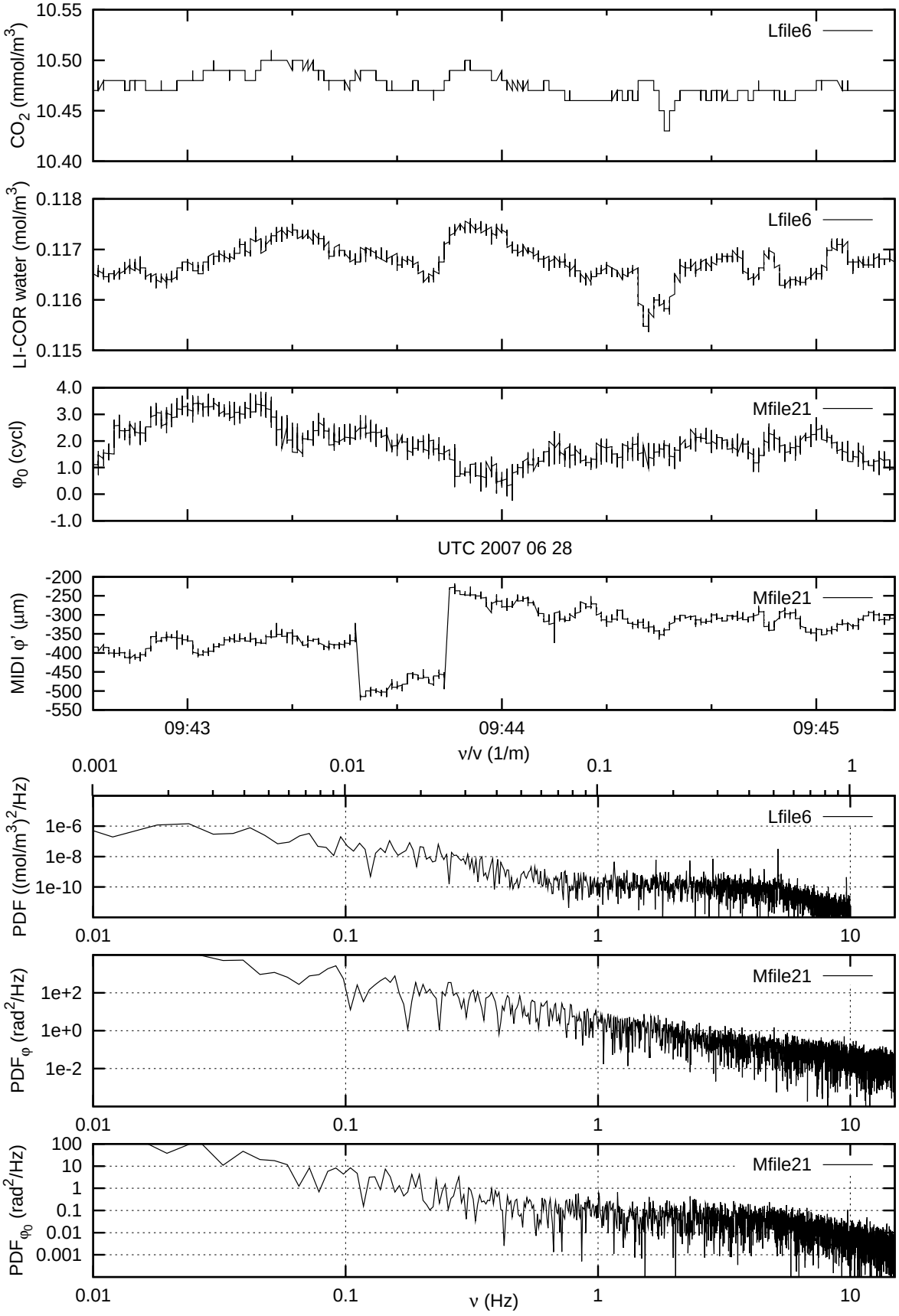

Figure 25: Correlation of MIDI data file 21 with LI-COR densities. Note that the wavenumber scale on the LI-COR densities does not make much sense here because they have been measured in the tunnel and are scaled here with the weather pole wind velocity. The origin of the sudden piston near 09:43:40 and of the even more obvious hub in Fig. 27 is unknown.

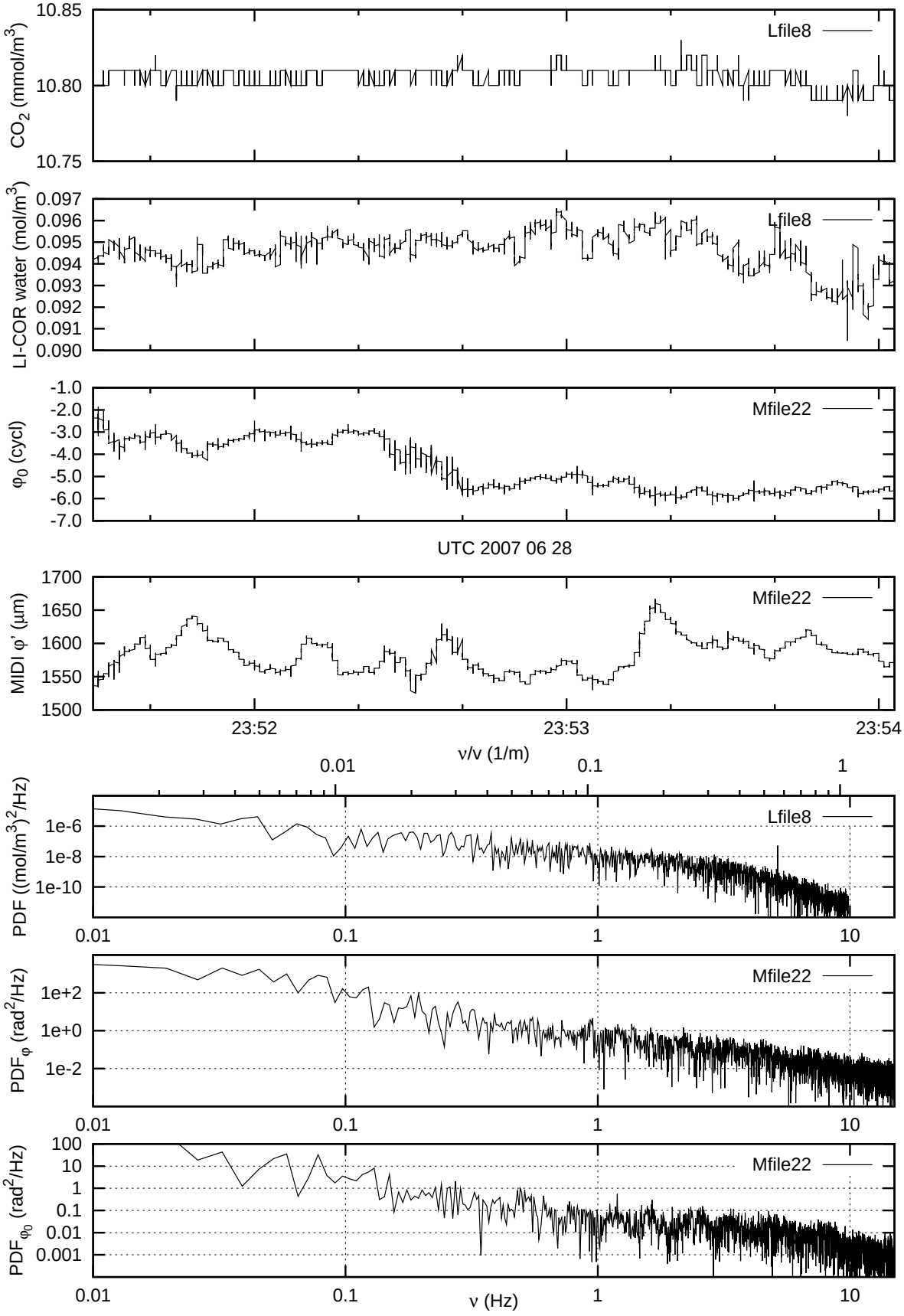

Figure 26: Correlation of MIDI data file 22 with LI-COR densities.

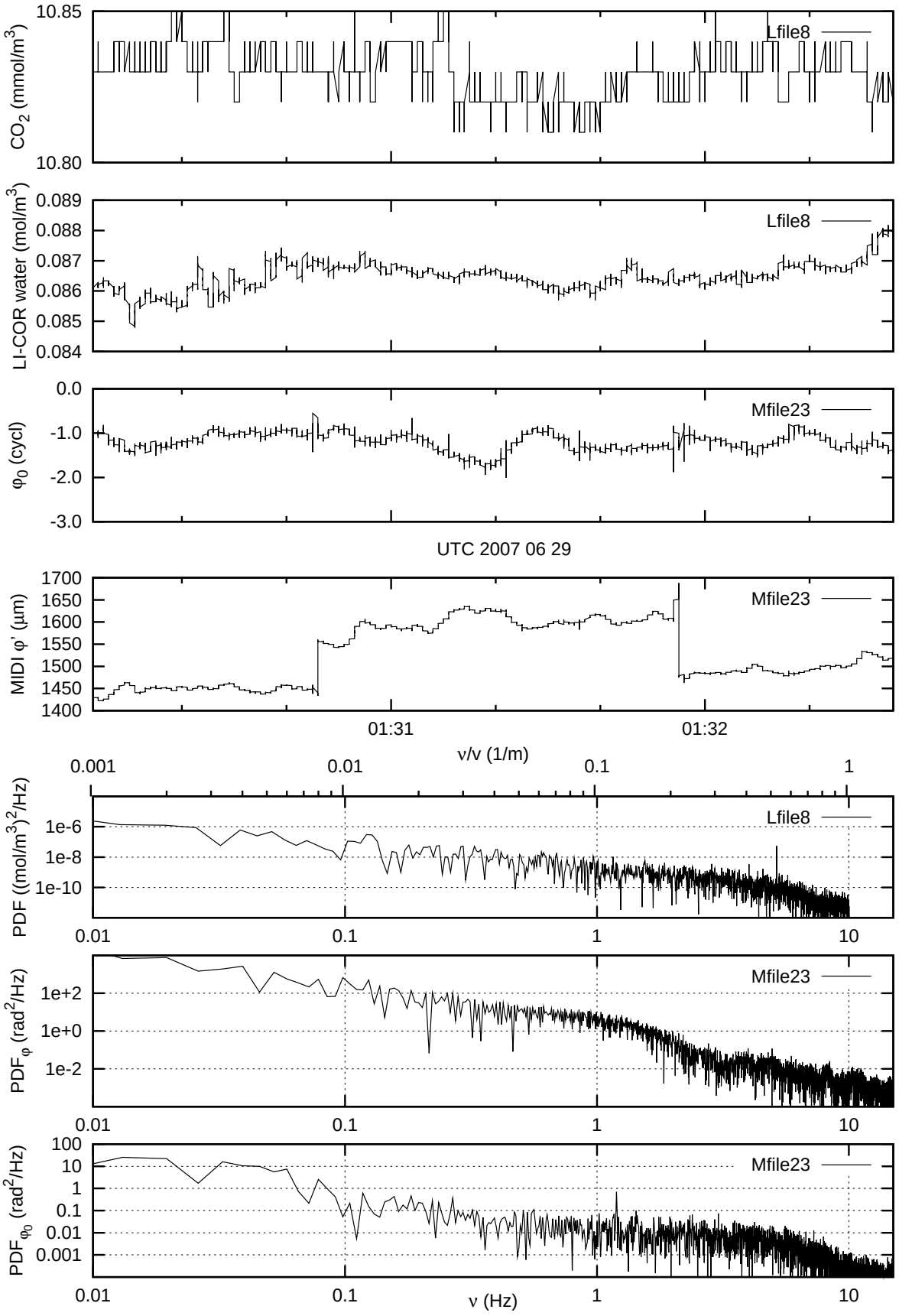

Figure 27: Correlation of MIDI data file 23 with LI-COR densities.

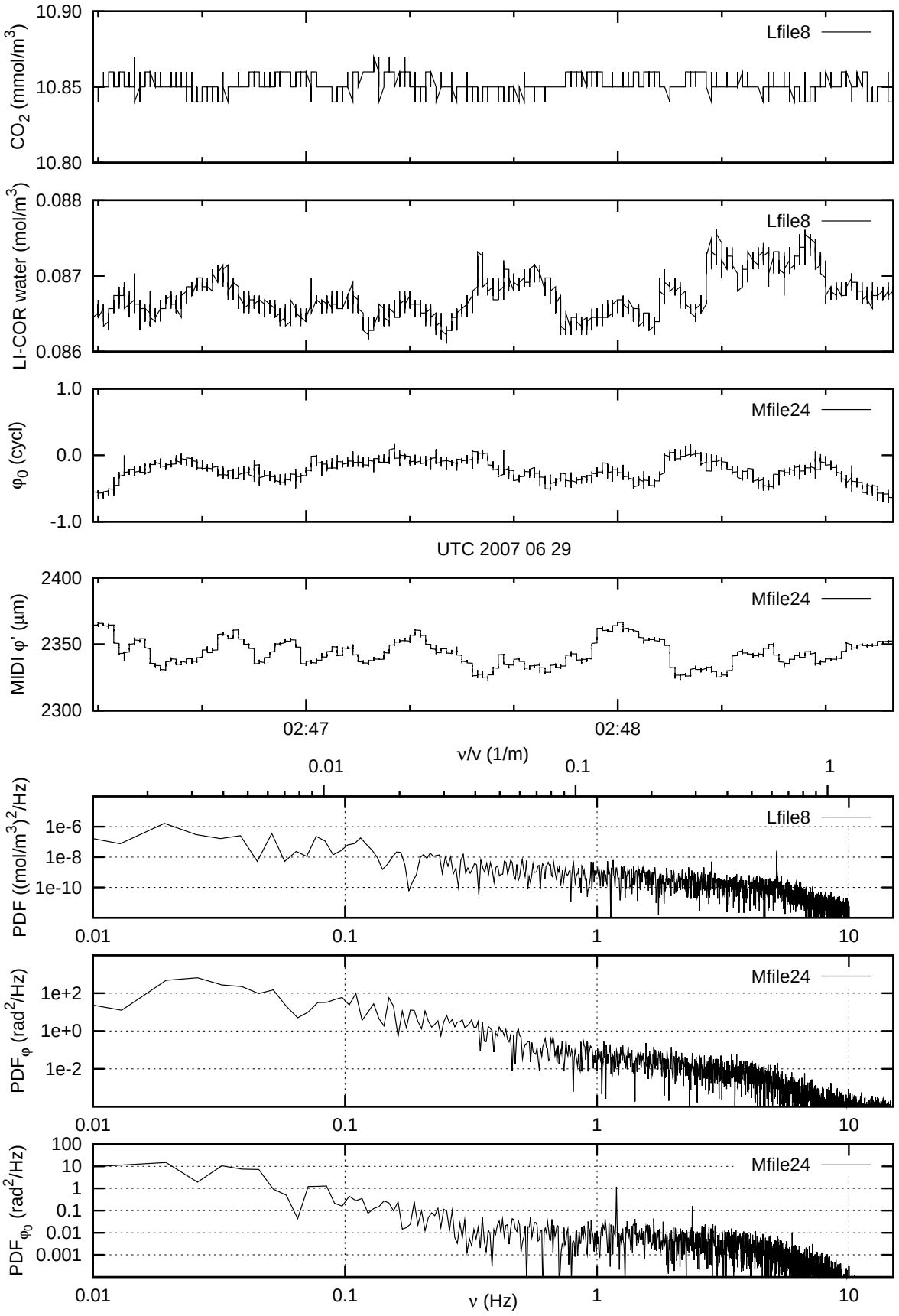

Figure 28: Correlation of MIDI data file 24 with LI-COR densities.

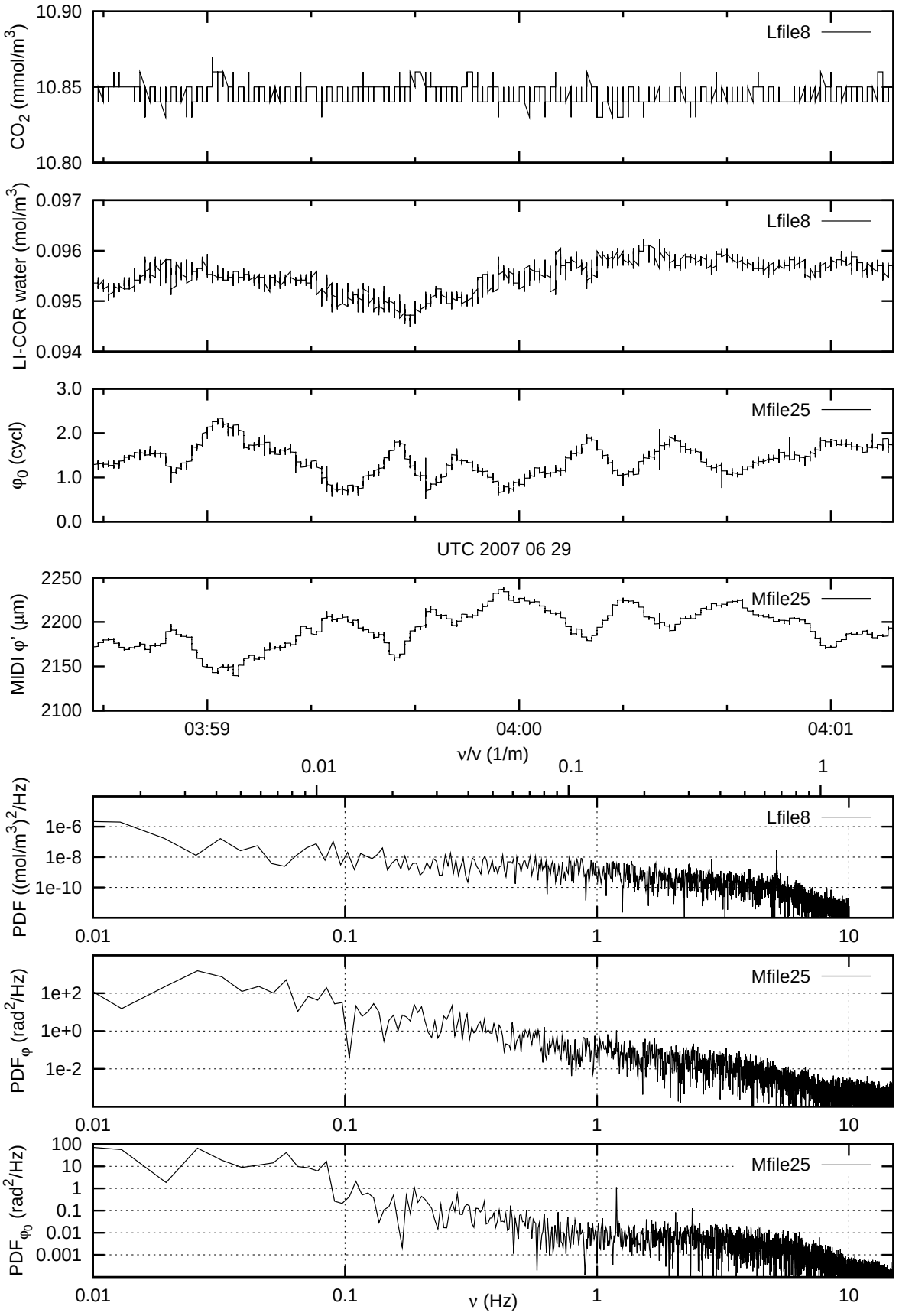

Figure 29: Correlation of MIDI data file 25 with LI-COR densities.

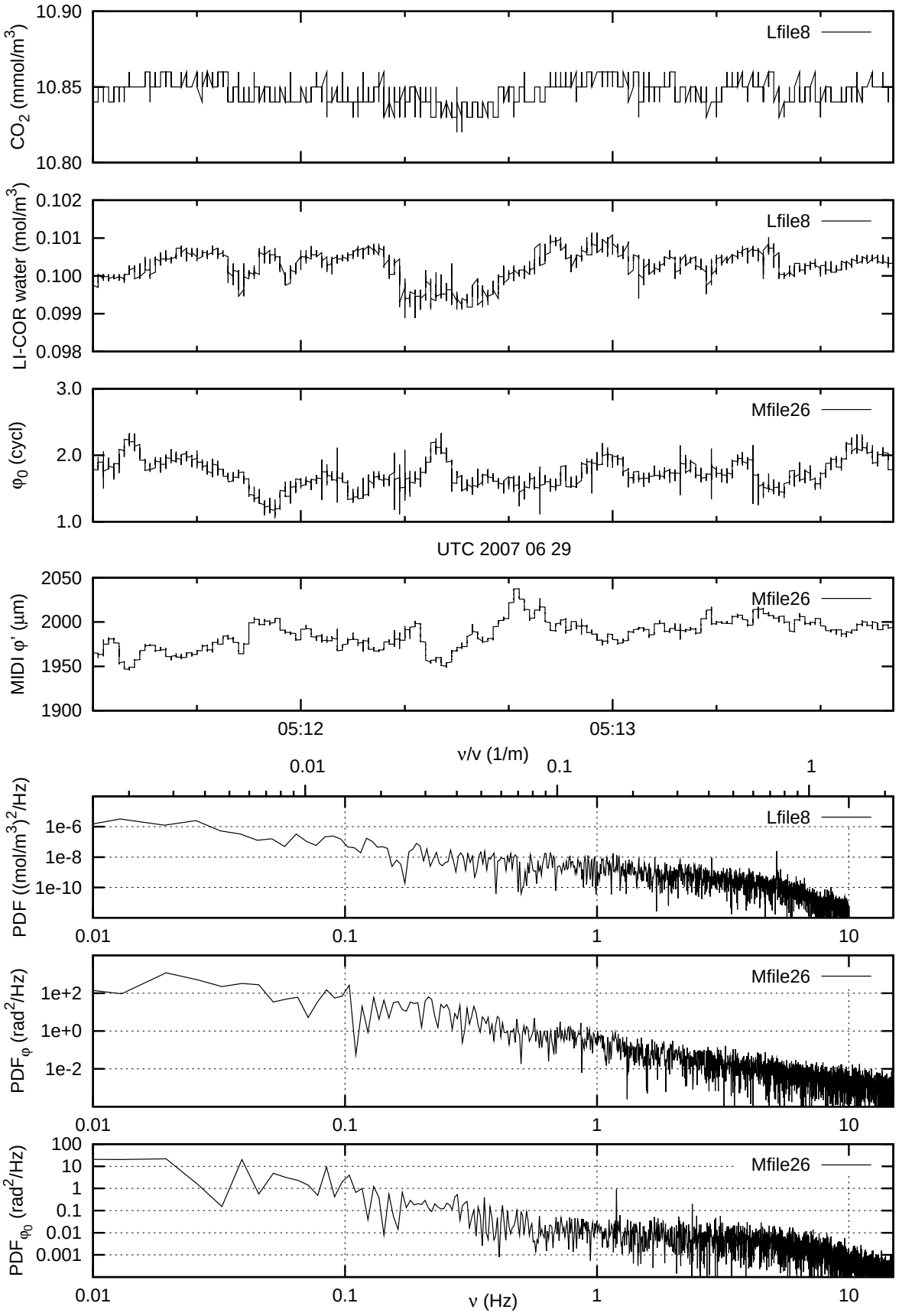

Figure 30: Correlation of MIDI data file 26 with LI-COR densities.

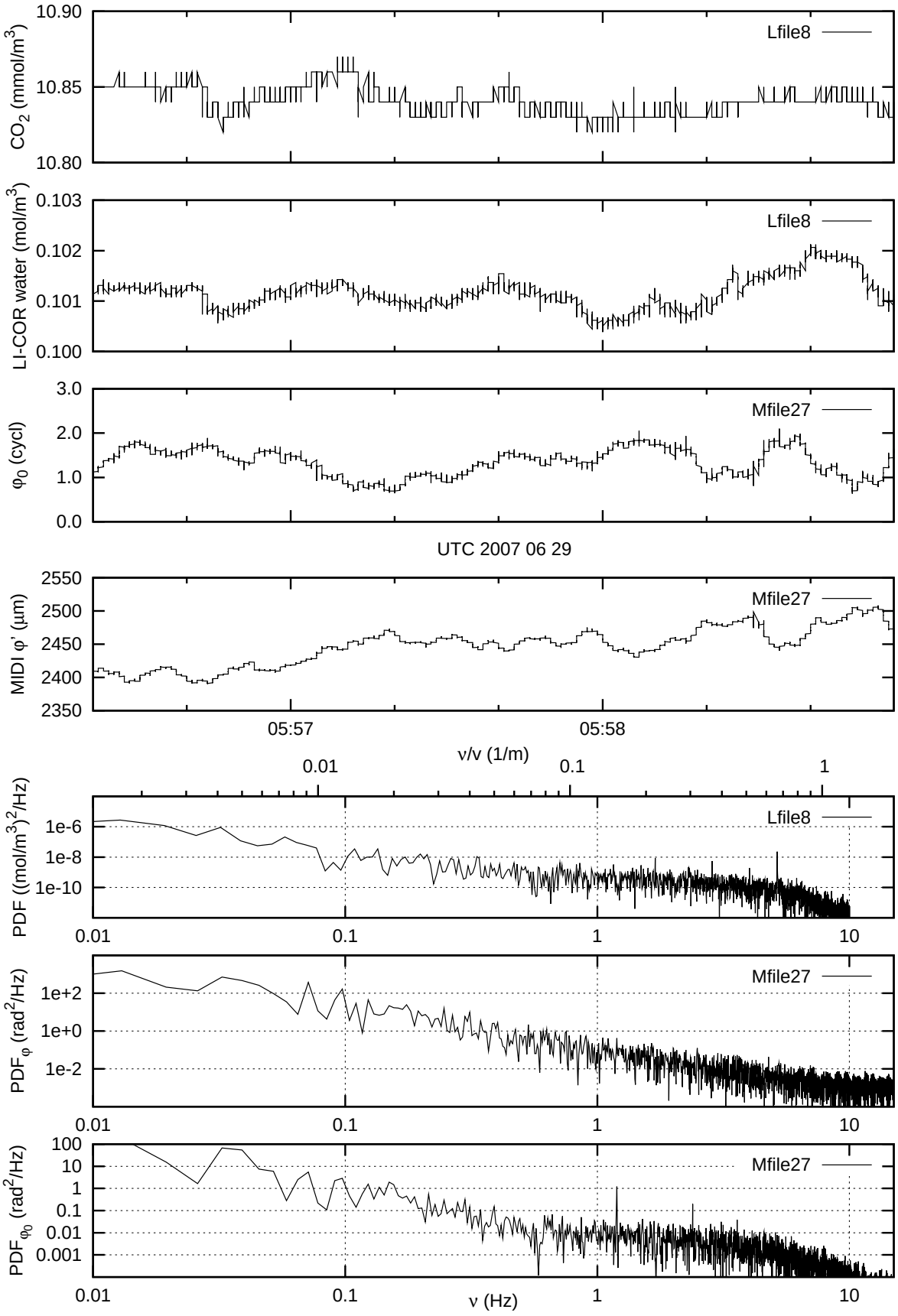

Figure 31: Correlation of MIDI data file 27 with LI-COR densities.

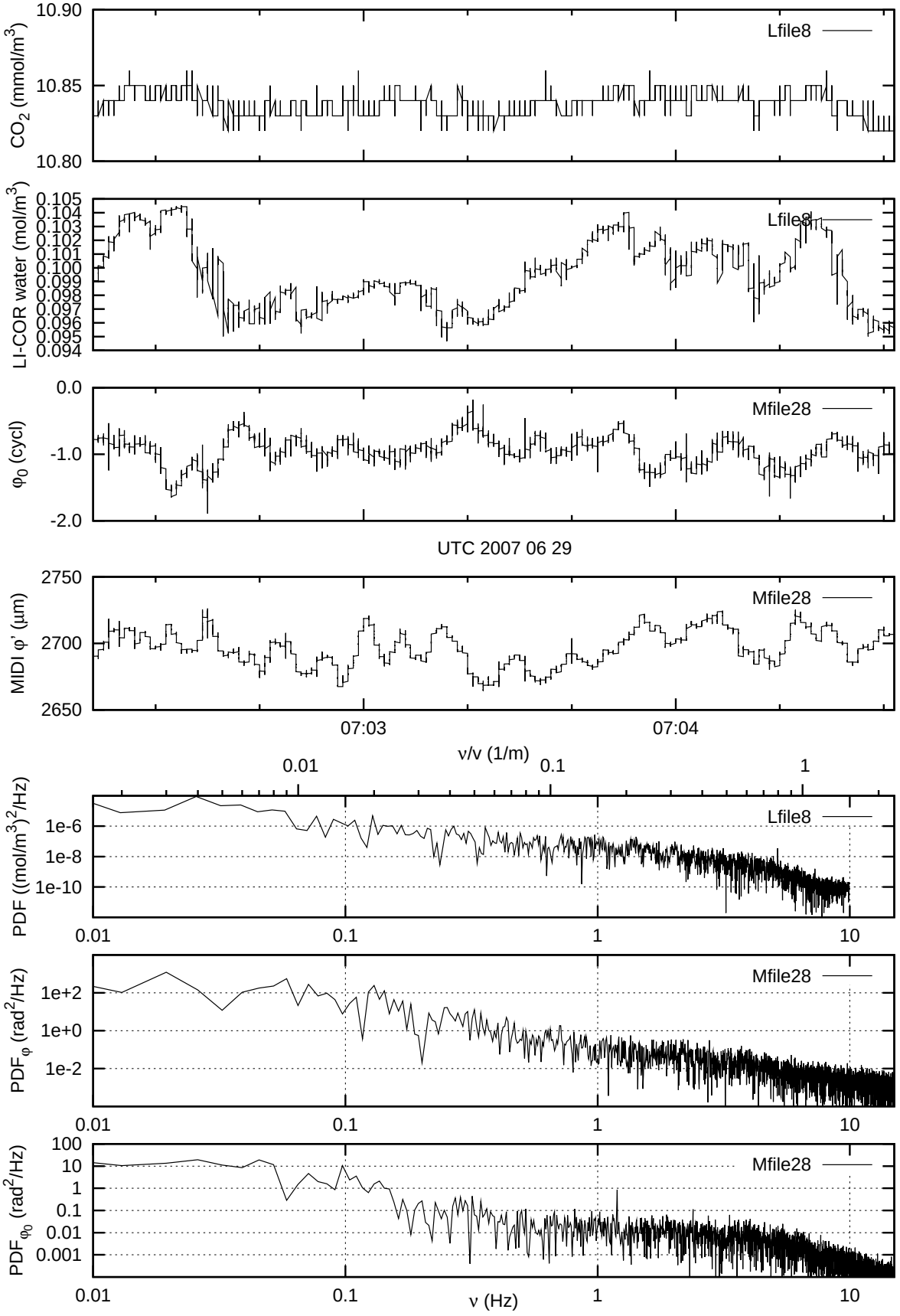

Figure 32: Correlation of MIDI data file 28 with LI-COR densities.

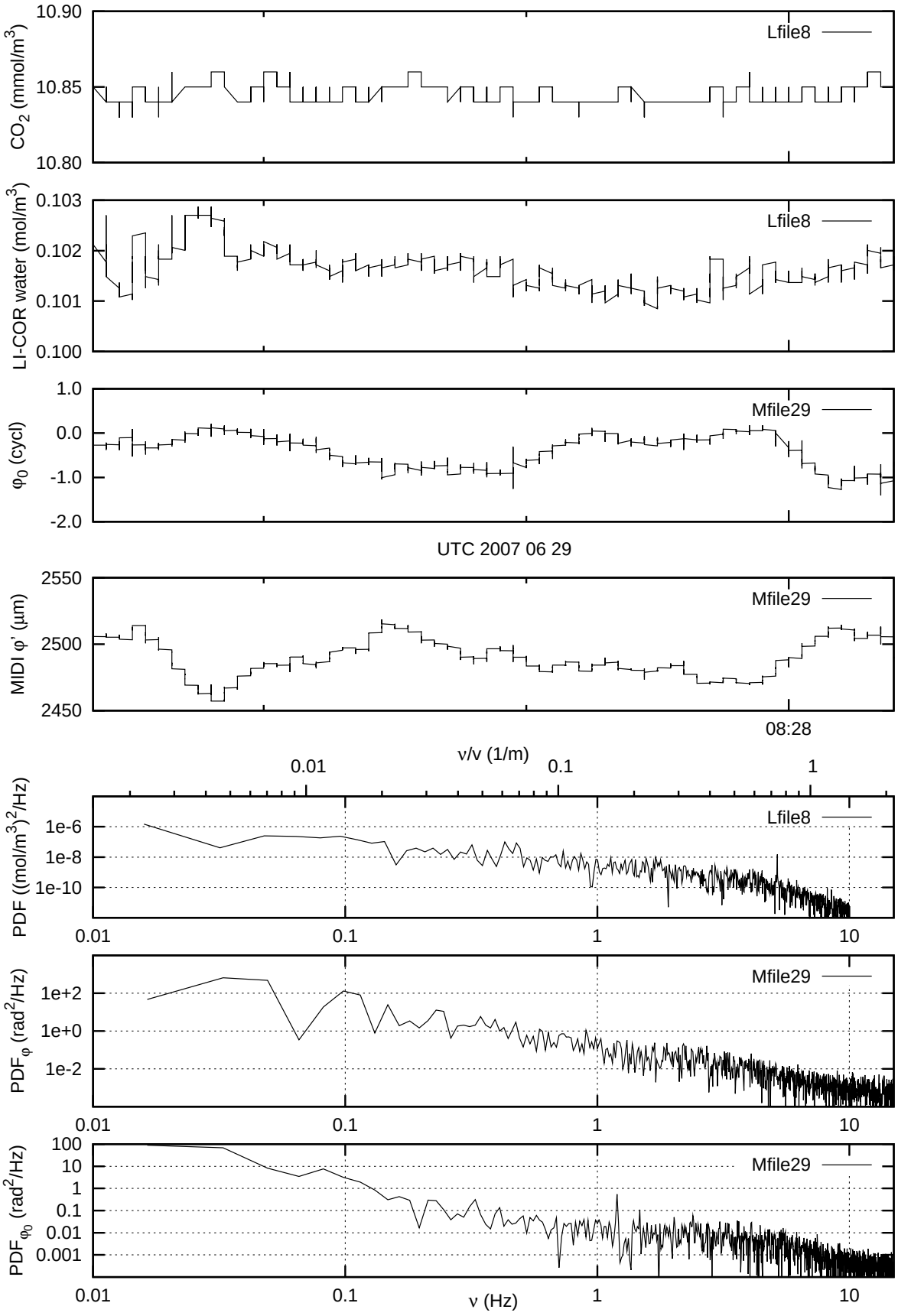

Figure 33: Correlation of MIDI data file 29 with LI-COR densities.

Figures 34–36 show the structure function of φ_0 or φ' for Mfile25–Mfile28 after flagging of weak points.

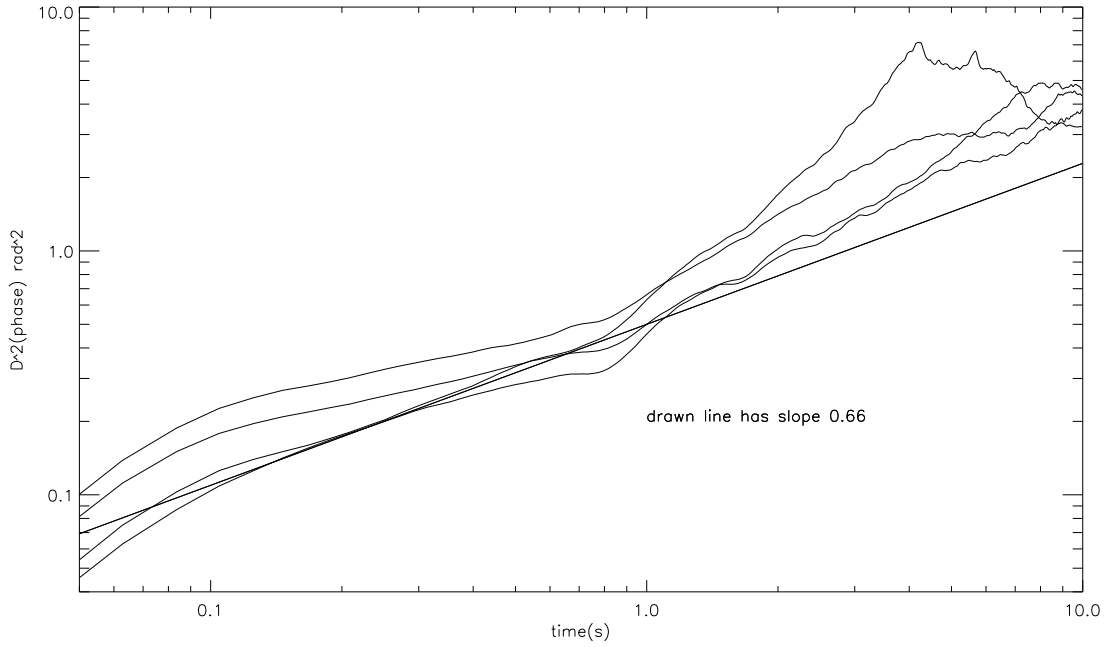

Figure 34: $\mathcal{D}_{\varphi_0}$ in units of rad^2.

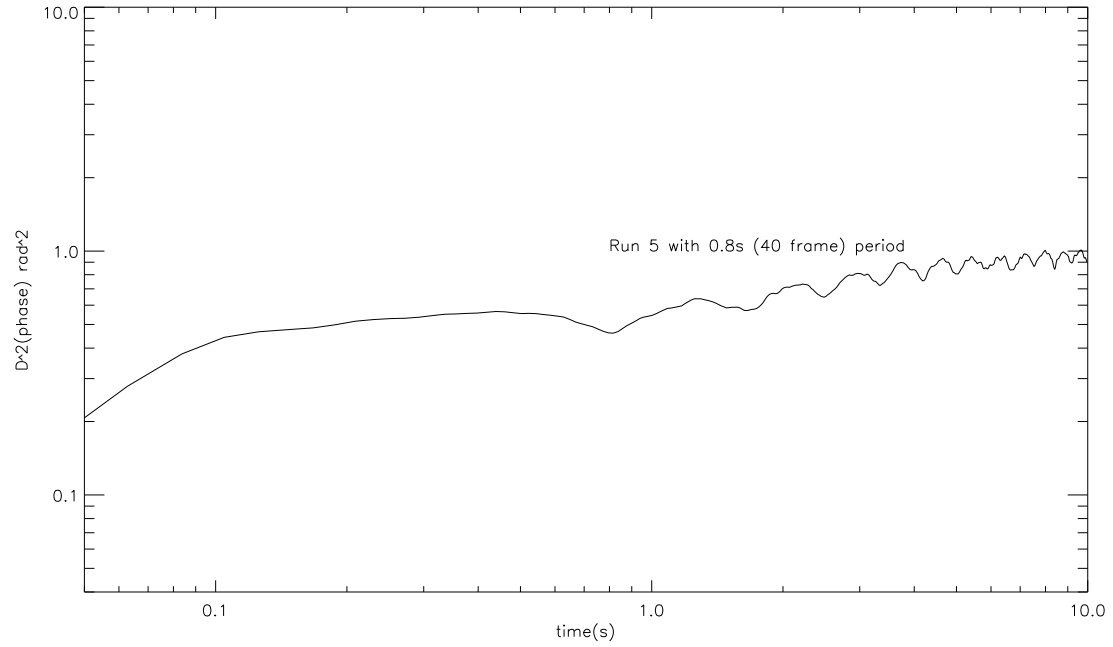

Figure 35: $\mathcal{D}_{\varphi_0}$ in units of rad^2. The detector cycle time has been the same for all 30 runs, and is not any different for run 5 shown here (see page 5). It is therefore not possible to evaluate from the data in this report whether the oscillations are an artifact of instrumental hardware, or some part of the data evaluation, for example Gibb's oscillations of some Fourier Transform.

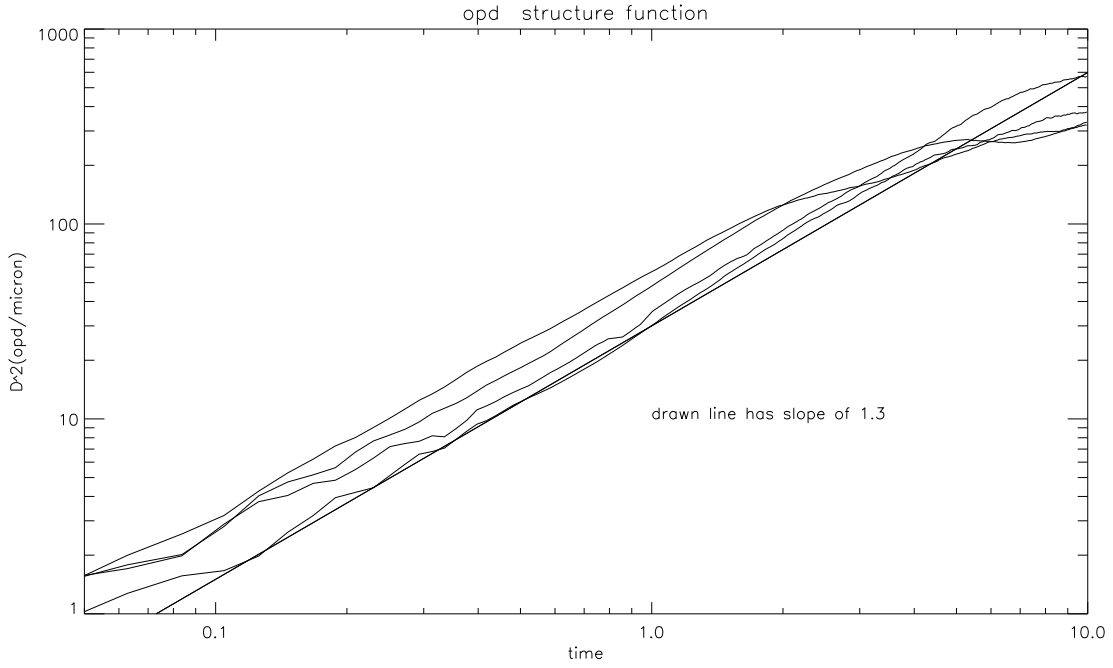

Figure 36: $\mathcal{D}_{\varphi'}$ in units of μm^2.

3 COMPARISON INTERFEROMETRY AND GAS ANALYZER

3.1 Refractive Index Model

An instrument like MIDI with some spectral dispersion may differentiate the chemical components in the optical paths if their refractive indices offer sufficient differences in the instrument's spectral band. We employ a linearized phase model of the dispersion [4]

$$k\hat{\chi}_{\mathrm{dry}}(\lambda) = a_{\mathrm{dry}} + b_{\mathrm{dry}}k; \quad k\hat{\chi}_{\mathrm{wet}}(\lambda) = a_{\mathrm{wet}} + b_{\mathrm{wet}}k. \tag{5}$$

We use the variables χ for the susceptibility, and $\hat{\chi}$ for its value ("intrinsic" polarizability) divided by the molecular number density. Differentiation of (5) with respect to k shows that the parameters b_{dry} and b_{wet} represent the augmented group refractive indices $n_g - 1$ [14, (7)] divided by the number densities.[2]

Numerical examples of the theory are shown in Fig. 37, Fig. 38 and 39. The coefficients in the fits quoted there are supposedly all proportional to the densities—that is, for our purposes here we may ignore the higher-order effects [15] because we do not need to achieve astrometric accuracy—and are divided through the partial pressures to generate the intrinsic, density-independent numbers.[3]

In the N-band, the intrinsic linear fitting coefficients are

$$b_{\mathrm{dry}} \approx \frac{2.0485\times10^{-4}}{31.771\mathrm{mol}\cdot\mathrm{m}^{-3}} \approx 6.45\times10^{-6}\frac{\mathrm{m}^3}{\mathrm{mol}}; \quad b_{\mathrm{wet}} \approx \frac{1.3224\times10^{-6}}{0.166\mathrm{mol}\cdot\mathrm{m}^{-3}} \approx 7.97\times10^{-6}\frac{\mathrm{m}^3}{\mathrm{mol}} \tag{6}$$

$$a_{\mathrm{dry}} \approx \frac{-3.608\times10^{-4}\mathrm{cm}^{-1}}{31.771\mathrm{mol}\cdot\mathrm{m}^{-3}} \approx -1.14\times10^{-5}\frac{\mathrm{m}^3}{\mathrm{mol}\cdot\mathrm{cm}}; \quad a_{\mathrm{wet}} \approx \frac{-4.21\times10^{-3}\mathrm{cm}^{-1}}{0.166\mathrm{mol}\cdot\mathrm{m}^{-3}} \approx -2.53\times10^{-2}\frac{\mathrm{m}^3}{\mathrm{mol}\cdot\mathrm{cm}} \tag{7}$$

This means the two b coefficients (inclinations of the fit) are almost the same for the two components, whereas the a coefficients (constant terms, axis intersections) differ by a factor of 2×10^3—on a per-molecule basis.

[2] This means (5) is the solution to the differential equation $n_g(k) \equiv n(k) + kdn/dk = b$, assigning a constant group refractive index $n_g = 1 + b$ to the dispersion.

[3] Doing this quickly is supported by the water vapor saturation curve, Fig. 37 in [13] and the GUI in http://www.strw.leidenuniv.nl/~mathar/progs/prWaterWeb.html.

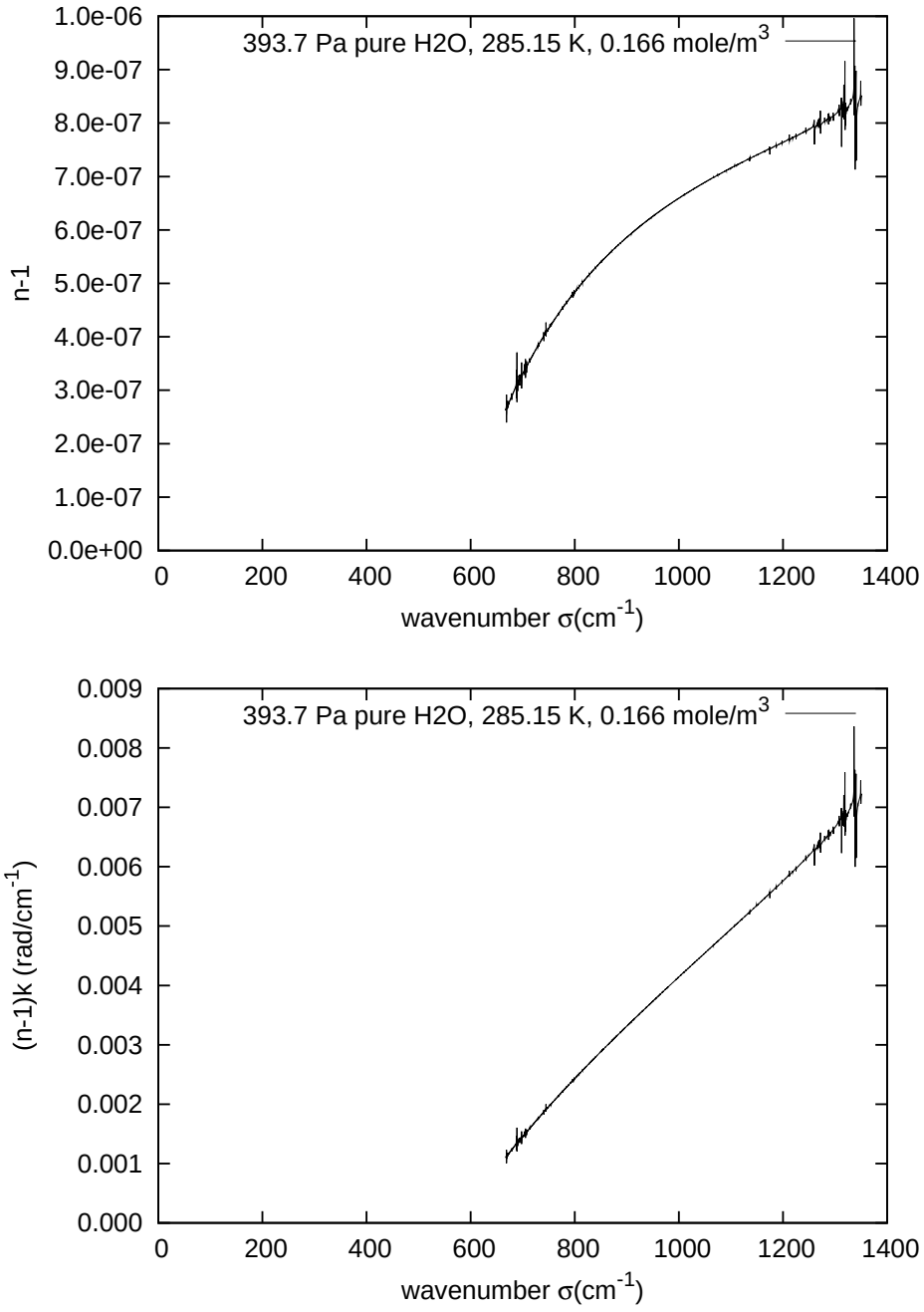

Figure 37: Upper plot: pure water vapor susceptibility $\chi_{\rm wet}$ at an average ambient partial pressure in the N band. Lower plot: product of this susceptibility $\chi_{\rm wet}$ and $k = 2\pi/\lambda = 2\pi\sigma$. A linear fit to the lower plot is $\chi k = -4.21 \times 10^{-3}{\rm cm}^{-1} + 1.3224 \times 10^{-6} k$, which means the group refractive index is $1 + 1.3224 \times 10^{-6}$ and "enhanced" by a factor of two relative to the $1 + 6.5 \times 10^{-7}$ of the phase refractive index of the upper plot.

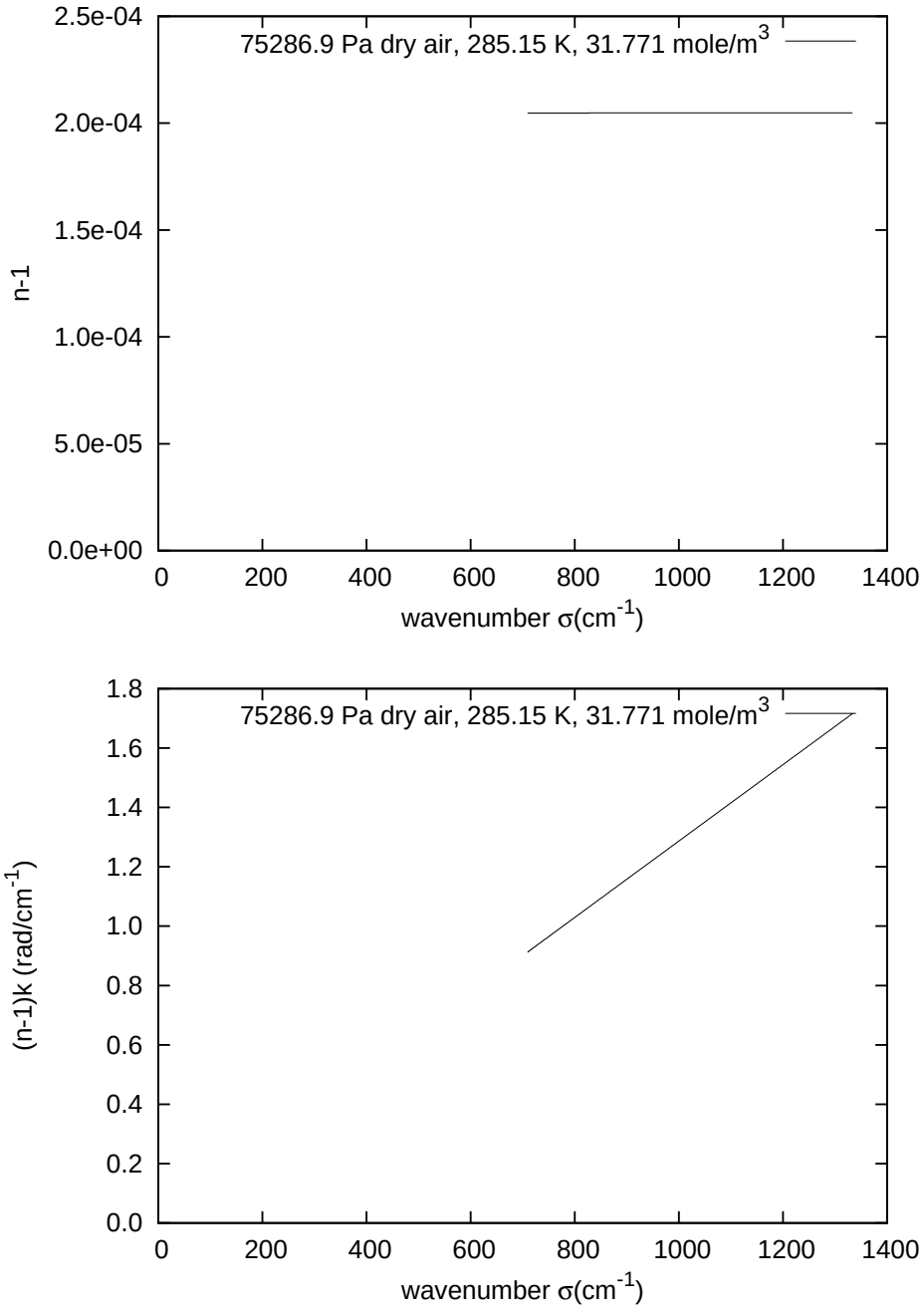

Figure 38: Upper plot: dry air susceptibility $\chi_{\rm dry}$ in the N band at a typical Paranal pressure. Lower plot: product of this susceptibility $\chi_{\rm dry}$ and $k = 2\pi/\lambda = 2\pi\sigma$. A linear fit to the lower plot is $\chi k = -3.608\times10^{-4}{\rm cm}^{-1} + 2.0485\times10^{-4}k$, which means the group refractive index is $1+2.0485\times10^{-4}$ and close to the phase refractive index of the upper plot.

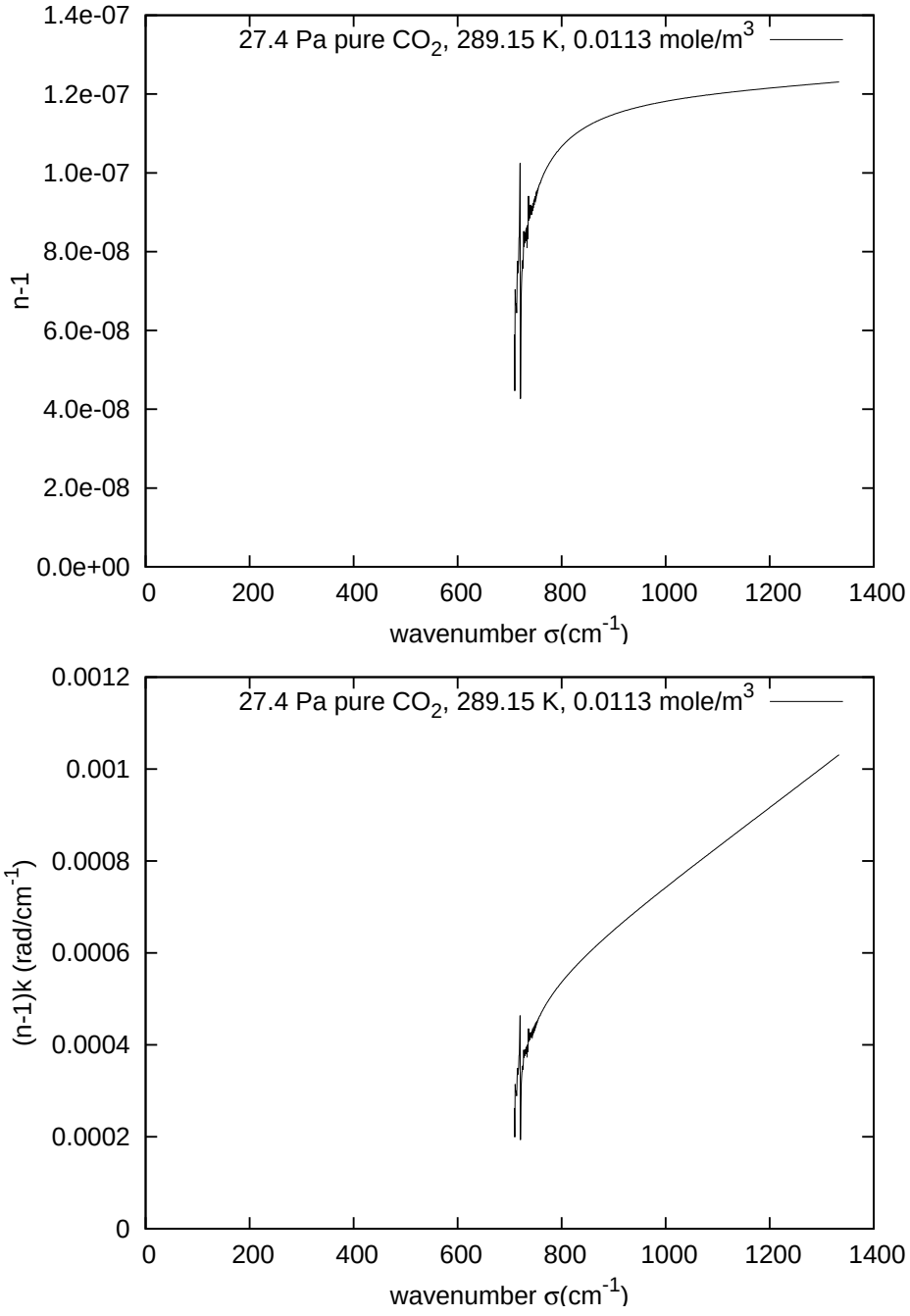

Figure 39: Upper plot: pure CO_2 susceptibility χ_c at a typical partial pressure in the N band. Lower plot: product of this susceptibility χ_c and $k = 2\pi/\lambda = 2\pi\sigma$. Each molecule of Carbon Dioxide has a polarizability which is approximately 1.53 times the polarizability of the average air molecule, in accordance with 10.5 μm measurements [12, Tabl 2].

3.2 Structure Functions and Fried Parameter

Density fluctuations C_ρ^2 are converted to line-of-sight-integrated refractive index structure functions and corresponding phase structure functions $\mathcal{D}_\varphi$ with

$$C_n^2 = C_\rho^2 \hat{\chi}^2; \tag{8}$$

$$\mathcal{D}_\varphi = k^2 \hat{\chi}^2 C^{(0)}(\alpha) C_\rho^2 K P^{1+\alpha} / \sin a \tag{9}$$

at scale height K, projected baseline length P, Kolmogorov power $\alpha = 2/3$, and star altitude a above the horizon. The sum of the fits (5) for the product $k\hat{\chi}$ at $k = 2\pi/(10\ \mu\text{m})$, and the definition of the Fried parameter r_0 [5, (6.3)] yield

$$\mathcal{D}_\varphi = (k\hat{\chi})^2 C^{(0)}(\alpha) C_\rho^2 K P^{1+\alpha} / \sin a = 6.884 (P/r_0)^{1+\alpha}. \tag{10}$$

The constants are $C^{(0)}(\alpha) = 2.914$ [17] and $k\hat{\chi} \approx (-2.53 + 7.97 \times 10^{-6} 2\pi/1 \times 10^{-5} - 1.14 \times 10^{-3} + 6.45 \times 10^{-6} 2\pi/1 \times 10^{-5})\ \text{m}^2/\text{mol} \approx 6.5\ \text{m}^2/\text{mol}$ as discussed in the other parts of the manuscript.

$$r_0 = \left(\frac{6.884 \sin a}{(k\hat{\chi})^2 C^{(0)}(\alpha) C_\rho^2 K} \right)^{3/5} \approx 0.176 \left(\frac{\sin a}{C_\rho^2 K} \right)^{3/5} \frac{\text{mol}^{6/5}}{\text{m}^{12/5}}. \tag{11}$$

The fit of the water structure functions $\mathcal{D}_{H2O}$ to a Kolmogorov 2/3 power law within the spatial distances from 1 to 10 m is illustrated in Figure 40.[4] On doubly-logarithmic axes, these are straight-line fits with fixed inclination. For `Mfile16`–`Mfile21` this computation is skipped because the LICOR measurements occurred in the VLTI tunnel during these observations.

[4] The only difference to Table 2 in [16] is that 4 hours of observation were summarized there, whereas the observations here cover approximately 2 minutes each.

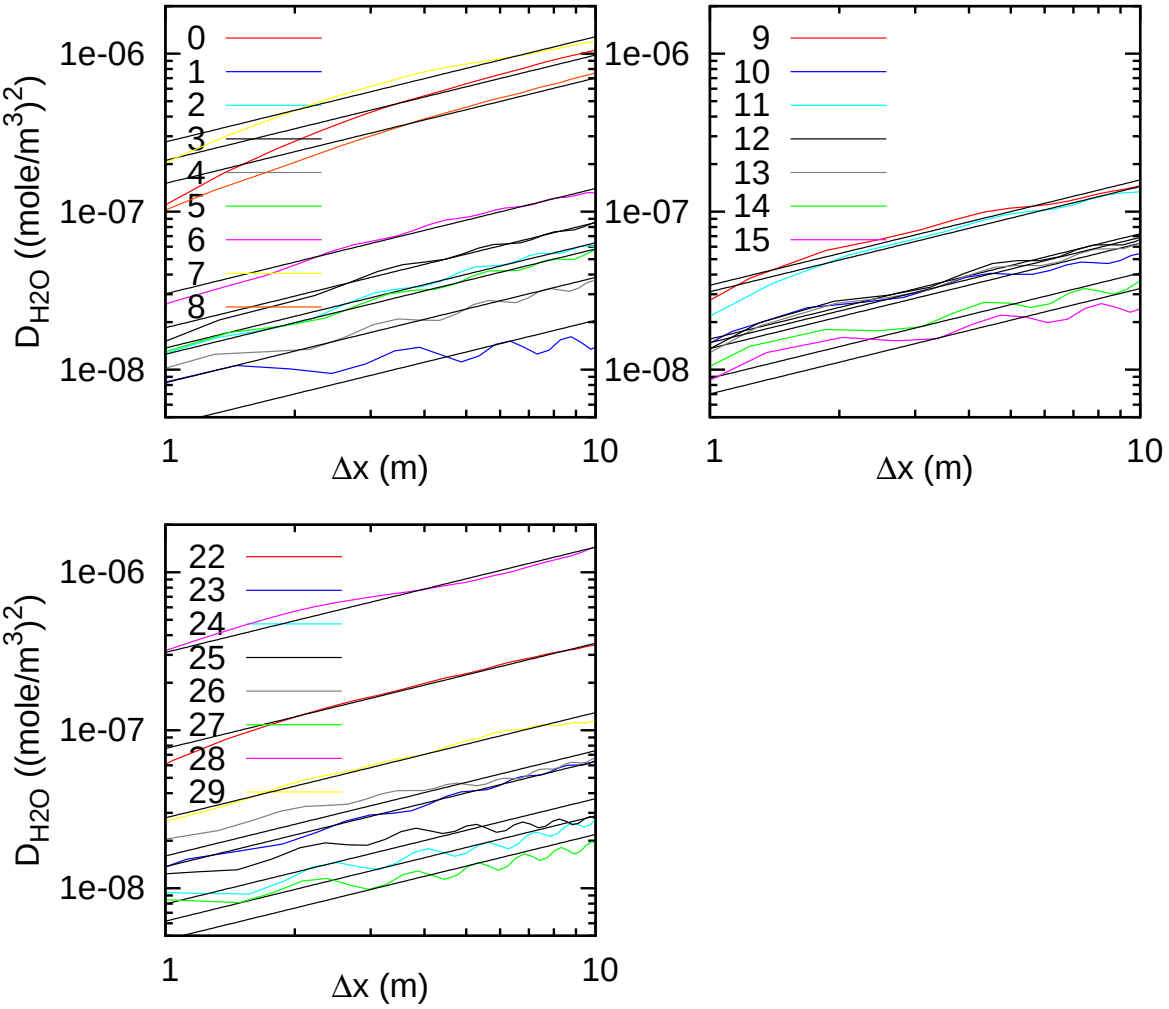

Figure 40: Kolmogorov fits to the LICOR water vapor structure functions. One panel is shown per night, curves enumerated with the file numbers as in Table 3. The colored curves are the structure functions; the black straight lines are the fits $\propto (\Delta x)^{2/3}$, each with $C^2_{\rm H2O}$ as the single free parameter.

The procedure is repeated for the carbon dioxide data in Figure 41. The structure function is flatter than the exponent 2/3 if $\mathcal{D}_{\mathrm{CO2}}$ is small, particularly in the fourth night. The main reason for this is uncovered in Figure 42: the digitization of the LI-COR data is quantized in units of 10^{-5} mol/m^3, which leads to a constant, distance-independent background noise level of 10^{-10} (mol/m^3)^2 in the structure function. At the 1 Hz time intervals at which the fit is attempted here, this is most of the value of the structure function itself, and not providing information on the actual air density fluctuations.

In detail, the connection between the density and refractive index structure functions is with (8) and scaling with $C^2_{\mathrm{dry}}/C^2_{\mathrm{CO2}} = 1/(3.8\times10^{-4})^2$,

$$C_n^2 = \left(\frac{2.04\times10^{-4}}{31.771}\,\frac{\mathrm{m}^3}{\mathrm{mol}}\right)^2 C^2_{\mathrm{dry}} \approx 4.1\times10^{-11}\,\frac{\mathrm{m}^6}{\mathrm{mol}^2}C^2_{\mathrm{dry}} \approx 2.9\times10^{-4}\,\frac{\mathrm{m}^6}{\mathrm{mol}^2}C^2_{\mathrm{CO2}}. \tag{12}$$

For Paranal, C_n^2 is in the range $5\times10^{-17}/\mathrm{m}^{2/3}$ –$5\times10^{-16}/\mathrm{m}^{2/3}$ [3], which means the expected range of C^2_{CO2} is from $2\times10^{-13}/\mathrm{m}^{2/3}$ to $2\times10^{-12}/\mathrm{m}^{2/3}$, not $1\times10^{-11}/\mathrm{m}^{2/3}$. If we reverse-engineer the C^2_{dry} from the `RO_MEAN` data of the primary FITS headers at 500 nm with (11) for all 30 MIDI files,

$$C^2_{\mathrm{dry}} = \frac{6.884}{r_0^{5/3}}\,\frac{\sin a}{K}\,\frac{1}{k^2\hat{\chi}^2 C^{(0)}(\alpha)}, \tag{13}$$

a maximum of $4.75\times10^{-6}/\mathrm{m}^{2/3}$ is found at `MFILE22`. Multiplied by $(3.8\times10^{-4})^2$ to extrapolate to the 380 ppm level of CO_2, C^2_{CO2} is actually not supposed to be larger than $7\times10^{-13}/\mathrm{m}^{2/3}$, in obvious discrepancy with the naïve fits to the noise level of the LI-COR CO_2 data in Table 3.

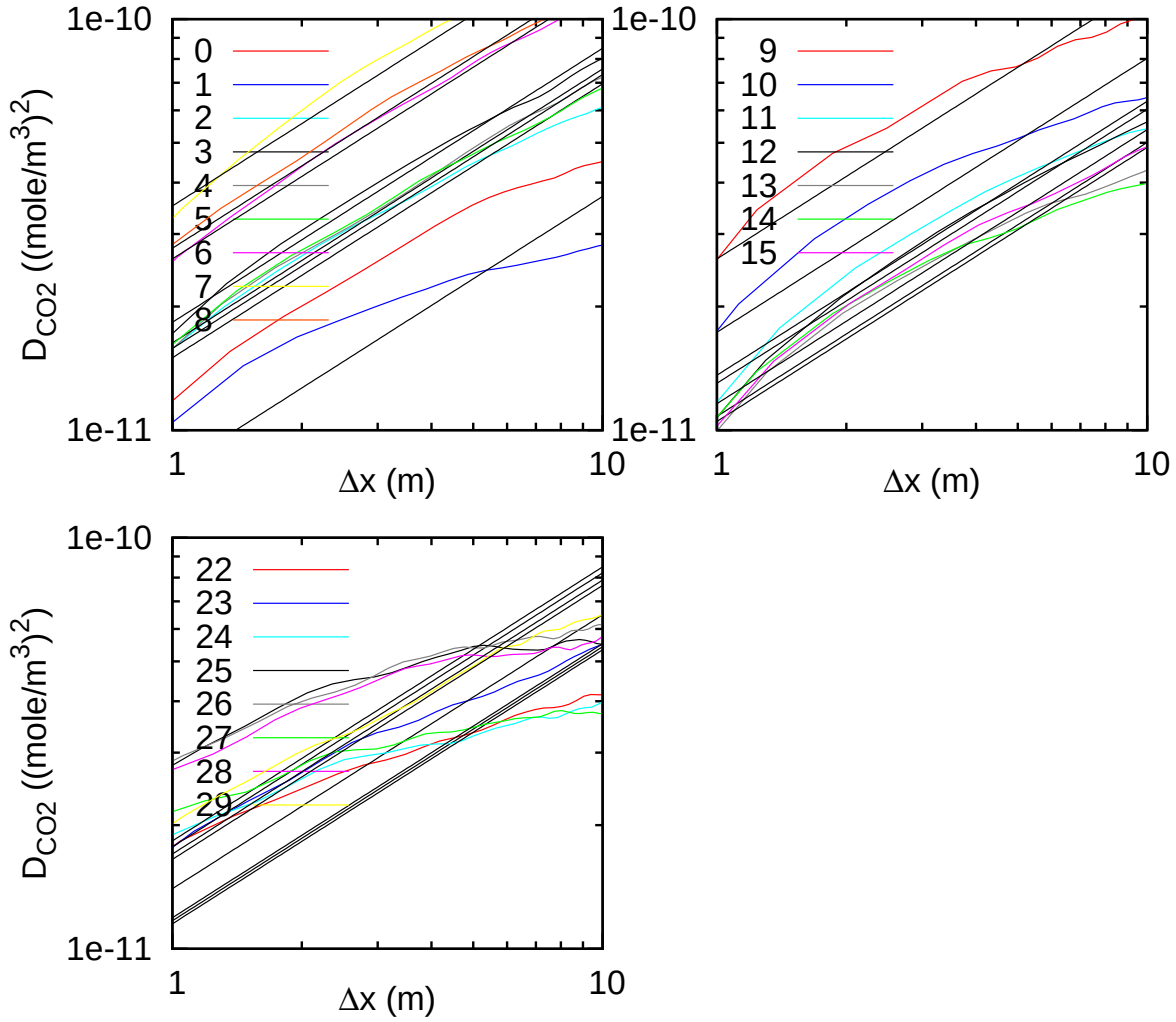

Figure 41: Kolmogorov fits to the LICOR CO_2 vapor structure functions. One panel is shown per night, curves enumerated with the file numbers as in Table 3. The colored curves are the structure functions; the black straight lines are the fits $\propto (\Delta x)^{2/3}$, each with C^2_{CO2} as the single free parameter.

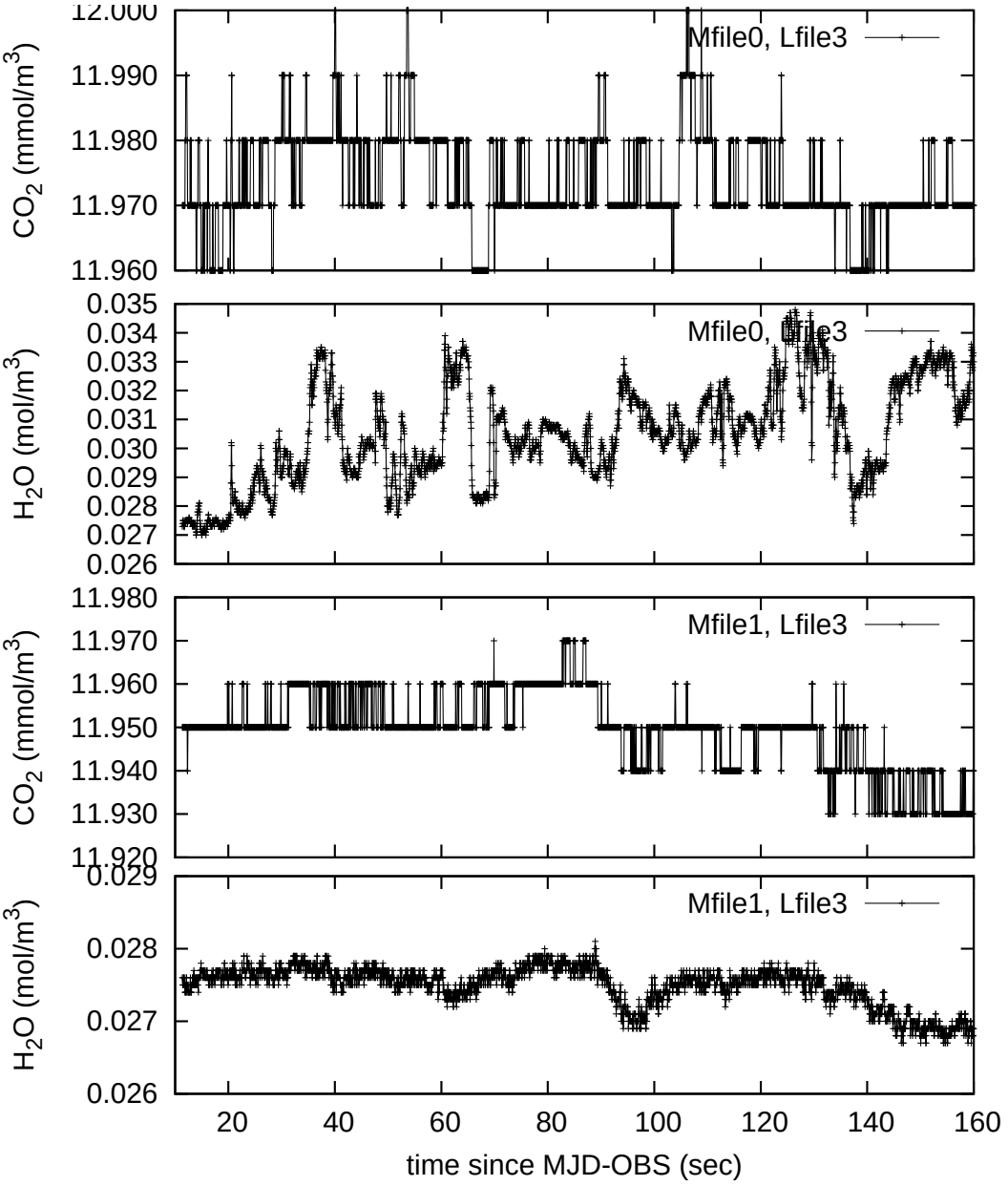

Figure 42: These replots of the LI-COR molar densities of Figures 4 and 5 demonstrate that a digitization (quantisation) noise of 1×10^{-5} mol/m^3 is inherent (and dominant at short time scales) to the CO_2 measurements, and a noise of 5×10^{-5} mol/m^3 is inherent (and relatively less important) to the water measurements.

The fitted C_ρ^2 for water and carbon dioxide are gathered in Table 3 in the columns C^2_{H2O} and C^2_{CO2}—although the latter is not of any value as discussed above.

- `RO_MEAN` is the mean of the two `COU AO1` and `COU AO2` values of the primary FITS headers scaled from 500 nm to 10 μm proportional to $\lambda^{6/5}$ [18, Table I]. Although the `RO_MEAN` of the VLTI FITS headers are essentially undocumented in DICB's `ESO-VLT-DIC.COU`, we assume that this is the value for pointing to the zenith.

- The column α_v is the platform wind direction (primary header keyword `WINDDIR`) relative to the baseline direction (ie, 111 and 40 degrees from North for the two UT baselines) reduced to the interval from 0 to 90 degrees. As expected from the dominant seasonal wind direction on Paranal, the U23 baseline of the second and fourth night is better aligned with the wind direction than the U34 baseline of the first and third night.

- The column $v_\perp$ is the component of the wind vector (derived from `WINDDIR` and the `WINDSP` of Table 1 assumed horizontal) perpendicular to the pointing direction, i.e., parallel to the projected baseline. (The latter is obtained from `ALT` and `AZ` of Table 2. If pointing were to the zenith, $v_\perp$ would be $|v\cos A_v|$.)

- The column A_v is the pointing direction relative to the wind direction—difference between `WINDDIR` and `AZ` if converted to a common coordinate system—reduced to the interval [0°,180°]. 0 refers to pointing into the wind, which is the worst case of shaking the main telescope structures [8].

- The column ρ_{wet} is the mean water number density reading of the LI-COR instrument over the exposure time, corrected as documented [16], outdoors or in the tunnel.

- The column C^2_{dry} is the dry air fluctuation derived from the `RO_MEAN` keyword of the primary FITS header via (13), the scale height guessed at $K = 9600$ m.

Mfile$n$	RO_MEAN (m)	α_v (deg)	$v_\perp$ (m/s)	C^2_{H2O} ($\mathrm{mol}^2/\mathrm{m}^{20/3}$)	C^2_{CO2} ($\mathrm{mol}^2/\mathrm{m}^{20/3}$)	A_v (deg)	ρ_{wet} ($\mathrm{mol}/\mathrm{m}^3$)	C^2_{dry} ($\mathrm{m}^{2/3}$)
0	4.37	15	11.57	2.13×10^{-7}	1.15×10^{-11}	110	0.030	8.76×10^{-7}
1	4.24	31	11.34	4.42×10^{-9}	7.98×10^{-12}	132	0.027	9.37×10^{-7}
2	3.35	55	9.23	1.38×10^{-8}	1.50×10^{-11}	152	0.029	1.17×10^{-6}
3	6.32	57	10.25	1.85×10^{-8}	1.83×10^{-11}	59	0.030	6.56×10^{-7}
4	5.75	59	10.37	8.26×10^{-9}	1.63×10^{-11}	64	0.030	7.58×10^{-7}
5	3.35	61	10.10	1.25×10^{-8}	1.58×10^{-11}	149	0.029	1.13×10^{-6}
6	3.44	75	6.39	3.09×10^{-8}	2.61×10^{-11}	142	0.031	1.72×10^{-6}
7	3.08	83	7.69	2.76×10^{-7}	3.51×10^{-11}	130	0.034	1.68×10^{-6}
8	3.15	87	8.05	1.51×10^{-7}	2.77×10^{-11}	65	0.036	1.69×10^{-6}
9	2.93	2	15.28	3.42×10^{-8}	2.61×10^{-11}	116	0.104	1.99×10^{-6}
10	3.17	6	13.11	1.36×10^{-8}	1.73×10^{-11}	124	0.107	1.80×10^{-6}
11	2.59	9	10.76	3.13×10^{-8}	1.36×10^{-11}	157	0.106	2.62×10^{-6}
12	2.48	8	15.87	1.56×10^{-8}	1.30×10^{-11}	93	0.121	1.70×10^{-6}
13	2.75	6	15.98	1.48×10^{-8}	1.08×10^{-11}	95	0.120	1.46×10^{-6}
14	3.68	4	14.89	8.83×10^{-9}	1.06×10^{-11}	104	0.110	1.34×10^{-6}
15	3.68	8	16.35	7.02×10^{-9}	1.16×10^{-11}	102	0.110	1.40×10^{-6}
16	7.10	65	11.70			136	0.125	3.98×10^{-7}
17	7.76	77	9.20			65	0.129	4.51×10^{-7}
18	6.68	83	9.43			127	0.146	4.70×10^{-7}
19	5.70	85	8.78			108	0.138	4.45×10^{-7}
20	4.19	71	8.43			90	0.138	9.93×10^{-7}
21	2.46	62	8.59			3	0.117	1.70×10^{-6}
22	3.28	1	9.12	7.69×10^{-8}	1.18×10^{-11}	87	0.095	4.75×10^{-6}
23	4.62	2	9.80	1.37×10^{-8}	1.40×10^{-11}	89	0.086	9.32×10^{-7}
24	6.34	24	4.68	6.19×10^{-9}	1.15×10^{-11}	150	0.087	6.61×10^{-7}
25	4.95	23	7.60	7.96×10^{-9}	1.77×10^{-11}	80	0.095	1.03×10^{-6}
26	4.62	28	3.32	1.61×10^{-8}	1.83×10^{-11}	160	0.100	1.10×10^{-6}
27	5.68	18	5.56	4.72×10^{-9}	1.18×10^{-11}	135	0.101	8.27×10^{-7}
28	4.55	18	5.84	3.12×10^{-7}	1.70×10^{-11}	121	0.100	1.03×10^{-6}
29	4.22	2	5.47	2.79×10^{-8}	1.64×10^{-11}	147	0.102	1.03×10^{-6}

Table 3: Parameters of the 30 MIDI data sets—continued from Tables 1 and 2. The meaning of columns is detailed on page 56.

3.3 Power Spectra of Phases

The conversion of C_ρ^2 to predicted power spectra of the phase fluctuations is done with the Clifford formula (last line of Table 1 in [1]),

$$PDF_\varphi(\nu) = 0.06601 k^2 \frac{K}{\sin a} C_n^2 v_\perp^{5/3} [1 - \cos(2\pi P \nu / v_\perp)] \nu^{-8/3} \tag{14}$$

where $0.06601 = \Gamma(8/3)\sin(\pi/3)/(2\pi^2)$ [17], where $v_\perp$ is in Table 3, P the projected baseline of Table 1, and the air mass in Table 1 or the reciprocal sine of the altitude of table 2.

Supposed the water vapor and dry air contributions to the statistics are independent and add in quadrature, the factor in (14) is replaced by

$$k^2 K C_n^2 = k^2 K_{\rm wet} C_{n,\rm wet}^2 + k^2 K_{\rm dry} C_{n,\rm dry}^2 = k^2 \hat\chi_{\rm wet}^2 K_{\rm wet} C_{\rm H2O}^2 + k^2 \hat\chi_{\rm dry}^2 K_{\rm dry} C_{\rm dry}^2 \tag{15}$$

with $K_{\rm wet} \approx 1660$ m, $K_{\rm dry} \approx 9600$ m (Fig. 25 in [13]), and $k\hat\chi$ as in (5).

The synopsis of these predictions from the water vapor fluctuations (red) or all contributions (blue) compared to the individual MIDI fringe tracker data of Figures 4, 5, 6,. . . ,33 (green) follows in Figures 44–46.

- The predictions (red) constructed/extrapolated from LI-COR water vapor fluctuations are typically a factor 100 too small.
- The predictions (blue) constructed from re-interpretation of the `RO_MEAN` keywords of the FITS headers (blue) via (13)—essentially not using any LI-COR data and therefore out-of-topic for this report here—are approximately correct in the frequency range up to 5 Hz.

The expected discrepancy is at most a factor of 2, because the contribution of various surface vibrations within the VLTI train to the PDF [8] of φ—as estimated in Fig. 43—is typically less than the expected contribution of the fluctuations of the ambient air humidity, supposed that the mirror vibrations of the VLTI mirror train, including effects of the MDL and responses of mirrors driven by IRIS, are negligible.

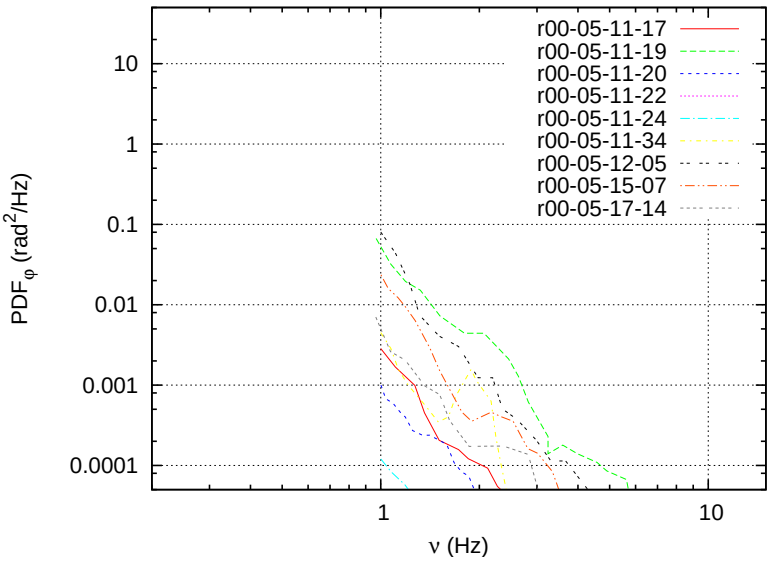

Figure 43: Contribution of some VLT mirror vibrations up to M6 to the PDF of the 10 μm phase. Values from [8] measured with UT3 under various conditions of activities of motors and pumps have been halved to account for an undocumented, presumably 1-sided definition of the spectra, then doubled to account for an (again undocumented) overlay of 2 telescope mirror trains, and scaled with $k^2 = 4\pi^2/\lambda^2 \approx 4 \times 10^{11}$ m^2 to transform lengths to phases.

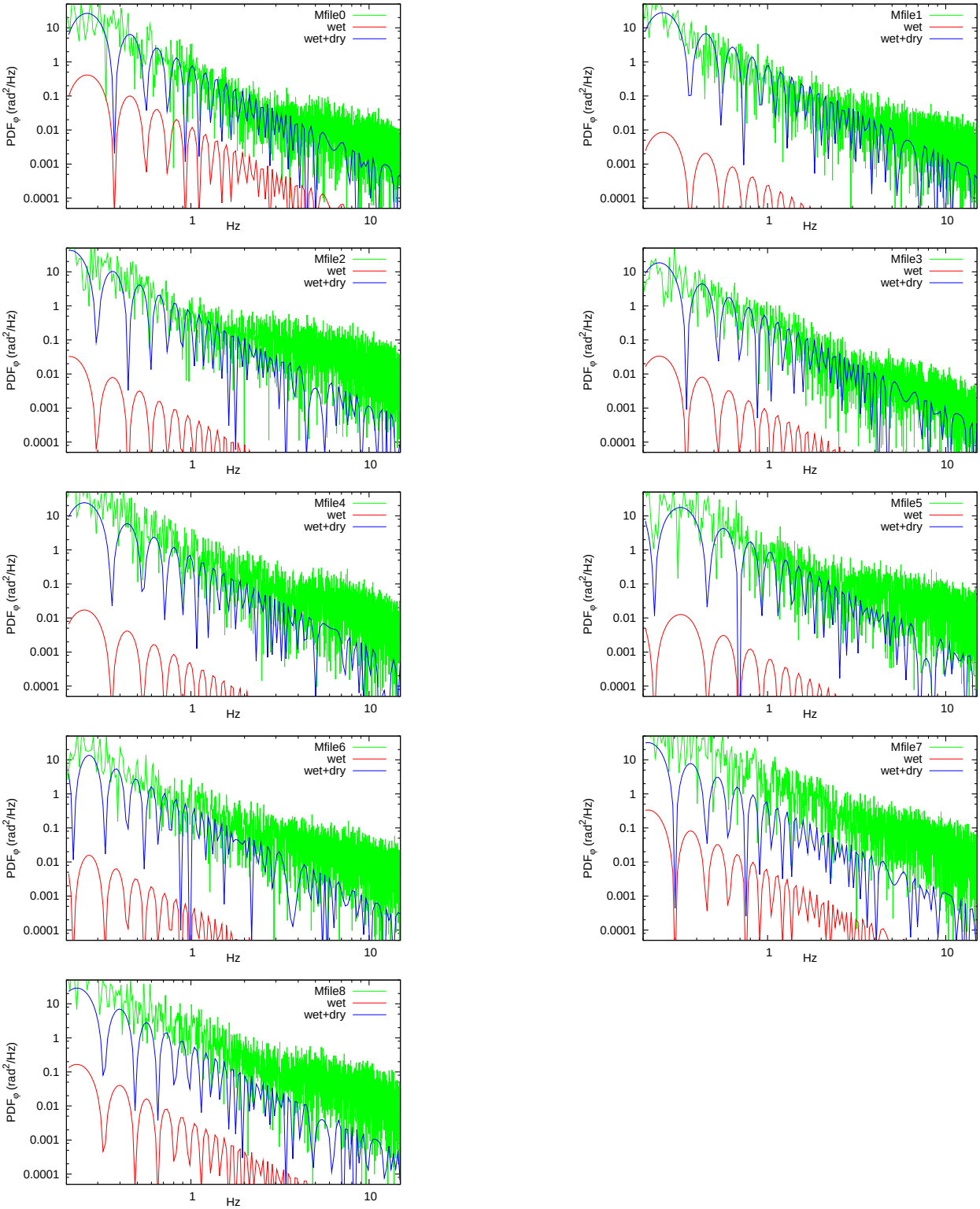

Figure 44: Comparison of the Clifford model (14) with the measured PDFs of the 10 μm phases of the first night. The numbers of (14) have been halved to account for the fact that the Clifford model (presumably) uses 1-sided PDFs.

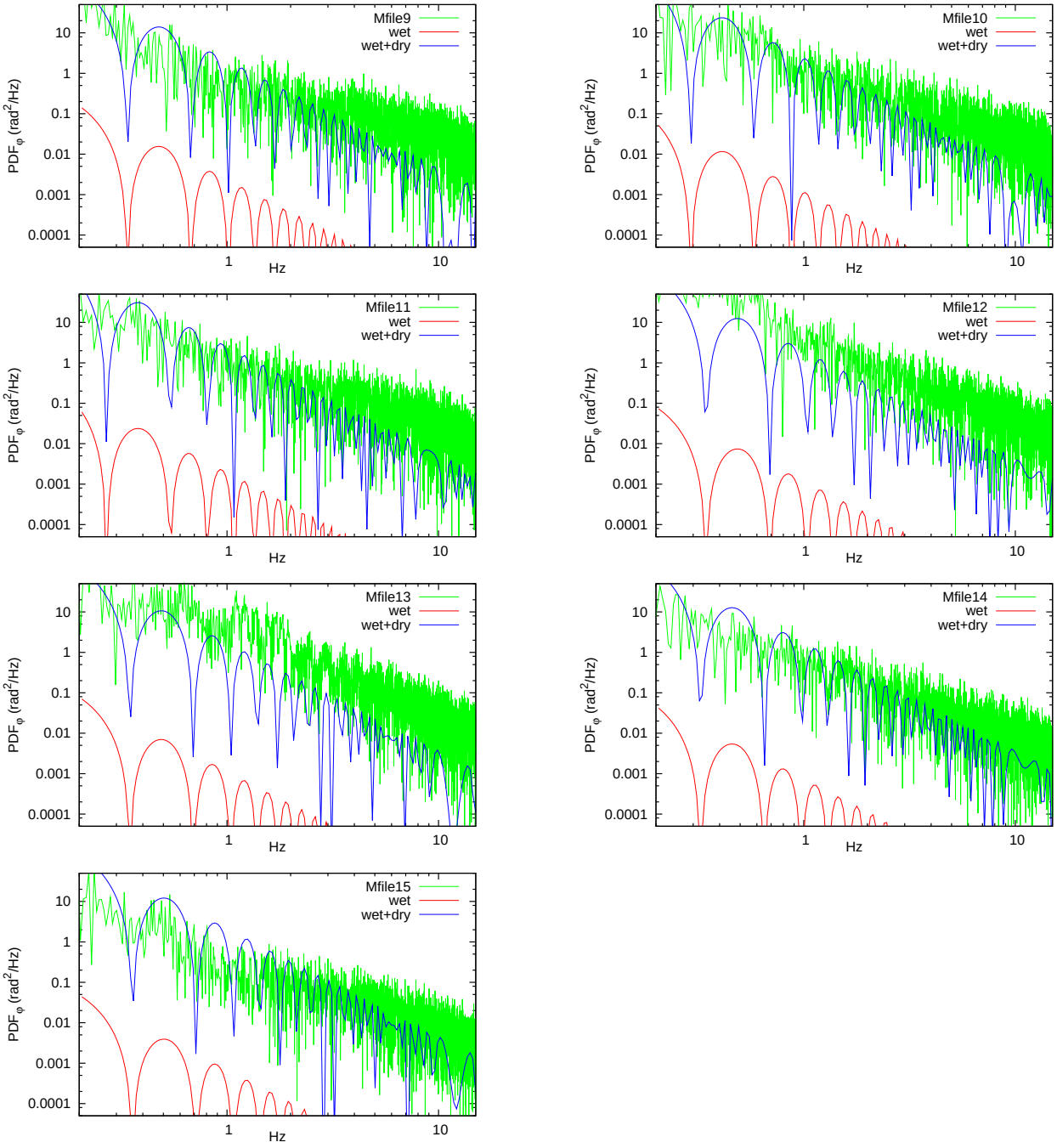

Figure 45: Continued from figure 44 into the second night of MIDI observations.

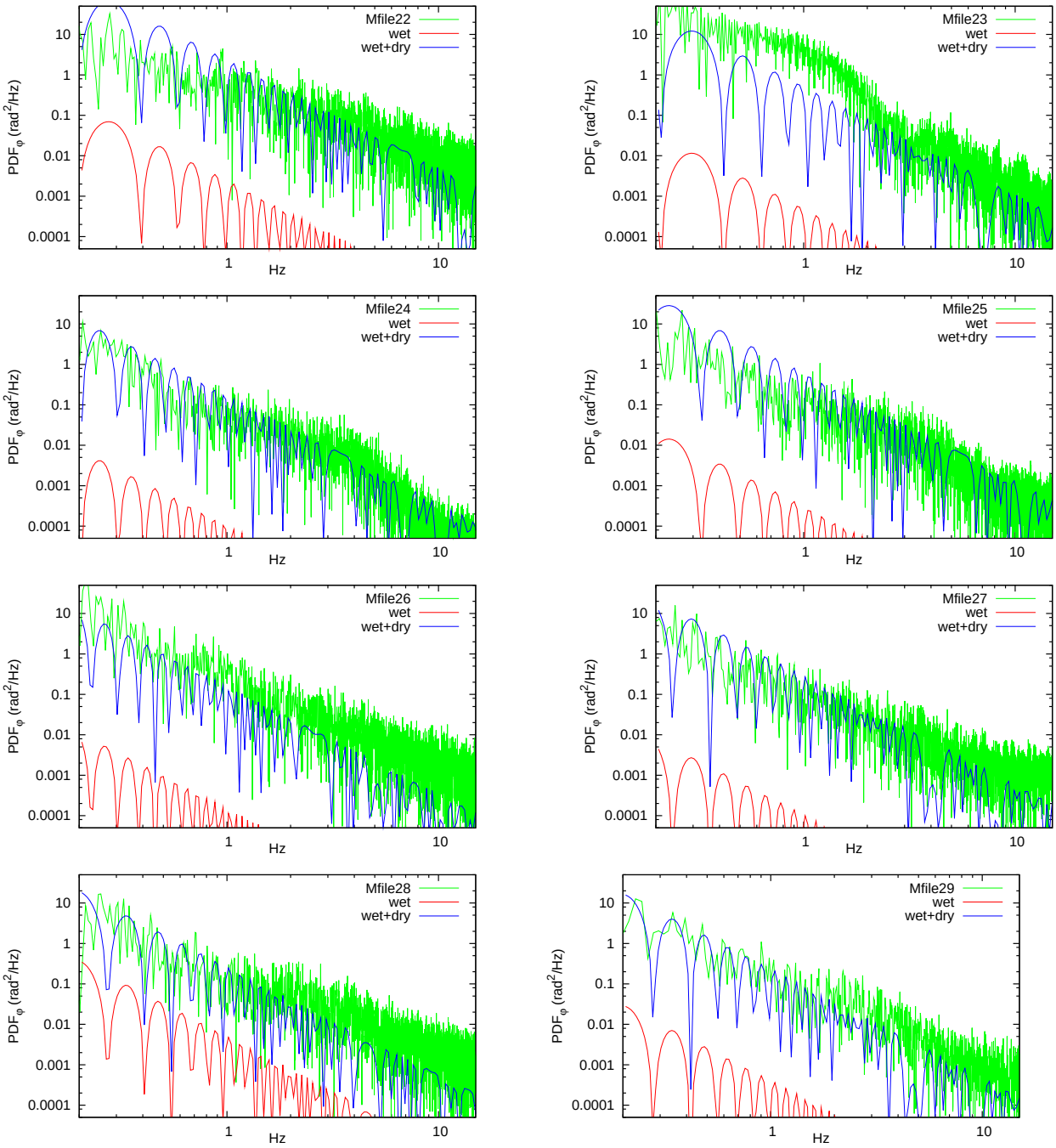

Figure 46: Continued from figure 45 covering the fourth night of MIDI observations. `Mfile23` is essentially to be ignored because it is contaminated by the bi-stable sudden 100 μm jump of φ' in Fig. 27.

3.4 Phases Extrapolated to Zero Wavenumber

If one decomposes the intrinsic air refractive index

$$n = 1 + \rho_{\rm dry}\hat{\chi}_{\rm dry} + \rho_{\rm wet}\hat{\chi}_{\rm wet} \tag{16}$$

as in Section 3.1,

$$k\hat{\chi}_{\rm dry} = a_{\rm dry} + b_{\rm dry}k; \quad k\hat{\chi}_{\rm wet} = a_{\rm wet} + b_{\rm wet}k, \tag{17}$$

equations (1)–(2) are the associations

$$\varphi_0 = \rho_{\rm dry}a_{\rm dry}D_t + \rho_{\rm wet}a_{\rm wet}D_t \tag{18}$$

and

$$\varphi' = D_t + \rho_{\rm dry}b_{\rm dry}D_t + \rho_{\rm wet}b_{\rm wet}D_t - D_e \tag{19}$$

between observed and theoretical parameters. The full meaning of terms like $\rho_{\rm dry}D_t$ is $\int_1 \rho_{\rm dry}dl - \int_2 \rho_{\rm dry}dl$, the difference between two path integrals for telescopes 1 and 2 over atmosphere and tunnel up to the detector. None of these two variables is actually correlated with the D_e of Table 1: φ_0 contains arbitrary offsets in units of 2π, and φ' is kept close to zero by group delay tracking.

$\rho_{\rm wet}a_{\rm wet}$ and $\rho_{\rm dry}a_{\rm dry}$ are typically -0.42 1/m and -0.036 1/m (Figs. 37, 38). The benefit of extrapolation of the phases to zero wavenumber, represented by φ_0, is that statistical variations of DL mirrors or AO optics up to some $\delta D_i \approx 1$ mm could at most change this wave-number independent component of the phase on sub-milli-radian scales. One has essentially found a parameter that is very insensitive to incoherent vibrations and motions of the two beam's optical subsystems and DL carriages, but still sensitive to the differential water-column over which the two beams integrate while traveling through the atmosphere.

The 2D phase structure function $\mathcal{D}_\varphi$ is related to the 3D structure function $\mathcal{D}_n$ of the refractive index as [5, 7]

$$\mathcal{D}_\varphi(\xi) = KC^{(0)}(\alpha)k^2\mathcal{D}_n\xi, \tag{20}$$

where $\xi = vt$ is the projected lateral distance across the pupil, $C^{(0)}(\alpha)$ a numerical factor depending on the exponent α that describes the growth of the 3D structure function, K the distance over which the phase is integrated along the line of sight, and $k = 2\pi\sigma$ the momentum number of the radiation. Splitting the refractive index into the zero-extrapolated $a_{\rm wet,dry}$ and slopes $b_{\rm wet,dry}$ decomposes the previous equation into

$$\mathcal{D}_\varphi(\xi) = \mathcal{D}_{\varphi_0}(\xi) + \underbrace{k^2\mathcal{D}_{\varphi'}(\xi)}_{\propto k^2} + \underbrace{\mathcal{D}_{ab}}_{\propto k}. \tag{21}$$

So we look only at the component of

$$k^2\mathcal{D}_n = k^2(\hat{\chi}^2_{\rm dry}D_{\rho,\rm dry} + \hat{\chi}^2_{\rm wet}D_{\rho,\rm wet}) = k^2(\hat{\chi}^2_{\rm dry}D_{\rho,\rm dry} + \hat{\chi}^2_{\rm wet}D_{\rho,\rm wet}) \tag{22}$$

of (20) which is independent of k

$$\mathcal{D}_{\varphi_0}(\xi) = KC^{(0)}(\alpha)(a^2_{\rm wet}\mathcal{D}_{H2O} + a^2_{\rm dry}\mathcal{D}_{\rm dry})\xi. \tag{23}$$

Here $K \approx 1660$ m (Figure 59 in [13]), $C(2/3) \approx 2.9$ and $a^2_{\rm wet} \approx (2.53 \times 10^{-2})^2{\rm m}^6/({\rm mol}^2{\rm cm}^2) \approx 6.4{\rm m}^4/{\rm mol}^2$ (eq (7)), therefore $KC(2/3)a^2_{\rm wet} \approx 3.1 \times 10^4$ m^5/mol^2.

Figs. 47–50 show the correlation between the φ' and φ_0 values, one figure per night, one panel per exposure. The first 2000 frames of each exposure are shown with red plusses, the 2nd 2000 frames with green crosses, the 3rd 2000 frames with blue boxes, and the final set of frames (none left over in this category for `Mfile19` and `Mfile29` which were shorter) magenta squares. This are painted on top of each other; so the read portions tend to be hidden by the latter data if all of them stay close.

The model of air dominated phase fluctuations predicts a correlation between φ_0 and φ' with a negative slope, which means a change of the overall air density modifies the (positive) slope of the bottom of Figures 37 and 38 by the same factor as their (negative) intersection. This explains why the point spread functions in Figs. 47–50 are tilted: For water-dominated fluctuations the slope is predicted as

$$\frac{\varphi_0}{\varphi'} = \frac{a_{\rm wet}}{b_{\rm wet}} = \frac{-4.21\times10^{-1}{\rm m}^{-1}}{1.3224\times10^{-6}} \approx -31.8/(100\mu{\rm m}), \tag{24}$$

and for dry-air dominated fluctuations it is

$$\frac{\varphi_0}{\varphi'} = \frac{a_{\rm dry}}{b_{\rm dry}} = \frac{-3.608\times10^{-2}{\rm m}^{-1}}{2.0485\times10^{-4}} \approx -0.0176/(100\mu{\rm m}), \tag{25}$$

the latter too small to be distinguishable from the zero of mirror surface fluctuations.

This could be used to separate the components [4]: The actual slopes are smaller than $-5/(100\mu{\rm m})$ during the very dry first night, Fig. 47, around $-10/(100\mu{\rm m})$ during the second and fourth night of average humidity, Figs. 48+50, and largest, around $-12/(100\mu{\rm m})$ for the slightly wetter third night, Fig. 49. These estimates confirm that the slope of φ_0/φ' is sensitive to the water content in the air—the VLTI is indeed an (expensive) hygrometer, the negative aspect is that either the jitters in the reflecting mirror surfaces or the contribution of the dry air fluctuations *do* contribute to the fringe motion substantially, as the value of φ_0/φ' near $-32/(100\mu{\rm m})$ of (24) is *not* reached.

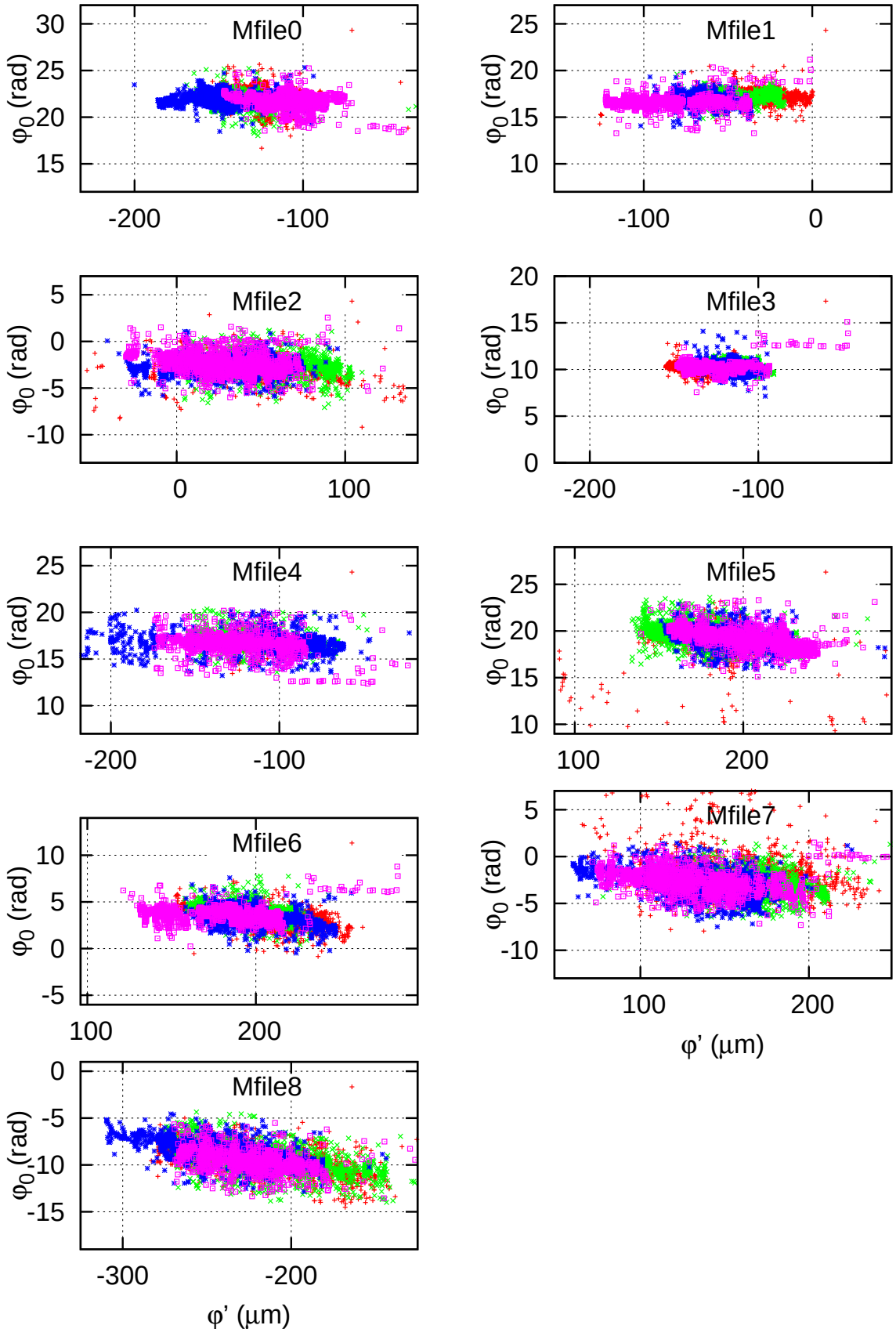

Figure 47: Correlation between φ' and φ_0 for the fringe fits of the first night. φ_0/φ' is in the range of 0 to $-5/(100\mu\text{m})$.

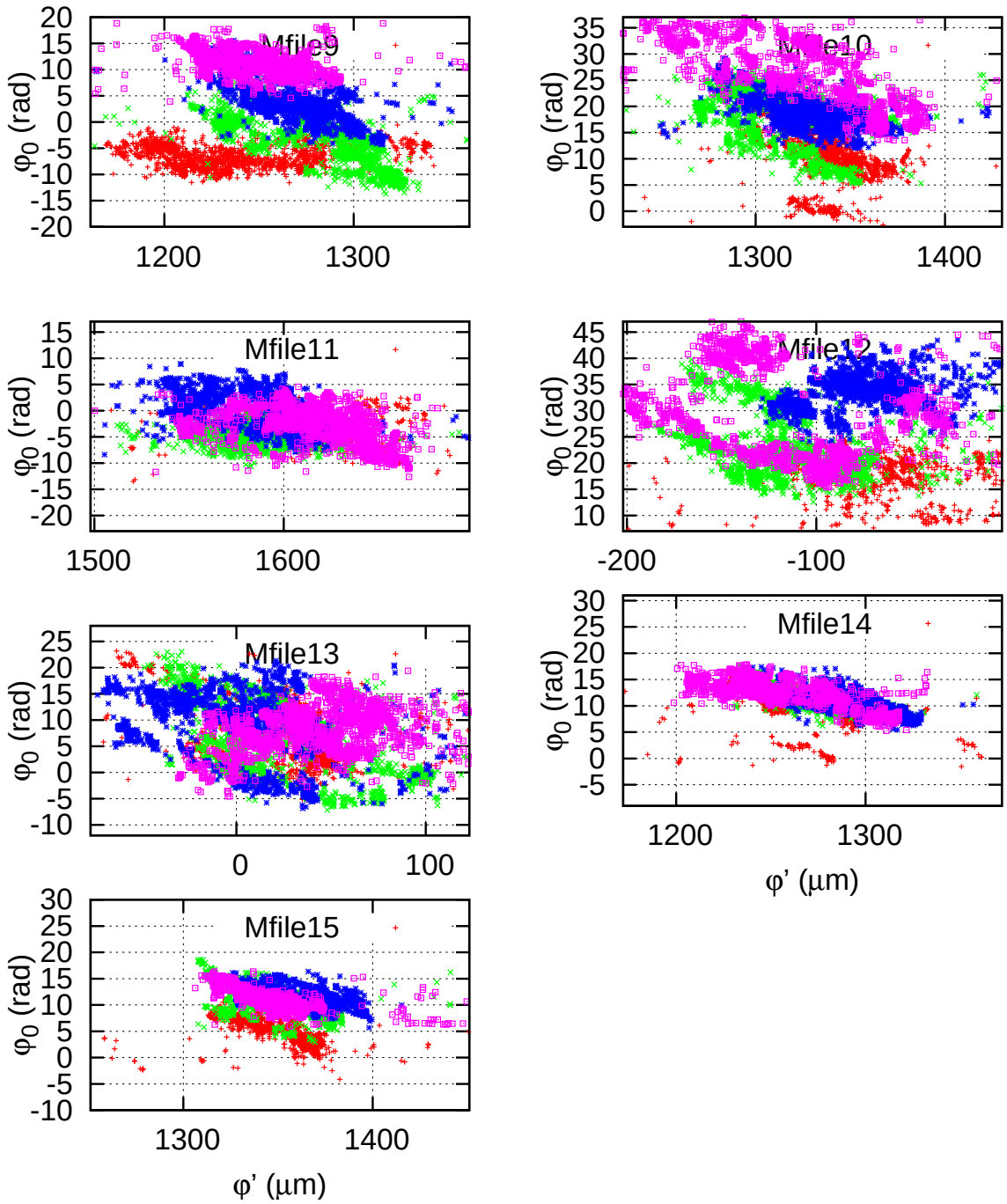

Figure 48: Correlation φ' and φ_0 for the fringe fits of the second night. φ_0/φ' is of the order $-10/(100\mu\text{m})$. Formation of separated streaks is probably an indicator of 2π errors in the phase unwrapping algorithm—the optimistic interpretation is that a clustering algorithm on this type of display may detect this condition in imaging modes. The colorization of the exposures in blocks of 2000 frames (chunks of ≈ 42 s per color) is meant to bolster this interpretation.

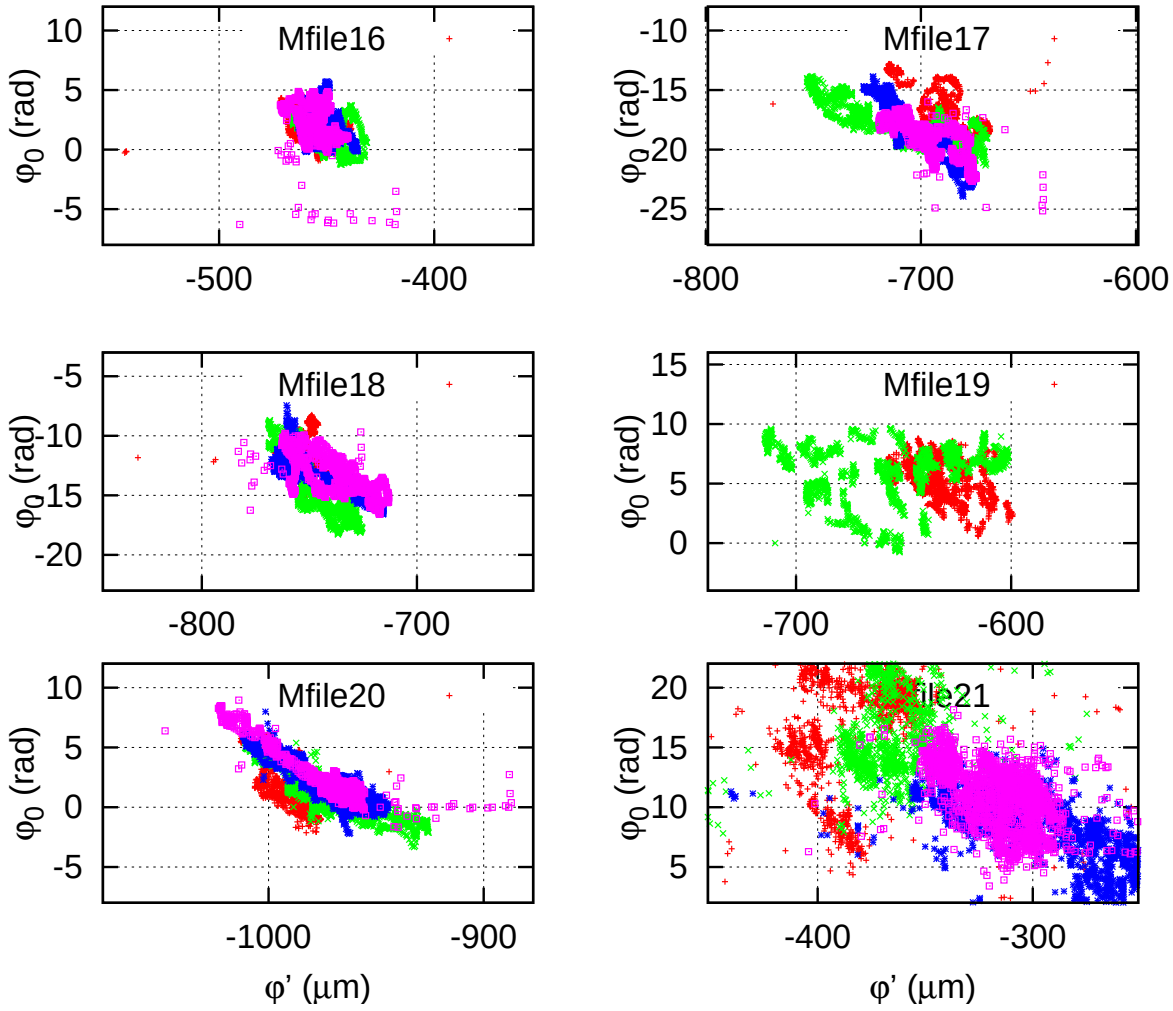

Figure 49: φ' and φ_0 for the MIDI fringe fits of the third night. φ_0/φ' is of the order $-12/(100\mu\text{m})$.

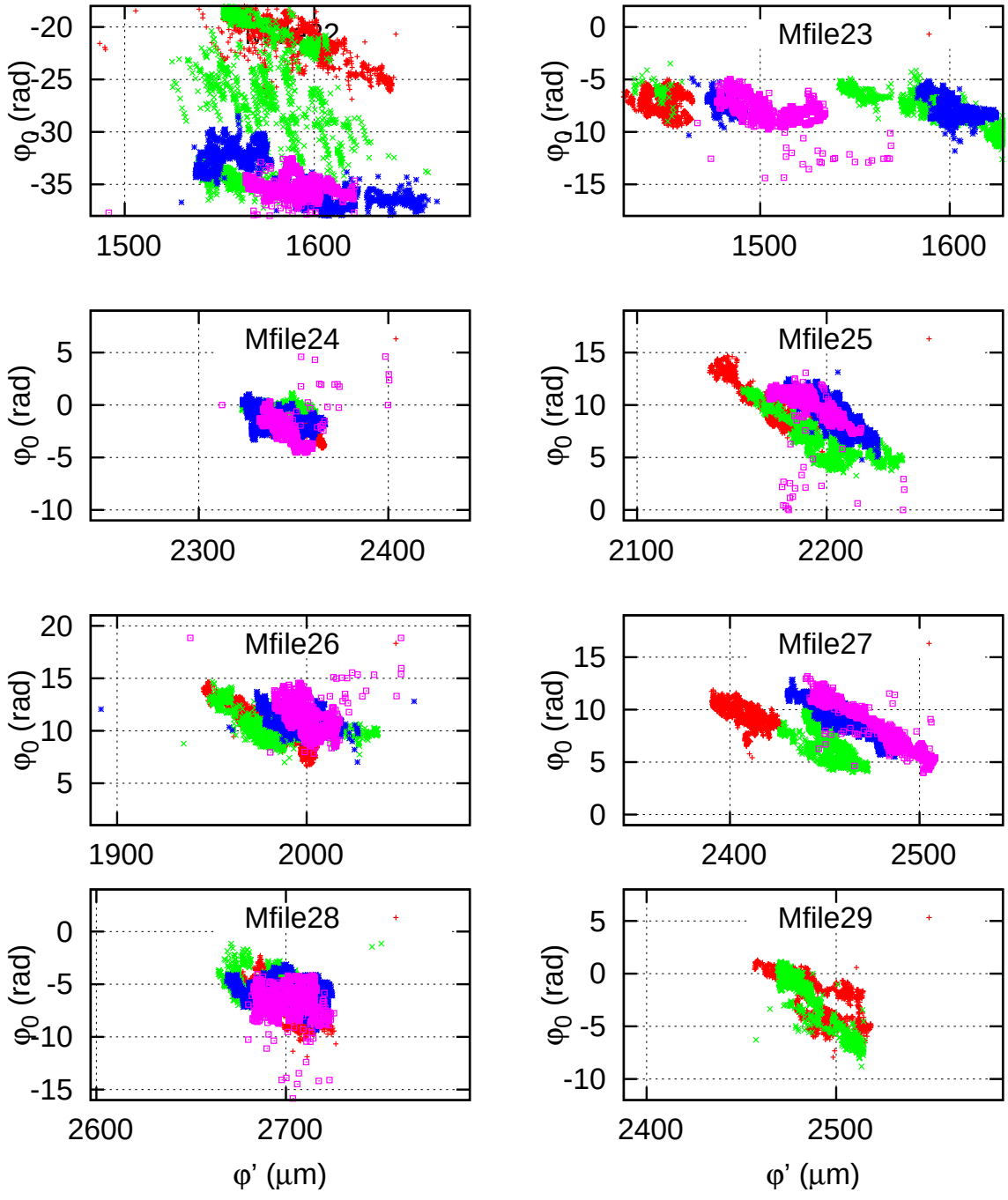

Figure 50: φ' and φ_0 for the MIDI fringe fits of the fourth night. φ_0/φ' is of the order $-10/(100\mu\text{m})$.

The influence of the dry air fluctuations are in comparison: $a^2_{\rm dry}/a^2_{\rm wet} \approx 2 \times 10^{-7}$ (Eq. 7). The scale height ratio contributes with a factor $K_{\rm dry}/K_{\rm wet} \approx 9.5/1.6 \approx 6$. From Figure 47 in [16] we estimate $\mathcal{D}_{\rm dry}/\mathcal{D}_{\rm H2O} \approx 3 \times 10^3$. So the relative magnitude of the dry air structure function is the product of these factors, $2 \times 10^{-7} \times 6 \times 3 \times 10^3 \approx 3.6 \times 10^{-3}$, negligible for our purposes. As we show the power density functions of φ_0 in Figures 51–53, the predictions (in red) are essentially the same, whether the dry air components are included or not.

The fluctuations of the zero-extrapolated component of the MIDI fringe fits are roughly two orders of magnitude higher than derived from the measured water structure functions: Figs. 51–53. They are of the $1/f$-noise shape at frequencies below 1 Hz, flat in the region up to 5 Hz, with a crossover to the predicted $\nu^{-8/3}$ Kolmogorov shape above 5 Hz.

The transition at 5 Hz is a result of a smoothing operation in the IDL software: a 5 Hz Nyquist frequency is equivalent to a filter of 0.1 s width in the time domain, or equivalent to averaging over 5 frames (see Section 2.1).

The model of constant group delay has re-written (1) and (16) as

$$\varphi(k) = k(D_i - D_e) + \rho_{\rm dry} D_i (a_{\rm dry} + b_{\rm dry} k) + \rho_{\rm wet} D_i (a_{\rm wet} + b_{\rm wet} k). \tag{26}$$

The difference between this Section 3.4 here and Section 3.3 is that we are now looking at the limit $k \to 0$; instead of addressing inclinations of the straight lines in the lower plots of Figures 37 and 38 we are now looking at the interception with the ordinate axes. The difference between the MIDI fringe tracker fits and projected estimates from air turbulence profiles (LI-COR etc) is measured by some missing factor between the PDF, typically 100 in Figures 51–53, or in units of amplitudes the square root of this, typically 10, but anyway a *relative* measure. The failure to converge the two data sets is a result of a very unfortunate error propagation in the lower plot of Figure 38: since the MIDI phase estimates in the range of 700 to 1400 cm^{-1} are inherently noisy in all ≈ 30 dispersed channels of the prism, a measure of the slope of the curve with acceptable *relative* error is still possible since the value on the curve drops by ≈ 30 % over the full range of the spectrum—which could not be done if the curve would be much flatter. A measure of the interception with the ordinate axis, on the other hand, with a *relative* error of same quality is almost impossible because the value of $k\chi(k)$ at the interception is only 3×10^{-4} of its magnitude within the N-band.

In summary, the green curves of the φ_0 parameter in Figures 51–53 are only a measure of infrared background and detector-readout noise; this shadows entirely the fluctuations we would expect in addition from the turbulence in the atmosphere above the two telescopes, represented by the red curves. A detailed look into these curves is of no value within the scope of this report.

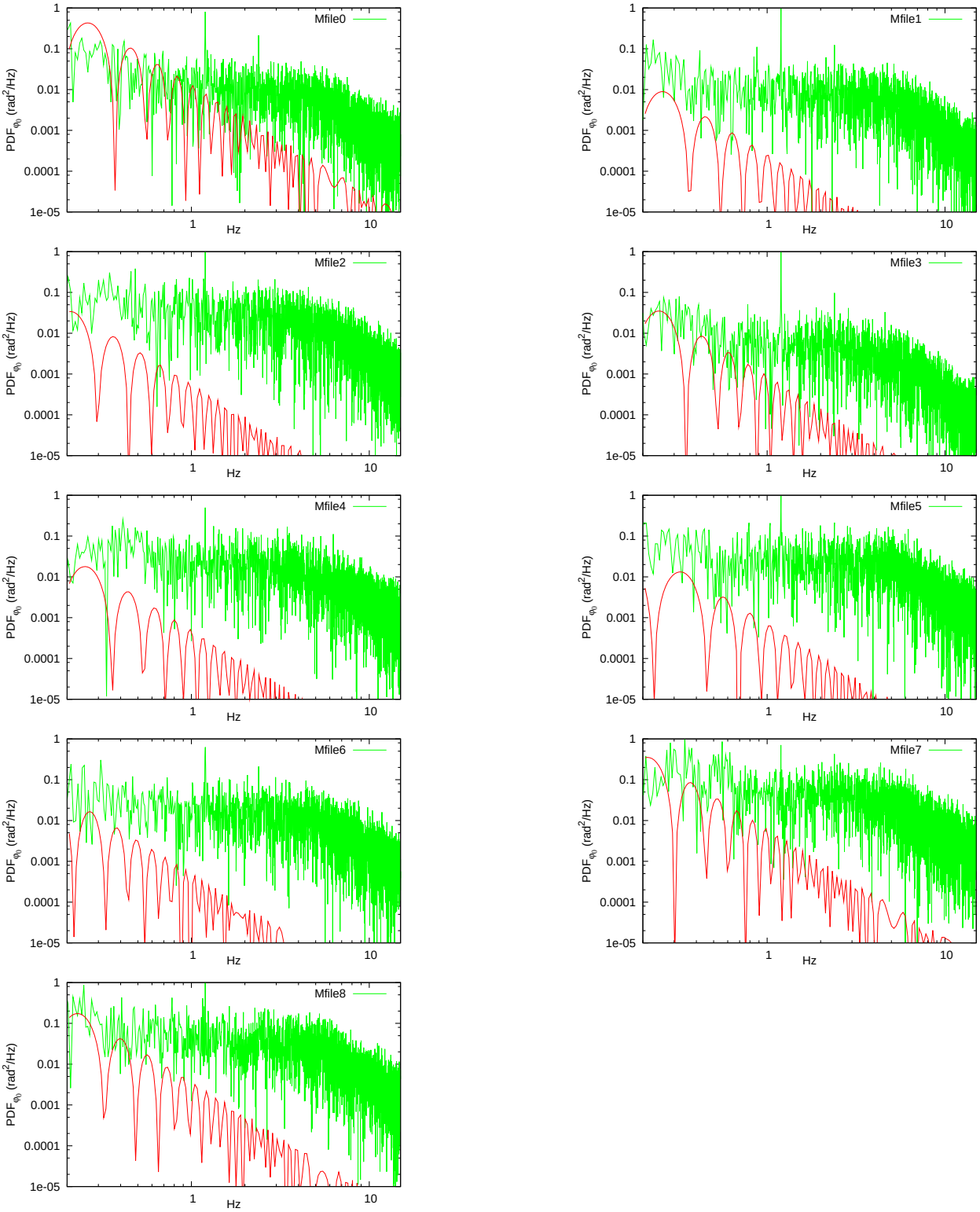

Figure 51: Comparison of the Clifford model (14) with the measured PDFs of the phases extrapolated to $k = 0$ in the range 0.2–15 Hz. Red the values derived from gas density fluctuations (both with or without water vapor), green the MIDI phases extrapolated from the N band to infinite wavelength.

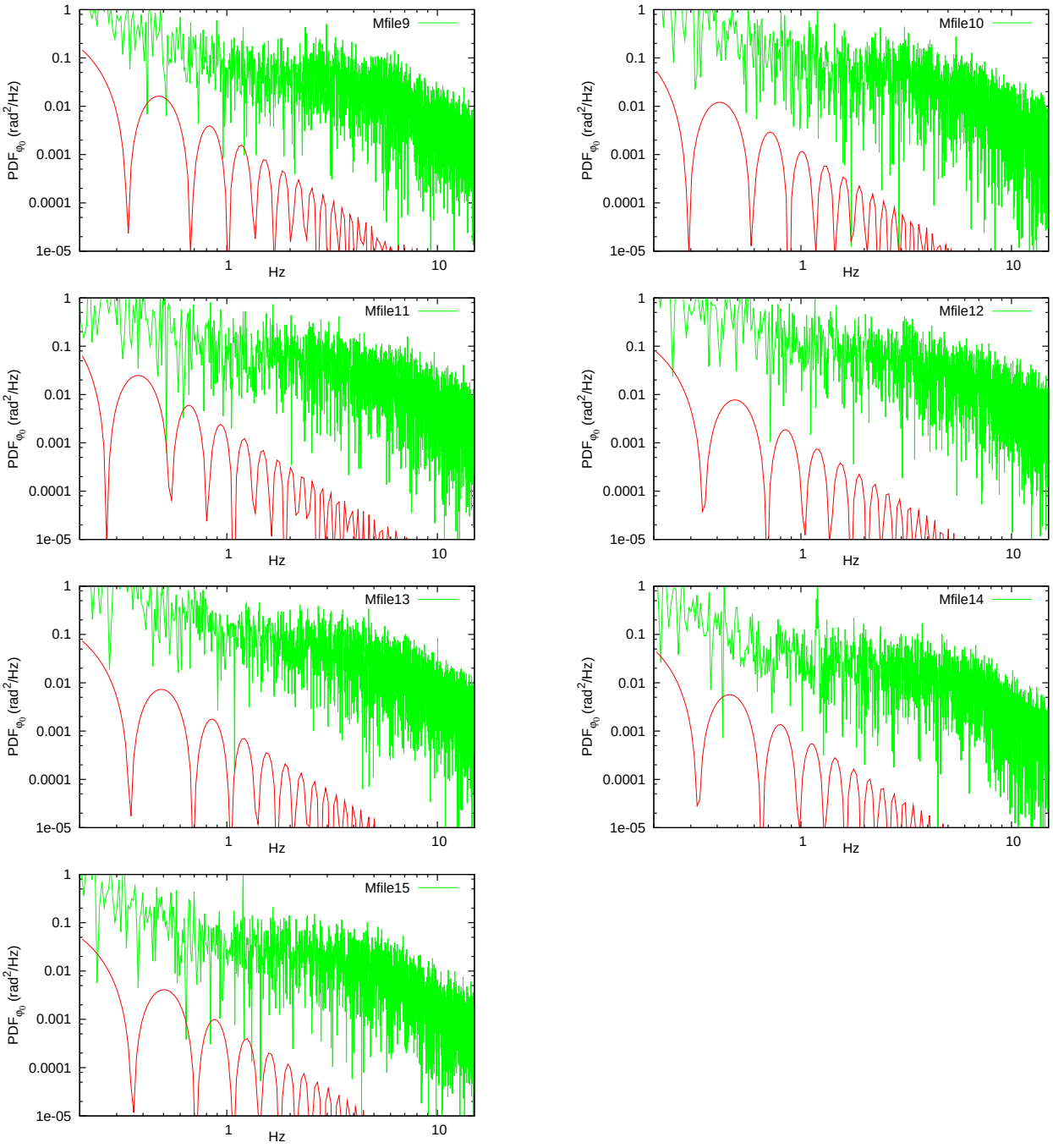

Figure 52: Continued from figure 51 covering the second night of MIDI observations.

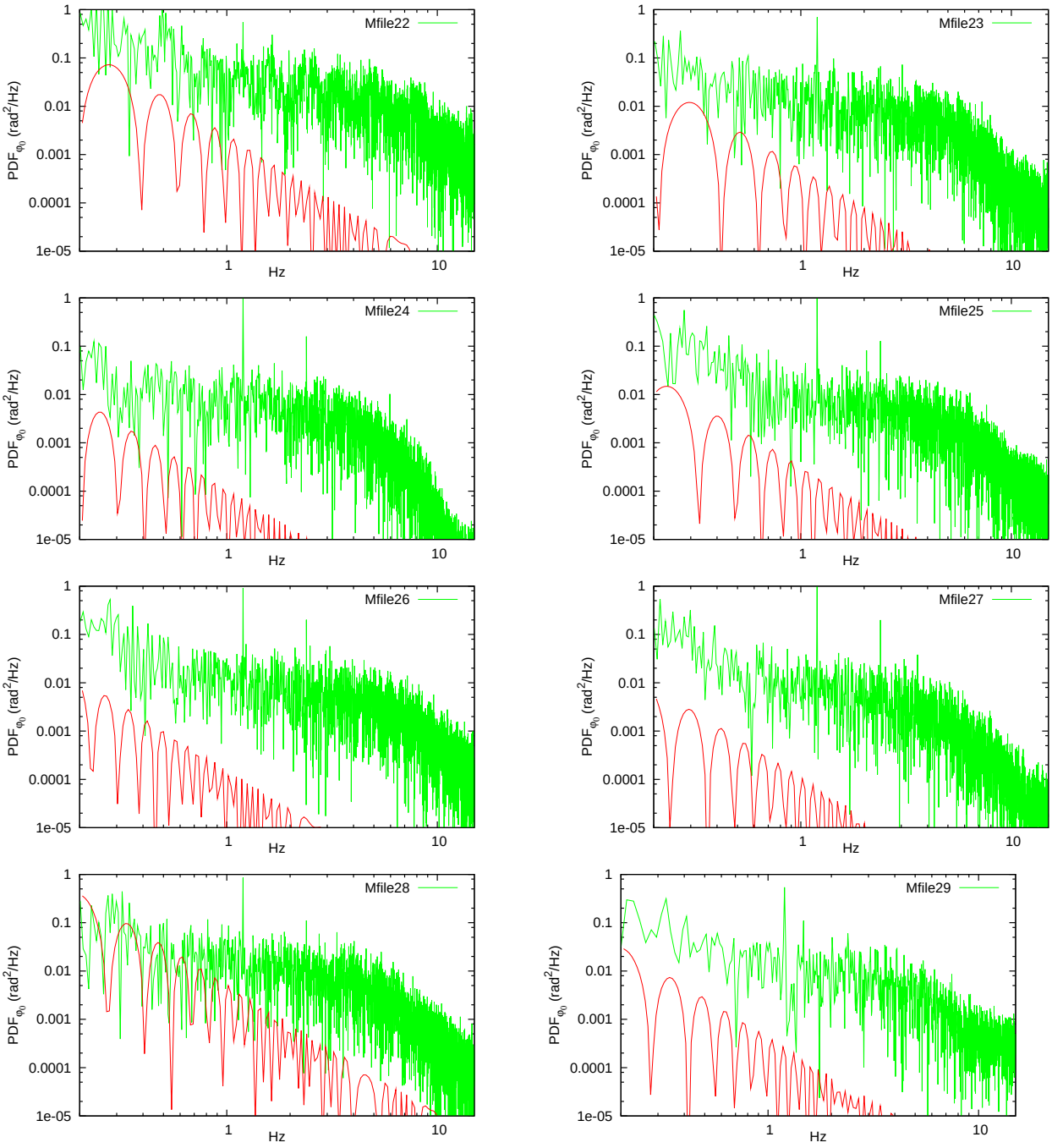

Figure 53: Continued from figure 52 covering the fourth night of MIDI observations.

4 SUMMARY

We summarize 30 exposures of prism-dispersed MIDI N-band interferometric fringe phase data—a total exposure time of roughly an hour spred over four nights in June 2007—in terms of power density spectra.

1. Prediction of the 10 μm phase fluctuation from the UT AO system's Fried parameter (at a wavelength of 500 nm) is robust in the frequency range up to 3 Hz. Deviations in the power spectral density are typical less than a factor of two. The stability of this analysis is due to the fact that (i) the integration over the scale height of the Troposphere is already done implicitly in the AO system which receives the path integrated phases anyway, and (ii) the other major parameters (wind speed/direction and air mass) are either well known or well represented by ground measurements.

   In the plots of the power spectral density of this phase φ evaluated at $\lambda = 10\mu$m, there is no noticable difference between either using or neglecting the water vapor content measured at the ground in the composition of the C_n^2.

2. The LICOR IR gas analyzer's carbon dioxide data cannot be used to estimate the local air density fluctuations at medium and high frequencies because the digitization noise is roughly a factor 10 higher than the (estimated) actual equivalent value of C_n^2. This is the reason why the strength of the turbulence is computed from the AO data as described above.

3. Since the N-band refractive index dispersion is large compared to the dispersion at smaller wavelengths, there is a promise that dispersed phase measurement across the N-band may separate the wet and dry air delays by 2-parametric fits of slope and interception. Unfortunately, the actual shape of the gas dispersion means that the sensitivity in the determination of the interception (extrapolation of phases to zero wavenumber in the plot of phase versus wavenumber) cannot be reached by MIDI; the noise sources *besides* the fluctuations in the optical path differences (that is, detector readout and background noise) dominate the noise in the fitted interception, and the extracted spectral density of that parameter is non-Kolmogorov, spot noise reshaped by software filters.

   For this reason, qualitatively quite different from abandoning the carbon dioxide information, the high frequency water vapor density measurements with the LICOR analyzer have not contributed to the current analysis.

4. Another general aspect of the 2-parametric fit of dispersed phase data with slope and interception is that the interception is insensitive to the OPD induced by mirror motions/vibrations. Here, the analysis of low-frequent co-motions of slope and interception monitored over typically 30 seconds reveals that the sensitivity of the interception to the slope parameter is correlated with the average ambient humidity. (The methodological difference to the point made above is just that a scan over 30 seconds extracts information that remains hidden by other noises/fluctuations if restricted to 1 Hz information.)

   As noticed under the first item, this information does matter if the phase fluctuations are to be modeled; this does not preempt evaluation in other contexts, such as (i) determination of the precipitable water vapor integrated over some 2 kilometers above the telescopes, (ii) detection of fringe jumps in unwrapping algorithms, potentially related to imaging modes, (iii) separation of phase jitters contributed from reflecting mirror surfaces or contributed from gas density flucuations, and others.

___oOo___